

EVALUATION OF UAS-BASED REMOTE SENSING FOR MEASURING FORAGE  
PROPERTIES AT AN EXPERIMENTAL GRAZING LAND

A Thesis

by

LAURA ELIZABETH CARBAJAL

BA, University of Texas at San Antonio, 2010

Submitted in Partial Fulfillment of the Requirements for the Degree of

MASTER of SCIENCE

in

GEOSPATIAL SYSTEMS ENGINEERING

Texas A&M University-Corpus Christi  
Corpus Christi, Texas

December 2018

ProQuest Number: 13419131

All rights reserved

INFORMATION TO ALL USERS

The quality of this reproduction is dependent upon the quality of the copy submitted.

In the unlikely event that the author did not send a complete manuscript and there are missing pages, these will be noted. Also, if material had to be removed, a note will indicate the deletion.



ProQuest 13419131

Published by ProQuest LLC (2019). Copyright of the Dissertation is held by the Author.

All rights reserved.

This work is protected against unauthorized copying under Title 17, United States Code  
Microform Edition © ProQuest LLC.

ProQuest LLC.  
789 East Eisenhower Parkway  
P.O. Box 1346  
Ann Arbor, MI 48106 – 1346

© Laura Elizabeth Carbajal

All Rights Reserved

December 2018

EVALUATION OF UAS-BASED REMOTE SENSING FOR MEASURING FORAGE  
PROPERTIES AT AN EXPERIMENTAL GRAZING LAND

A Thesis

by

LAURA ELIZABETH CARBAJAL

This thesis meets the standards for scope and quality of  
Texas A&M University-Corpus Christi and is hereby approved.

Michael J. Starek, PhD  
Chair

Jamie L. Foster, PhD  
Committee Member

Gary A. Jeffress, PhD  
Committee Member

December 2018

## ABSTRACT

This study uses Unmanned Aircraft Systems (UAS) to provide multispectral imagery and point cloud data to measure the health, height, and structure of plants. The high spatial resolution coupled with control over the temporal resolution of the data provide a potentially invaluable tool for grazing land management.

Study areas were flown throughout the growing season in 2016 and 2017 at the Texas A&M AgriLife Beeville Station at the Tifton 85 and Sandy fields to measure forage health by calculating four vegetation indices (VIs) from the resulting reflectance images. VIs were used to estimate forage parameters such as plant height, herbage mass, and protein content, which were measured in the field for comparison. Digital elevation models and digital surface models were also created from the structure-from-motion (SfM) point cloud generated from the UAS flight. Multiple filtering algorithms were used to classify the raw point cloud into ground and non-ground classes. The classified points were then used to create ground and surface models for the 2016 flights. These surfaces were used to create terrain maps and to attempt to estimate plant height throughout the pasture.

Linear regression analysis was performed to determine the strength of the association of each VI to forage field measurements for the 2016 and 2017 flights. Herbage mass and crude protein show the most significant regression with most of the vegetation indices, especially in the 2017 flights. Inconsistency between the 2016 and 2017 flight results highlights the importance of flight parameters in the resulting data. Future field data collection may show stronger relationships given improvements in experimental design and enable more comprehensive and accurate estimates of grazing land forage quantity and quality.

## DEDICATION

I would like to dedicate this thesis to my parents, Harold and Teresa Klemcke, who have supported me unfailingly throughout my life and education.

## ACKNOWLEDGEMENTS

I would like to thank my advisor, Dr. Michael Starek, for being patient and flexible and encouraging through several years of coursework and research. Thank you for providing me with such a fascinating and challenging thesis topic, for helping me to navigate the Master's program, for advocating on my behalf when I could not be on campus, and for helping me to find financial support. Without your help I could not have finished such a professionally and technically challenging and satisfying program.

I would like to thank the Texas A&M AgriLife team for making this research possible, and for providing generous financial support to help with my tuition. I would especially like to thank Dr. Jamie Foster for heading this project and for being so patient and understanding with my work schedule. Thank you for giving me the opportunity to work with such exciting research. I would also like to thank Dr. Megan Clayton for giving valuable insight into the laboratory results.

Special thanks to Jake Berryhill of the Mantis Laboratory for his work in the field and for providing me with the data needed to do this research. As a distance student I was disappointed I could not coordinate my schedule to be involved in the field data collection, but I was well-supported by Jake who showed me as much of the process as he could when I visited campus, always sent me high-quality data, and was available for questions whenever I had them.

Thank you to the entire AgriLife team and Dr. Starek for working with me as I pursued this degree while working full-time in another city. Your willingness to meet when I could get time off from work, and to have video or phone conferences, made completing this research and my degree possible.

I would also like to thank the USDA for their support through the internship award they generously awarded me in 2017. Special thanks as well to Dr. Xavier Gonzales, for providing guidance and support as part of the USDA internship program, and for making conference trips possible for me.

Finally, I would like to thank my family and friends for encouraging and believing in me. Thank you for listening to all my frustrations and sharing my hopes while I pursued this degree. Special thanks to my father, Dr. Harold Klemcke, for helping me sort through my statistical analysis, even when he was working on his own research. Thank you for lending me your determination and resolve to help me complete this degree.



## TABLE OF CONTENTS

CONTENTS	PAGE
ABSTRACT.....	v
DEDICATION.....	vi
ACKNOWLEDGEMENTS.....	vii
TABLE OF CONTENTS.....	ix
LIST OF FIGURES .....	xii
LIST OF TABLES.....	xvii
CHAPTER 1 .....	1
1.1 Introduction.....	1
1.2 Precision Agriculture and Remote Sensing .....	1
1.3 Unmanned Aircraft Systems and Grazing Land Management .....	3
1.4 Structure-from-Motion (SfM) Photogrammetry .....	7
1.4 Study Purpose and Objectives .....	13
CHAPTER 2: STUDY AREA AND DATA COLLECTION .....	15
2.1 Study Area .....	15
2.1.1 Plants and Soils .....	17
2.1.2 Brush Field.....	20
2.1.3 Sandy Field .....	21
2.1.4 Tifton Field .....	22
2.2 UAS Data Collection .....	23

2.3 Field Data Collection .....	27
CHAPTER 3: METHODOLOGY .....	31
3.1 UAS Image Processing .....	31
3.2 Ground Point Classification .....	32
3.3 Digital Elevation and Surface Models .....	36
3.4 Quadrat Identification .....	40
3.5 Vegetation Indices .....	44
CHAPTER 4: RESULTS AND DISCUSSION.....	47
4.1 Results.....	47
4.1.1 UAS-SfM Point Cloud Classification.....	47
4.1.2 Canopy Height Models .....	52
4.1.3 Vegetation Indices vs Field Measurements .....	54
2016 Results.....	56
2017 Results.....	60
Combined Results .....	65
4.2 Discussion.....	67
4.2.1 UAS-SfM DEM Products for Grazing land Management.....	67
4.2.2 UAS Vegetation Indices for Forage Estimation .....	68
Comparison of Flights.....	68
VI Assessment .....	70

Field Measurements .....	71
Potential Sources of Error: Pixel Contamination.....	71
Potential Sources of Error: Lighting Conditions .....	72
CHAPTER 5: CONCLUSION AND FUTURE WORK .....	74
5.1 Future Research .....	75
REFERENCES .....	77
LIST OF APPENDICES.....	85
APPENDIX 1: MONTHLY FLIGHT RESULTS .....	86
APPENDIX 2: UAS-SfM Point Cloud Metrics vs Forage Measure.....	90
APPENDIX 3: Point cloud classification Code .....	92

## LIST OF FIGURES

FIGURES	PAGE
Figure 1. Absorption and reflectance of the electromagnetic spectrum observed in plants [10]....	3
Figure 2. Example of a 3D point cloud, seen in LAStools software. ....	7
Figure 3. An illustration of how an SfM point cloud is generated from multiple camera positions [29]......	9
Figure 4. A DEM (left), showing the bare-earth surface. A DSM (right), showing trees and other features along with the underlying surface [32]. ....	11
Figure 5. The TAMU AgriLife Research Beeville Station is located in Beeville, TX. ....	15
Figure 6. The Beeville Station is used for grazing Brahman-influence cattle, like the ones shown above [44]. ....	16
Figure 7. Relative sizes and locations of the fields at the Beeville Station. ....	17
Figure 8. A huisache plant [46]......	18
Figure 9. A mesquite tree [47]......	19
Figure 10. (a) A field of coastal bermudagrass (left) [48]. (b) A stand of buffelgrass (right) [49]. .....	20
Figure 11. Brush field at the Texas A&M AgriLife Research Beeville Station. ....	21
Figure 12. Sandy field at the Texas A&M AgriLife Research Beeville Station.....	22
Figure 13. Tifton field at the Texas A&M AgriLife Research Beeville Station.....	23
Figure 14. The senseFly eBee mapping drone used in the 2016 flights (left), and the senseFly eBee SQ agricultural drone used in the 2017 flights (right). ....	24
Figure 15. The normalized response spectrum (left) for the Canon Power Shot S110 NIR Camera, and the corresponding appearance of vegetation [53]......	24

Figure 16. (a) The eBee SQ main body sensor (left) and (b) the sunshine/irradiance sensor (right) [57].	25
Figure 17. Spectral sensitivity of the eBee SQ’s irradiance sensor (left) and main sensor (right). The red-edge band is shown in purple, NIR in black [57].	26
Figure 18. An example of the PVC quadrat frames and targets used for the 2016 flights. ....	27
Figure 19. The field map used to help place the quadrats for each of the Sandy Field flights. ....	28
Figure 20. The field map used to help place the quadrats for the Tifton field.....	28
Figure 21. Initial point cloud classification method using LAStools. ....	32
Figure 22. The iterative classification workflow. ....	35
Figure 23. The UAS-SfM-derived digital elevation model for the October 2016 Tifton field flight.....	37
Figure 24. The UAS-SfM-derived digital surface model for the October 2016 Tifton field flight. ....	38
Figure 25. The smoothed DEM for the July Brush Field flight.....	39
Figure 26. The smoothed DEM for the July Brush Field flight, visualized with contours.....	40
Figure 27. Quadrat layout for the Sandy Field. Heads-up digitized from the June 2016 data. ..	41
Figure 28 (a). The outline of a quadrat is shown here in red (left). The white pixels beneath it represent both the quadrat PVC piping and the reflective halo of pixel contamination surrounding the piping. (b) The interior traced quadrat area shown in bold black within the square quadrat boundary (right). Raster pixels represent NDVI values.....	42
Figure 29. (a) An example of the false-color image created by combining the red, green, and NIR bands (left). (b) Green vegetation appears brighter in the NIR band (right). ....	46

Figure 30. The Sandy Field test areas: (a) Field; (b) Tree Stand; (c) Pond; (d) Lone Tree; (e) Building Roof.....	48
Figure 31. The Tifton Field test areas: (a) Building Roof; (b) Tree Stand; (c) Lone Tree; (d) Planted Field; (e) Adjacent Field .....	48
Figure 32: Percent ground points for the 2016 Sandy Field flights in the test areas. ....	49
Figure 33: Percent ground points for the 2016 Tifton Field flights in the test areas. ....	50
Figure 34. Point counts and densities per test area for the 2016 Sandy Field flights. ....	51
Figure 35. Point counts and densities per test area for the 2016 Tifton Field flights. ....	51
Figure 36. The difference surface created from the October 2016 UAS-SfM-derived DEM and DSM.....	53
Figure 37. The measured plant heights vs difference raster heights for the interior quadrat areas (October 2016 flight). ....	54
Figure 38. Uncontaminated areas (m <sup>2</sup> and %) for the 2016 and 2017 quadrats. ....	55
Figure 39. Correlation between field measures and vegetation indices by field for the 2016 flights. ....	57
Figure 40. Performance of each of the vegetation indices for each field measurement by field for the 2016 flights. ....	59
Figure 41. P-values resulting from the linear regression analysis for the 2016 flights. ....	59
Figure 42. Correlation between field measures and vegetation indices by field for the 2017 flights. The VIs using the red-edge band are indicated using a “RE” prefix.....	61
Figure 43. Performance of each of the vegetation indices for each field measurement by field for the 2017 flights. The VIs using the red-edge band are indicated using a “RE” prefix. ....	63
Figure 44. P-values resulting from the linear regression analysis for the 2017 flights. ....	64

Figure 45. Regression plot and marginal histogram of NDVI using the red-edge band and HM for the 2017 Sandy Field flights using the 1m quadrat size. .... 66

Figure 46. Regression plot and marginal histogram of ENDVI and crude protein for the 2017 Sandy Field flights using the 1m quadrat size. .... 67

Figure 47.  $r^2$  values based on the regression analysis of each VI vs HM for the 2016 flights. The mean uncontaminated quadrat area (%) is also shown as an area plot. .... 86

Figure 48.  $r^2$  values based on the regression analysis of each VI vs HM for the 2017 flights. The mean uncontaminated quadrat area (%) is also shown as an area plot. .... 86

Figure 49.  $r^2$  values based on the regression analysis of each VI vs average plant height in centimeters for the 2016 flights. The mean uncontaminated quadrat area (%) is also shown as an area plot..... 87

Figure 50.  $r^2$  values based on the regression analysis of each VI vs average plant height in centimeters for the 2017 flights. The mean uncontaminated quadrat area (%) is also shown as an area plot..... 87

Figure 51.  $r^2$  values based on the regression analysis of each VI vs % DM for the 2016 flights. The mean uncontaminated quadrat area (%) is also shown as an area plot..... 88

Figure 52.  $r^2$  values based on the regression analysis of each VI vs % DM for the 2017 flights. The mean uncontaminated quadrat area (%) is also shown as an area plot..... 88

Figure 53.  $r^2$  values based on the regression analysis of each VI vs % Crude Protein (CP) for the 2016 flights . The mean uncontaminated quadrat area (%) is also shown as an area plot..... 89

Figure 54.  $r^2$  values based on the regression analysis of each VI vs % CP for the 2017 flights . The mean uncontaminated quadrat area (%) is also shown as an area plot..... 89

Figure 55. The results of the regression analysis between the standard deviation of point heights with (a) HM (kg/ha); (b) Average Plant Height (cm); (c) %DM; (d) %CP. Values are for the 2016 flights only. .... 91



## LIST OF TABLES

TABLES	PAGE
Table 1. Comparison of sensors used for 2016 and 2017 flights [53], [57].	26
Table 2. A comparison of the UAS and field data collection parameters across the two field seasons.	29
Table 3. The GSD for each flight. 2017 GSD values are for the multispectral sensor only.	29
Table 4. The parameters used for the three classification iterations.	36
Table 5. Summary of quadrat identification for 2016 flights.	43
Table 6. Summary of quadrat identification for 2017 flights.	44
Table 7. Vegetation indices used and their associated equations.	45
Table 8. Summary of point cloud evaluation test areas for each field.	47
Table 9. Performance of VIs overall for the 2016 flights for both the Sandy and Tifton fields. The p-values indicate the significance of the regression models between each of the VIs and the field measurements.	58
Table 10. Performance of VIs overall for the 2017 flights. The p-values indicate the significance of the regression models between each of the VIs and the field measurements.	62
Table 11. Results filtered to display only those results whose p values are $< 0.05$ . Only the 2017 flights generated results where $p < 0.05$ .	66

## CHAPTER 1

### **1.1 Introduction**

Texas has long been a top producer of agricultural products in the United States. Nearly 52.6 million hectares of Texas farm and ranchland provide U.S. consumers with most of their beef and poultry. These same farms and ranches produce more forage and hay than any other state [1]. Within its borders, Texas holds the highest-value farm real estate in the nation with nearly a quarter-million businesses, over 98% of which are family-owned [2]. The United States relies heavily upon these farms and ranches to produce most of its livestock. The importance of the pastures and ranchland that support and nurture these animals cannot be overstated.

### **1.2 Precision Agriculture and Remote Sensing**

Precision agriculture is a revolution in modern agriculture. It has existed in some form since the 1930s when the Agricultural Administration of the United States began using aerial photographs to help measure cropland area [3]. This approach to modern agriculture focuses on acquiring and using data that enables land, crops, and livestock to be managed at as fine a scale as possible, both spatially and temporally. The goal of precision agriculture is to maximize the effectiveness of management practices and improve crop and livestock productivity while minimizing waste, costs, and negative impacts to the environment [3]–[5].

Precision agriculture provides farmers and ranchers with the tools needed to apply fertilizer, herbicides, and seed in the areas of greatest need at the most appropriate time [5]. While older methods of crop and range management use largely uniform application of fertilizer or pesticide across an entire field or pasture, precision agriculture allows fields and pastures to be managed according to their specific local topography, soil type, management history, and position in the larger landscape [5].

Precision agriculture requires the collection, processing, and analysis of large and detailed datasets that span large areas and multiple growing seasons. The process involves first collecting the data, mapping spatial and temporal variability, making a management decision, and implementing that decision. Remote sensing is a critical tool for precision agriculture, as it can provide all the data necessary to help inform management decisions [3].

Remote sensing depends upon different spectral responses of objects to electromagnetic radiation. Specifically for precision agriculture, the focus is on the spectral response of plants and soils to sunlight. Different objects can be identified by their spectral response, and the biochemical and physical properties of plants and soils can be measured by measuring their reflectance of light at different wavelengths. The spectral response of plants in particular is largely determined by the physical structure of plants and the plant canopy [6], [7].

When equipped with sensors, sensing platforms such as satellites, aircraft, unmanned aerial vehicles, balloons, tractors, and handheld sensors can be used to measure reflected electromagnetic radiation for plants and soils. Reflectance measurements in plants are inversely related to the amount of electromagnetic radiation absorbed by chlorophyll and other pigments [3], [5]. Different plant pigments absorb electromagnetic radiation at different wavelengths. Chlorophyll, for example, absorbs most strongly between 400 and 700 nm in the visible spectrum (Figure 1). By contrast, plants strongly reflect infrared radiation in the 700 to 1300 nm wavelengths [5]. The relationship between reflectance and absorption for various plant pigments has led to the creation of various spectral indices used to measure plant properties such as herbage mass (HM) and nitrogen content [5], [7]. Spectral indices combine reflectance signatures from multiple wavelengths to measure relative quantities of features of interest, such as soil or vegetation. A popular vegetation-focused spectral index is the Normalized Difference

Vegetation Index, or NDVI, which compares the near-infrared (NIR) reflectance to the amount of reflected visible light. NDVI can be used to measure the amount of healthy, growing vegetation in a multispectral image [8], [9].

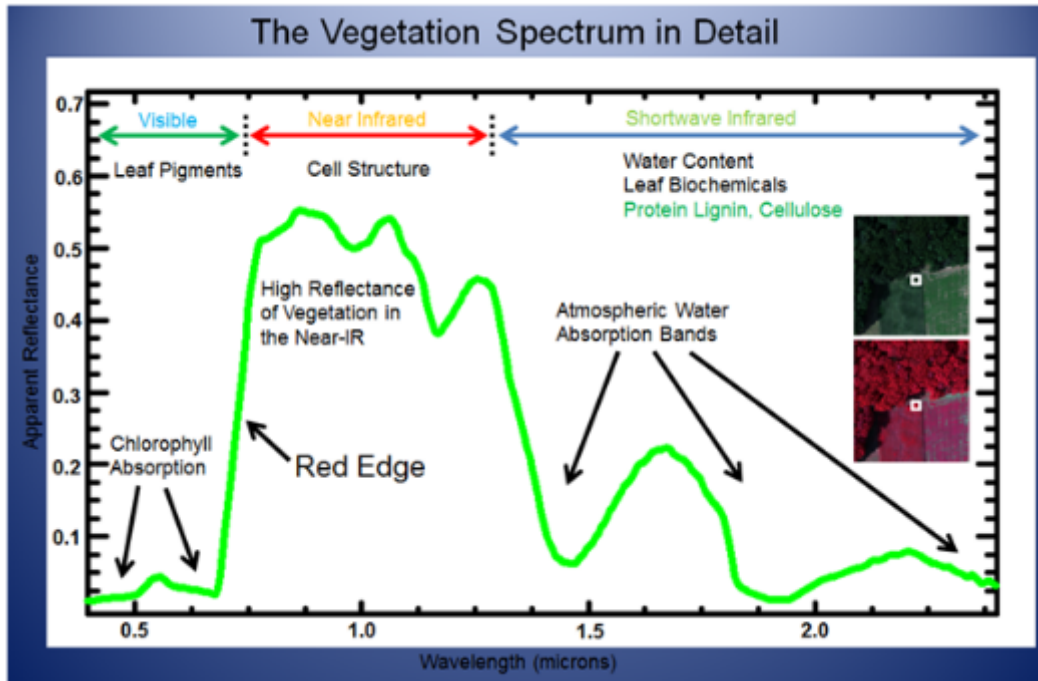


Figure 1. Absorption and reflectance of the electromagnetic spectrum observed in plants [10].

### 1.3 Unmanned Aircraft Systems and Grazing Land Management

Grazing land management refers specifically to the management of grasslands, shrublands, and savannahs which have the potential to be grazed by animals. These landscapes are generally marginal lands which are not suitable to be used for row crop production, but are useful for grazing livestock and harvesting hay or silage. Grazing lands can be affected by drought, insect and other pests and diseases, weed encroachment, and overgrazing. The total area of grasslands in the United States is vast, comprising over 35% of the country's total land area [11]. As grazing lands are often used to graze livestock, they can benefit from the same precision agriculture principles and technologies that are applied to crop production.

The use of satellite imagery has long been in use for precision agriculture, including grazing land management, and allows for the measurement of both plant and soil properties. Satellite imagery at the required spatial and temporal resolution for the management of grazing lands can prove prohibitively expensive for smaller farms and ranches. Satellite imagery also faces challenges such as cloud cover and insufficient spatial and temporal resolution [6], [7].

Imagery collected by UAS (Unmanned Aircraft Systems) can provide much greater spatial and temporal resolution than is currently obtainable with satellite data. Control over spatial and temporal resolution is crucial for avoiding cloud cover in the imagery, controlling the timing of data collection during the growing season, and obtaining ultra-high-resolution imagery with as few mixed pixels as possible. The resolution of UAS imagery also is sufficiently detailed to capture field sample quadrats used as ground truth to compare with collected reflectance data [6], [7]. In recent years, UAS have become increasingly more accessible to the public as they become smaller and less expensive. Sensor technology is following the same trend. UAS can be flown at a fraction of the cost of manned aircraft. Grazing lands are often in remote areas, making it easier to acquire permission for conducting small UAS flights and complying with regulations set by the Federal Aviation Administration (FAA) [3], [12]. The current study utilized small UAS, which is defined by the FAA as an unmanned aircraft weighing less than 55 pounds, including any sensors. A small UAS must be flown during the day, at or below 122 meters above ground level, and within visual line-of-site [13].

Use of UAS to measure and monitor vegetation for crop management and precision agriculture is well-established in many studies [14]–[17], but the same approach has yet to find widespread application in grazing land management [18]. The potential benefits are significant, as the productivity of cattle is determined primarily by forage quality [19]. Many of the same

methods used for precision agriculture can be applied to measure HM and nutritive value in a pasture to better inform grazing land management.

Reflectance data acquired using UAS equipped with multispectral sensors can be used to measure HM by analyzing the collected reflectance data using spectral indices. Vegetation indices do not measure biomass directly but are correlated with both plant biomass and the leaf area index (LAI), which is a measure of the total leaf area per unit area [20]. HM measurements for crop management and conservation can be used for cattle and grazing land management applications. Estimates of HM have been calculated by collecting and weighing samples from small quadrats of a known area taken from a field or pasture. The resulting estimates can be improved by increasing the number of samples, but it can only provide an estimate of the entire field. There is still a need for techniques that can collect data on plant health and HM rapidly for large areas [7], [18], [21].

Recently, techniques have been developed which use active optical LED sensors mounted on all-terrain vehicles, which can be driven over pastures and fields to provide a measure of plant health by measuring red and near-infrared (NIR) reflection [1]. Red and NIR reflection can be used to calculate several indices that correlate with green HM including the NDVI, Simple Ratio (SR), Soil Adjusted Vegetation Index (SAVI), and the Modified Non-Linear Vegetation Index indices (MNLI) [18]. A 2010 study by Trotter et al. [18] showed the log-transformed SAVI index accurately predicted the amount of green dry matter (GDM). That study also revealed substantial intra-field variation (4,000 kg GDM/ha) [18]. This further underscores the value of collecting data for an entire field or pasture compared with traditional destructive sampling or the transect method used by Trotter and colleagues.

Nutritive value is another parameter that can be measured from reflectance data captured by UAS. Nutritive value is a crucial metric as it provides a measure of plant chemical composition that is critical for determining if the forage will meet the animal's nutritional requirements [19], [22]. Nutritive value is measured in a laboratory setting and may include the digestibility of the available HM measured in vitro, and the concentrations of neutral- and acid-detergent fiber and crude protein [23]. Crude protein in forage is calculated as 6.25% times the nitrogen (N) content, which varies by plant species and maturity through the growing season [21]. Cattle eat about 1.25% of their body weight each day [19]. Hence, measures of the available nutritive value in a pasture can provide critical information for planning how long cattle can graze in a field before supplements are needed or the animals need to be rotated to another paddock [19], [21], [23].

Traditionally, nutritive value is estimated by testing field samples in the lab, which is a costly technique in terms of sample collection, processing, and disposal [23]. Nutritive value can also be measured indirectly by looking at various red and NIR indices, like NDVI [18], [21], [23]. While they can be costly in terms of technology, data storage, and data processing, non-destructive techniques can provide measures of nutritive value faster, at a lower cost, and with potentially greater accuracy and temporal resolution than traditional laboratory methods. The ratio of near-infrared to red, and the NDVI index, along with other vegetation indices, can be used to measure HM and plant stress [18], [21], [23].

Spectral indices can provide a measurement of chlorophyll in plants as a proxy measure of their nitrogen content, and hence their protein content [21], [23]. Previous studies have used a spectroradiometer mounted on a boom to measure plant reflectance, and have shown significant linear relationships between crude protein and HM with NIR reflectance ratios [23]. In

measuring crude protein concentration, it is important to consider the overall HM and growth to determine the concentration of crude protein [21], [23].

The use of spectral indices with multispectral UAS imagery can provide rapid, high-resolution data to measure important biochemical properties of plants for an entire pasture or field. A reliable, accurate, and automated procedure for collecting, processing, and analyzing these data would allow for powerful precision agriculture management methods to be applied to grazing lands.

#### **1.4 Structure-from-Motion (SfM) Photogrammetry**

In addition to measuring reflectance, imagery collected by UAS can be used to create three-dimensional models of the terrain. A technique called Structure-from-Motion (SfM) photogrammetry can be applied to overlapping image sequences collected from a UAS to derive three-dimensional (3D) point clouds of the land cover and terrain. A point cloud is a set of data points in space that represent a physical surface (Figure 2) [24].

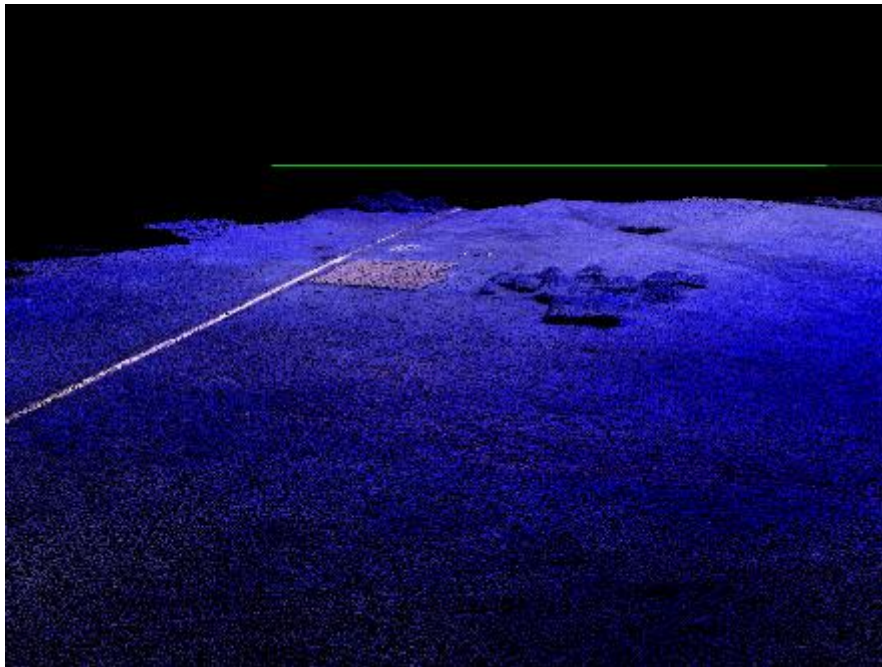


Figure 2. Example of a 3D point cloud, seen in *LAStools* software.



SfM offers an alternative to traditional photogrammetry, which requires more known parameters and controls in order to make measurements or a point cloud. Traditional photogrammetry requires the 3D location (X, Y, and Z positions) of the camera or control points to be known in order to triangulate and reconstruct positions within the photographed scene [25]. SfM does not require these positions to be known but instead calculates positions within a scene using feature matching between overlapping and offset images [25]. This approach makes SfM useful at multiple scales and ranges, and provides a relatively low-cost tool for three-dimensional modeling over traditional photogrammetry [25].

SfM has its origins in computer vision and uses feature recognition to identify features in multiple overlapping images [25]. SfM uses the Scale Invariant Transform (SIFT) approach which uses “cascade filtering” to help reduce the processing cost necessary to identify features that reoccur in multiple overlapping images in a scene [26]. While different software packages use varying algorithms, the SIFT approach generally identifies key points that are used to identify the same feature in multiple images, and allows feature identification and matching to be invariant even at different scales, orientations, and scene or object illuminations [26]. Images where the scale differences are extreme enough to fundamentally change the visible characteristics of a feature may be rejected by the algorithm [27]. The camera position and orientation, along with the three-dimensional scene geometry, are calculated by tracking these features from one image to the next. These calculations are estimated using a non-linear least-squares adjustment that is continually refined as more potential solutions become available from image pairs and matching key points [25].

There are many software packages available for processing UAS imagery, such as Pix4D. These software packages identify key points from overlapping images collected by a UAS to

create a sparse point cloud (Figure 3). The sparse point cloud is then densified by using derived camera positions as input into various densification algorithms. Different software packages use different algorithms to obtain a densified point cloud [28]. The resulting three-dimensional point cloud derived from the combination of all the overlapping images lacks absolute location or scale without the inclusion of ground control points or geotagging of imagery (or both). Ground control can be collected either during data collection or after; high-contrast targets with high-accuracy positions collected during the image collection provide the best results [25].

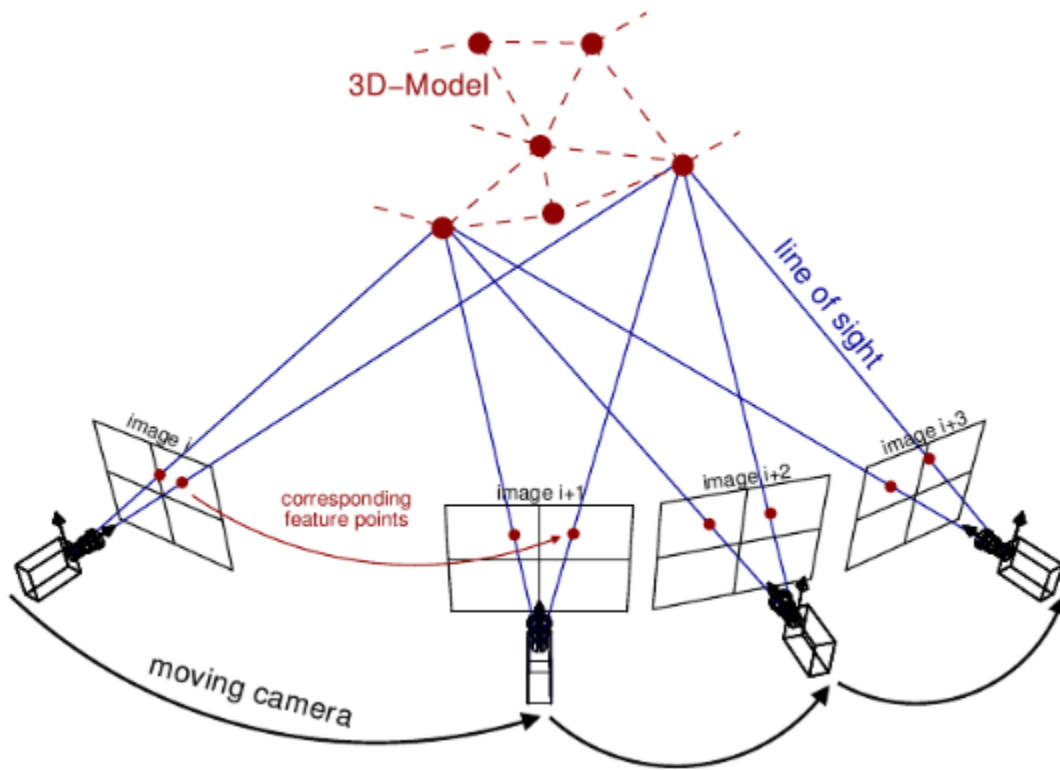


Figure 3. An illustration of how an SfM point cloud is generated from multiple camera positions [29].

Ground control points can be used to georeference the point cloud using a linear transformation (rotation/translation). Any corrections needed in the image alignment beyond a linear transformation can be applied and the point cloud re-constructed using the ground control points, to help reduce errors in the final point cloud. Most software packages also produce an

orthomosaic and digital surface model (DSM) along with the point cloud in the final output [28]. The DSM contains elevation values in a raster format for each location in the point cloud [30].

Data collection using UAS provides significant advantages over traditional photogrammetry, including the ability to use substantially lower-cost, consumer-grade cameras. The UAS platform itself is also much less expensive to obtain and operate than the specialized aircraft used in traditional aerial photogrammetry, although the type of UAS used can pose sensor limitations as it is much more restricted in terms of payload [31].

When using traditional photogrammetric methods, the imagery captured by a UAS may prove difficult to process due to lower-quality cameras, less stable flights, and off-nadir images taken from multiple altitudes [28]. Using a SfM approach largely avoids these issues as the camera interior and exterior orientation and position do not have to be specified, and SfM is capable of handling images of many different scales and orientations. In fact the inclusion of oblique-angle images along with nadir-view images from a UAS can help compensate for a dome-like deformation of elevation values that occurs in the point cloud as a result of self-calibration of lower-quality, consumer-grade cameras [28], [30].

SfM-derived point clouds can be used to derive digital models of the terrain and land cover. These terrain models can be used as another geospatial data product to inform grazing land management. Digital elevation models, or DEMs, map the “bare-earth” ground surface without any vegetation, buildings, or other non-ground features, and can be used to calculate slope and model terrain [22], [32]. Digital surface models, or DSMs, map the ground surface inclusive of non-ground features like vegetation. The difference between these two surfaces can be used to estimate biomass [32], [33]. Examples of both a DEM and a DSM are shown in Figure 4.

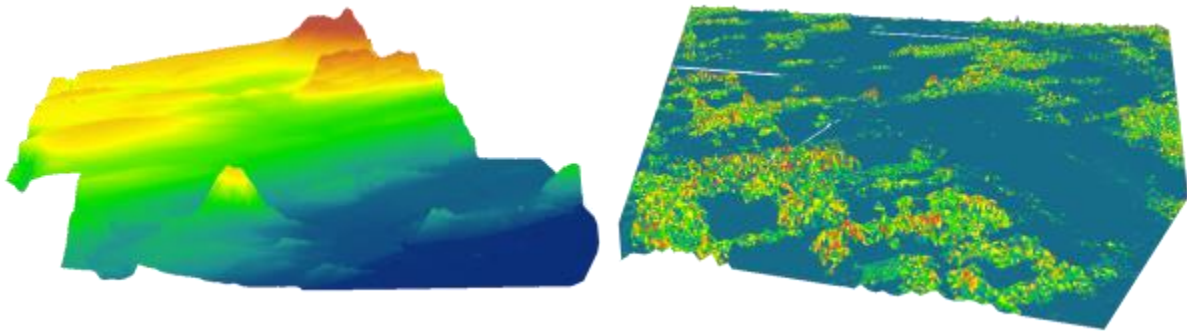


Figure 4. A DEM (left), showing the bare-earth surface. A DSM (right), showing trees and other features along with the underlying surface [32].

Recent studies have shown that UAS-collected point clouds can generate DEMs accurate within just a few centimeters [30]. In order to obtain this level of accuracy, a control network consisting of visible targets can be placed in the field ahead of the UAS flight and ideally located using Real-Time Kinematic (RTK) GPS [25]. This control network can then be used for accurate image registration and point cloud georeferencing. Ideally, ground control points (GCPs) are evenly distributed throughout the scene or site and with sufficient frequency to capture variation in terrain [25], [30]. Errors in GCP positioning will be propagated to the final SfM products, so positions of the control points must be as accurate as possible [28], [30].

3D point clouds can also be captured by relatively costly LiDAR (Light Detection And Ranging) sensors. LiDAR sensors use lasers to measure the distance to an object using the time elapsed from when the laser light is emitted and when it is returned. LiDAR sensors can record multiple returns from a single laser pulse. Returns represent multiple elevations ( $Z$ ) for a single ( $X, Y$ ) location [34]. Compared to LiDAR point clouds, SfM point clouds pose a particular challenge for classification as they generate a single elevation ( $Z$ ) for a given ( $X, Y$ ) location. No return information is provided using SfM, as with LiDAR. Ground points are generally classified by filtering for the lowest point in a given window [35], [36]. This can produce very good results when the actual bare earth surface is visible, but in imagery where the ground is not

visible the point cloud classification results are not reliable and can vary in accuracy across a dataset. SfM point cloud classification generally requires manual quality control and the identification and removal or correction of misclassified points [35].

SfM point clouds derived from UAS-acquired imagery can be useful for precision agriculture as they provide a high-resolution digital model of a field or pasture's canopy structure and exposed terrain. A high-quality DEM can be used to measure slope, elevation, and aspect. Combined with high-quality ground control, SfM point clouds can yield DEMs that can be used for multiple applications. Calculating the difference between an accurate DEM and DSM can be used to measure plant height, and slope information calculated from a DEM can be used to help determine if there are any areas within a pasture that are less likely to be grazed [22], [37].

As the use of UAS becomes more common, research into different techniques for using RGB, multispectral, and hyperspectral imagery captured by UAS for precision agriculture has increased [38]. Using UAS-based remote sensing to apply precision agriculture methods and principles to grazing lands can provide invaluable information to ranchers on plant health, which will in turn produce greater livestock yields at a lower overall cost [39], [40]. In order to ensure the health and value of their livestock, ranchers must provide adequate forage quantity and quality for their animals. Measuring and monitoring the amount and health of plants in pastures is therefore a constant part of grazing land management. Cattle require particular nutrients in their diet which must be supplemented when the forage quantity or quality is not sufficient. Current grazing land management practices rely on destructive sampling and laboratory testing to estimate forage HM and nutritive value. Pastures and fields are sampled using representative areas which are then tested in the laboratory to generate an estimate of the overall HM and nutritive value [38]. This is a labor-intensive process that can fail to capture the spatial

variability of important abiotic growth factors, including variations in soil types and topography [38], [39]. Destructive sampling can also prove impractical and inaccurate for very large areas, which may have remote and inaccessible sections that are rarely if ever measured directly. Finally, the results may not always be returned to the farmer immediately, limiting their benefit for altering grazing land management practices to meet the needs of livestock as they arise [6].

Remote sensing can provide a non-destructive, lower-cost alternative that allows for measurement of an entire pasture at a fraction of the time spent in the field [39]. It can also provide measurements for areas that would be difficult or impractical to access for destructive sampling methods. Photogrammetry and remote sensing performed with a UAS equipped with a digital RGB camera or multispectral sensor can provide 3D point clouds and reflectance data, respectively. Reflectance data can be used for many applications including measuring plant health and estimating other biophysical parameters in grazing lands. 3D point clouds can be used to estimate crop structure and derive digital terrain models to measure slope, aspect, and elevation. The management of grasslands using UAS provides timely and accurate data for the most effective application of the principles of precision agriculture.

#### **1.4 Study Purpose and Objectives**

The purpose of this study is to develop better methods for informing and refining grazing land management through estimation of forage nutritive value and quantity—including above-ground HM, nutritive content, and 3D structure—and by modeling terrain. This study uses photogrammetrically-processed RGB and multispectral imagery collected by UAS to generate 3D point clouds and reflectance maps. Point clouds are used in this study to create DSMs, and filtered to create DEMs, which are then used to calculate canopy height models. Raw point cloud structure is also used to analyze forage structure, including height. Reflectance

maps are used to create vegetation index rasters, which are in turn used to derive estimates of above-ground HM and nutritive value. Consistent correlations between reflectance image signatures and field measures could provide more accurate, complete, and detailed measurements of pasture forage with each UAS flight. This study has the following objectives:

- Create a successful filtering algorithm to classify the SfM point cloud generated from UAS-acquired imagery. Use the classified points to create accurate bare-earth DEMs.
- Calculate plant height and HM using DSMs and DEMs generated from the classified SfM point cloud.
- Determine which of four vegetation indices derived from multispectral data acquired using a UAS is most effective at predicting HM and chemical composition measured in the field.

## CHAPTER 2: STUDY AREA AND DATA COLLECTION

### 2.1 Study Area

Data for this study was collected at the Texas A&M Agrilife Research Station in Beeville, TX (Figure 5). The Beeville Station is approximately 567 hectares used to graze Brahman-influenced cattle [41]. Brahman-influenced cattle, shown in Figure 6, are the result of breeding Brahman cattle with other breeds, such as British or European breeds. These cross-bred cattle generally have a higher heat tolerance and are relatively hardier than their non-Brahman counterparts [42]. The Forage Management and Ecology Laboratory is located at the Beeville Station and researches sustainable forage systems, the use of native and non-native plants to improve livestock system productivity, and the management of forages in South Texas [43].



Figure 5. The TAMU AgriLife Research Beeville Station is located in Beeville, TX.





Figure 6. The Beeville Station is used for grazing Brahman-influence cattle, like the ones shown above [44].

The Beeville Station contains two experimental pastures, the “Sandy” and “Tifton” fields, which were used for this study. Flights for this study were flown in 2016 and 2017 during the growing seasons, between May and October. Flights were generally flown each month with some gaps due to scheduling conflicts. Another experimental field at the Beeville Station, called the “Brush” field, which has had little treatment for brush control over the last 25 years, was flown in early 2016 and was used for preliminary point cloud analysis and DEM generation, but was not included for subsequent analysis of the multispectral imagery. The relative positions of these fields within the Beeville Station are shown in Figure 7. More detail on the Beeville Station and its experimental fields are provided in the following sections, including the most common plant and soil types.



Figure 7. Relative sizes and locations of the fields at the Beeville Station.

### 2.1.1 Plants and Soils

There are several plant and soil types found throughout the Beeville Station, and within each experimental field. Huisache (*Vachellia farnesiana* (L.) Wight & Arn.) is a flowering invasive plant found in many Texas pastures and grazing lands, and is found throughout the Beeville Station. Huisache is a small tree in the Legume family, generally found in south Texas.

It is also called Sweet Acacia and can reach 4.6 m (15 feet) in height. Huisache is hardy and aggressive and prevents the growth of other forage plants that can be used by livestock. It can be grazed but provides poor nutritional content compared to other plants. It is commonly spread by grazing livestock and requires constant control to prevent its spread [45], [46]. An example of a huisache plant is shown in Figure 8.



Figure 8. A huisache plant [46].

Mesquite (*Prosopis glandulosa* Torr.) is a small to medium tree that is commonly found throughout Texas, including the Beeville Station. It has thorns on its branches and produces seed pods. The beans can be toxic, especially to cattle. The beans are also high in sugar which can cause digestive issues and inhibit the absorption of B-vitamins in livestock [47]. A mesquite tree is shown in Figure 9.



Figure 9. A mesquite tree [47].

Coastal bermudagrass (*Cynodon dactylon* [L.] Pers.) is a perennial grass found at the Beeville Station that grows from under- and aboveground stems. It grows well in different soil types and is highly adaptable. It is the most widely planted variety of bermudagrass in Texas and is drought- and grazing-tolerant [48]. Buffelgrass (*Pennisetum ciliare* (L.) Link) is a perennial grass considered to be good grazing for livestock and is also found at the Beeville Station. It is a perennial warm-season grass, like coastal bermudagrass [49]. Tifton 85 bermudagrass is a hybrid like Coastal bermudagrass. It is excellent for hay and livestock grazing [50]. Coastal bermudagrass and buffelgrass are shown in Figure 10a and Figure 10b, respectively.

Parrita-Olmos undulating and Parrita sandy clay loam soils are considered well-drained soils that are not prime for farmland. Weesatche fine sandy loam is prime farmland soil that is also well-drained [51]. These soils are found throughout the Beeville Station.



Figure 10. (a) A field of coastal bermudagrass (left) [48]. (b) A stand of buffelgrass (right) [49].

### 2.1.2 Brush Field

The Brush field is 17 hectares of uncultivated land, which is typically considered native grazingland in the region. The land was acquired by Texas A&M AgriLife in the early 1970s. The understory forage is occasionally grazed. Plant species include mesquite trees and huisache brush. Soils in this field are primarily Parrita-Olmos association, undulating soil [41]. The Brush field was only included for preliminary tests of the drone flights at the beginning of the study; it was not included in the final analysis. An aerial view of the Brush field is shown in Figure 11.



Figure 11. Brush field at the Texas A&M AgriLife Research Beeville Station.

### 2.1.3 Sandy Field

The Sandy Field, or large pasture, consist of 43.3 hectares planted to ‘Coastal’ bermudagrass in the early 1970s. Encroached weeds in this pasture include buffelgrass and old world bluestems (Kleberg’s bluestem [*Dichanthium annulatum*] and KR bluestem [*Brothriochloa ischaemum*]). This pasture is one of the rotational paddocks for grazing by cow-calf pairs, and has been harvested for hay in years of forage excess. Soils in this pasture consist primarily of Parrita sandy clay loam (loamy, mixed, superactive, hyperthermic, and shallow

Petrocalcic Paleustolls soil) and an area of Weesatche fine sandy loam (fine-loamy, mixed, superactive, hyperthermic Typic Argiustolls) [41]. An aerial view of the Sandy field is show in Figure 12.



Figure 12. Sandy field at the Texas A&M AgriLife Research Beeville Station.

#### *2.1.4 Tifton Field*

The Tifton Field, or small or front pasture, consists of about 5.3 hectares planted to Tifton 85 bermudagrass in 2011. It is harvested for hay annually. The Tifton Field is fertilized according to soil tests, and herbicide is applied to control broadleaf weeds as necessary.

Encroached weeds include old world bluestems. The soil consists primarily of sandy clay loam soil [41]. An aerial view of the Tifton field is shown in Figure 13.



Figure 13. Tifton field at the Texas A&M AgriLife Research Beeville Station.

## 2.2 UAS Data Collection

The 2016 flights were flown using a senseFly eBee mapping drone equipped with a Canon Power Shot S110 NIR camera. This camera collects data in the red, green, and NIR bands. The Sandy Field flights were flown at 120 m above ground level (AGL), with a 75% sidelap and 65% endlap. The Tifton Field was flown at 60 m AGL with an 80% sidelap and 65%



endlap [52]–[54]. The senseFly eBee used in the 2016 flights and senseFly eBee SQ used in the 2017 flights are shown in Figure 14. A full comparison of the sensors used in each year is shown in Table 1. Figure 15 shows the response spectrum for the Canon Power Shot S110 NIR Camera used in the 2016 flights, and how this response spectrum affects the appearance of vegetation compared to an RGB camera.



Figure 14. The senseFly eBee mapping drone used in the 2016 flights (left), and the senseFly eBee SQ agricultural drone used in the 2017 flights (right).

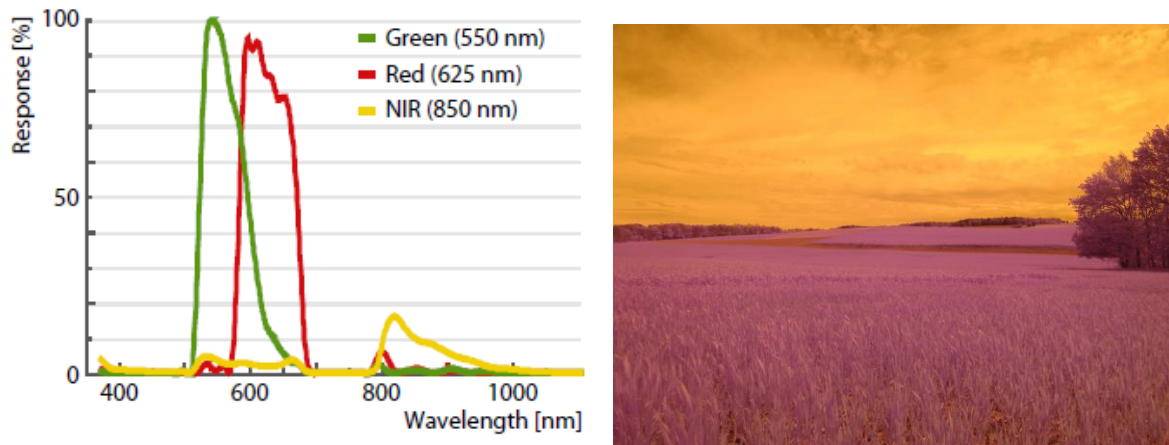


Figure 15. The normalized response spectrum (left) for the Canon Power Shot S110 NIR Camera, and the corresponding appearance of vegetation [53].

In 2017, the eBee SQ agricultural drone was used for all flights. This drone is equipped with the multispectral Parrot Sequoia sensor (Figure 16). This sensor contains a 16 megapixel

(MP) RGB camera and a 1.2 MP 4-band multispectral sensor that measures NIR, red edge, red, and green reflectance. It has an upward-facing irradiance sensor to help offset the effects of various lighting conditions on the resulting imagery (Figure 16). The irradiance sensor records the ambient light conditions in the same bands as the multispectral sensor. The intensity of ambient light conditions, which vary depending on cloud cover and time of day, can then be corrected for during image post-processing by software such as Pix4D which can use the data from the irradiance sensor as part of its image processing algorithms [55]. This makes flight data collected on days with different global lighting conditions more directly comparable [56].

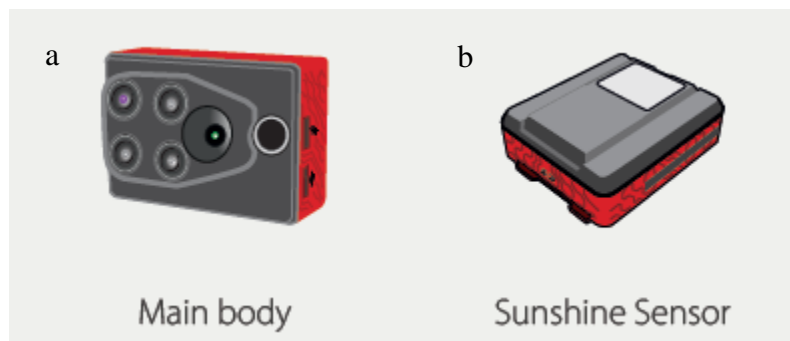


Figure 16. (a) The eBee SQ main body sensor (left) and (b) the sunshine/irradiance sensor (right) [57].

The eBee SQ multispectral sensor collects red-edge reflectance data in addition to red and NIR. Red-edge refers to a portion of the electromagnetic spectrum around 700 nm, where green vegetation shows sharp changes in reflectance [58]. This is a feature of green vegetation and is due to the presence of chlorophyll and the reflectance of NIR. The red-edge allows green vegetation to be clearly distinguished from dead vegetation and non-vegetation in the surrounding environment. Because it is a narrow spectral band, the red-edge is often measured indirectly by spectral indices that use combinations of red and NIR [58]. The spectral sensitivity of both the main body and sunshine irradiance sensors for the eBee SQ, including the red-edge band, are shown in Figure 17.

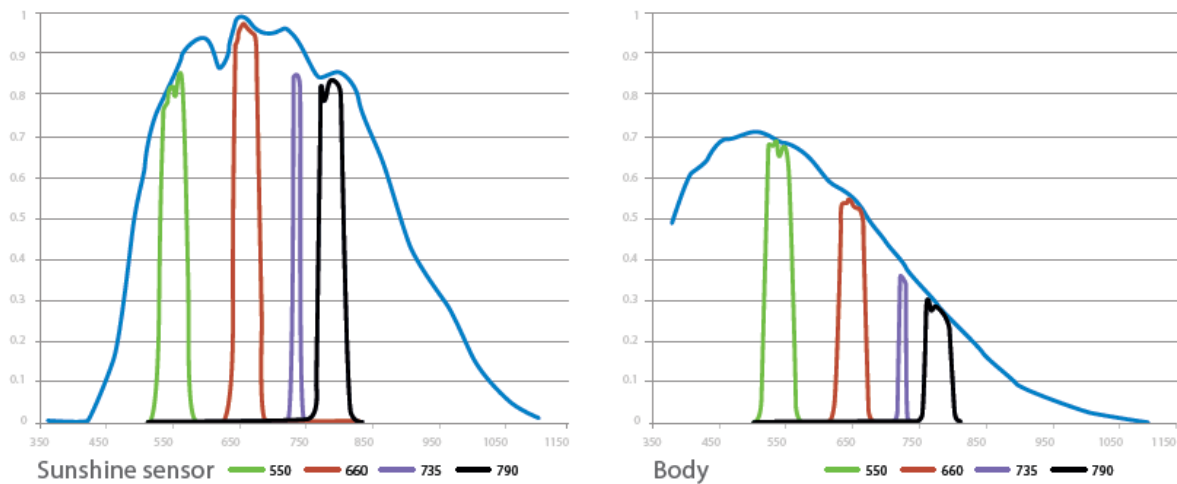


Figure 17. Spectral sensitivity of the eBee SQ’s irradiance sensor (left) and main sensor (right). The red-edge band is shown in purple, NIR in black [57].

The Sandy Field was flown at about 90 m above ground level (AGL) and had a 75% sidelap and 65% endlap, while the Tifton Field was flown at 36 m AGL with an 80% sidelap and 65% endlap. For both years, the flight control software used was senseFly’s eMotion Ag. This software allows for the use of imported field boundaries and the specification of a desired ground resolution for generating a flight path. The images collected during a flight are automatically geotagged by eMotion Ag; the final image mosaic is georeferenced using control targets placed in the field prior to data collection and located using RTK GPS [54], [59], [60].

Year	Sensor	Image Size	Reflectance Bands	Max fps	Max Shutter Speed	Weight w/o battery
2016	Canon Power Shot S110 NIR	12.1 MP	Red, Green, NIR	f/2.0	1/2000s	153 g
2017	Parrot Sequoia Main Body Camera	RGB: 16 MP Multispectral: 1.2 MP	Red, Green, Red Edge, NIR, RGB	f/1.0	Rolling shutter	72 g

Table 1. Comparison of sensors used for 2016 and 2017 flights [53], [57].

## 2.3 Field Data Collection

Before each flight, PVC quadrats were placed in the fields. In 2016, the quadrats were PVC pipe with a larger outer frame (0.5 x 0.5 m; 0.25 m<sup>2</sup>) and a smaller inner frame (0.33 x 0.33 m; 0.1 m<sup>2</sup>) centered inside as shown in Figure 18. The sampling frame design was to limit contaminated pixels from sunlight reflection [7]. In 2017 the quadrat sizes were larger (Table 2) and the different quadrat sizes were placed next to each other on the ground. Ten quadrats were placed in each pasture in a W-transect and areas of low, medium, and high HM selected to facilitate regression along a range of HM. Ground control targets were also laid in the fields to help with georeferencing the resulting images. An example of a PVC frame and a ground control target is shown in Figure 18. The ground control targets are painted black and white for radiometric calibration in the image processing described in Chapter 3.

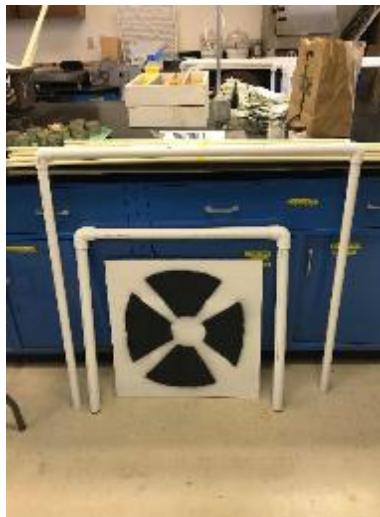


Figure 18. An example of the PVC quadrat frames and targets used for the 2016 flights.

For the 2016 flights, GPS coordinates were collected by the TAMU AgriLife team with a handheld GPS to collect approximate locations of the quadrats which then had to be identified in the imagery post-flight. A field map of planned quadrat positions was also available, and targets were placed to help identify quadrats in the imagery. Figure 19 shows the field map used to help

place the Sandy Field quadrats; Figure 20 shows the field map used to help place the Tifton field quadrats.

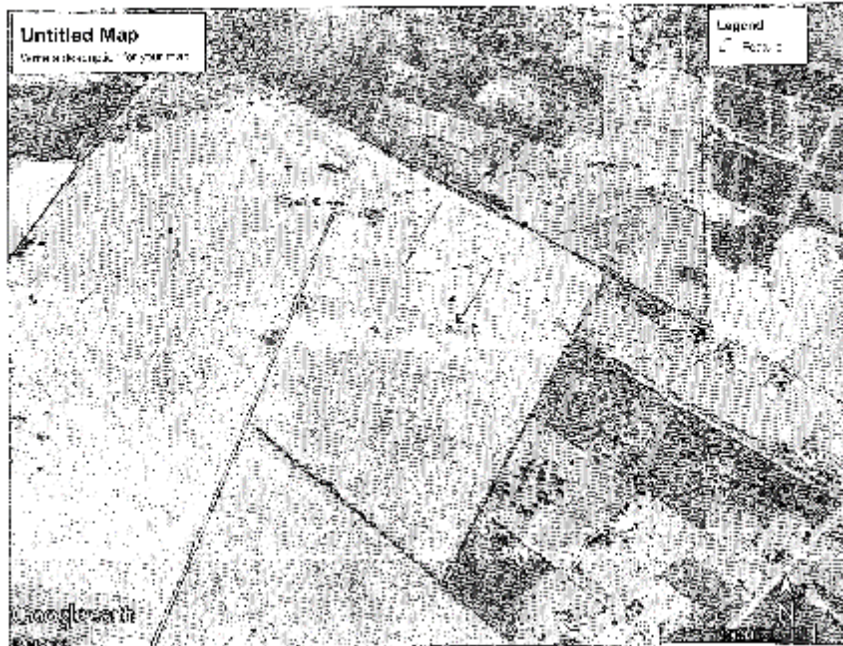


Figure 19. The field map used to help place the quadrats for each of the Sandy Field flights.

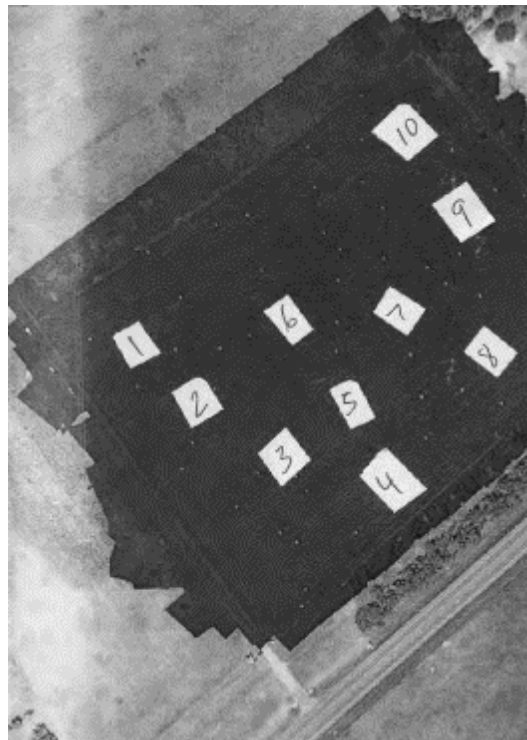


Figure 20. The field map used to help place the quadrats for the Tifton field.

For the 2017 flights, the quadrat sizes used were 1 m<sup>2</sup> and 0.5 m<sup>2</sup>. The quadrat sizes were enlarged to make the quadrats easier to identify in the imagery post-flight. RTK GPS positions were collected for each corner of the quadrats, which were placed side-by-side in the field. Table 2 summarizes the field and flight parameters for 2016 and 2017; Table 3 summarizes the ground sample distance (GSD) for each flight. The GSD is the average projected pixel size or spatial resolution of the images resulting from each flight; anything smaller than the GSD cannot be resolved by the sensor [61]. GSD is given for only the multispectral sensor in the 2017 flights.

Year	UAS	Sensor	Flying Height (m)	Quadrat Sizes (m <sup>2</sup> )	Quadrat Positioning
2016	eBee	Canon Power Shot S110 NIR	Sandy: 120 Tifton: 60	0.5	Handheld GPS
2017	eBee SQ	Parrot Sequoia Multispectral Sensor	Sandy: 90 Tifton: 36	0.5 1.0	RTK GPS

Table 2. A comparison of the UAS and field data collection parameters across the two field seasons.

Flight Date	Average GSD (cm) Sandy Field/Tifton Field
6/21/2016	4.36/4.61
7/29/2016	4.4/2.33
9/1/2016	4.36/2.66
10/21/2016	4.48/2.3
5/24/2017	7.74/5.26
7/3/2017	6.94/5.15
8/4/2017	6.65/5.47
9/15/2017	7.11/5.38

Table 3. The GSD for each flight. 2017 GSD values are for the multispectral sensor only.

The Texas A&M AgriLife team collected field data from inside each quadrat area after each flight. Plant height was measured using three randomly chosen locations within each

quadrat and then averaged. Plant height was measured from the ground to the top of the plant; the plant was not touched or manipulated for these measurements [62]. The forage within the inner frame of each quadrat was then sampled by hand-cutting the forage down to the ground level. Each sample was weighed, then dried at 65° C until a constant weight was achieved. The dried samples were then weighed and HM calculated. Samples were then ground to at least 1 mm in a Wiley Mill and analyzed for dry matter [63] and crude protein content by combustion in a Leco analyzer [64]. The resulting values for average plant height, HM, dry matter, and crude protein per quadrat, field, and flight were provided to the author in a spreadsheet for comparison with the UAS-collected data. The method for comparing the field measurements and the UAS data is explained in the following chapter.

## CHAPTER 3: METHODOLOGY

### 3.1 UAS Image Processing

After each flight, the data collected by the UAS must be processed to generate point clouds and reflectance maps. The data was downloaded from the sensor (the Canon s110 for the 2016 flights, and the Parrot Sequoia Multispectral sensor for the 2017 flights) and uploaded into Pix4D. For both years, the ground control target positions were used both to help georeference the images and to help radiometrically calibrate the images. This radiometric calibration corrects reflectance values in images based on the reflectance values recorded for the calibration ground control targets. The 2017 Parrot Sequoia multispectral imagery was processed using Pix4D's Ag Multipsectral processing template along with the calibration targets [65], [66].

The processing workflow followed by the software makes use of the SfM algorithms described in Chapter 1. Keypoints found in the overlapping images are identified and used to find areas in overlapping images that match. The matching keypoints along with the input GCPs are then used in automatic aerial triangulation and bundle block adjustment algorithms, resulting in a georeferenced orthomosaic, a densified point cloud, and a DSM [67]–[70]. The orthomosaic is then radiometrically corrected using calibration targets that were placed in the field. These targets allow the orthomosaic to be corrected for variations in reflectance due to variations in incoming sunlight irradiance, vignetting, sensor response, and camera parameters [71]. For the 2017 imagery, the software uses data from the sunlight/irradiance sensor along with the calibration targets to help radiometrically calibrate the orthomosaic [65]. The radiometrically-calibrated orthomosaic provides a more accurate reflectance map that can then be used to extract and measure the spectral response of objects captured in the UAS-collected imagery [71], [72].



### 3.2 Ground Point Classification

Point clouds generated from processed imagery collected by UAS provide a highly detailed snapshot of the terrain traversed during the UAS flight [70]. The detail of a UAS and SfM-derived, or UAS-SfM, point cloud can be comparable to the detail in a LiDAR-derived point cloud, with the key difference that UAS point clouds lack return information that can be used to classify the points in the point cloud [70], [73]. As discussed in Chapter 1, UAS-SfM generated point clouds do not penetrate vegetation like LiDAR and therefore can only capture the ground surface when it is visible to the sensor [73]. UAS-SfM-derived point clouds can provide both the detail and accuracy needed for highly accurate HM estimations, provided the ground surface is visible enough to allow for successful point cloud classification [74]. If the UAS-SfM point cloud is classified successfully, HM can be calculated by subtracting the DSM from the DEM, and plant height can be derived by looking at the elevation differences between the same two surfaces [74].

In order to classify the UAS-SfM point cloud, the point cloud was imported into LAStools [75], a set of C++ scriptable tools that are able to efficiently handle large point cloud datasets. LAStools has a set of tools designed for point cloud processing, including point cloud classification. Initially the recommended sequence [76], shown in Figure 21, was used on the densified point cloud:



Figure 21. Initial point cloud classification method using LAStools.

The recommended sequence shown in Figure 21 represents a single iteration of processing the point cloud data. The point cloud is first indexed, which creates an adaptive

quadtree of the data. This quadtree allows data to be processed much faster as the points can be “found” by the algorithms much more quickly in subsequent classification routines [77]. Next the data is tiled. Tiling creates smaller subsets of the data which also helps improve processing speed [78]. Sorting the points in their z-order within each tile acts like a vertical index [79]. These first three steps in the process all help facilitate the classification algorithm by creating a vehicle by which the classification algorithm can traverse the densified point cloud quickly and improve the results of classification [76].

The classification routine used in LASTools is based on a filtering algorithm that creates a Triangular Irregular Network, or TIN [80], and compares points from the UAS-SfM point cloud within a moving window. In the absence of return information, the relative heights of points within this moving window are compared; the lowest points are classified as “ground” points. The moving window is defined by the “step size” parameter. The step size is the size of the moving window. A step of 5 m will compare points within a 5 m area [81]. The difference between ground and non-ground points are defined by two additional parameters: the “spike” and “bulge.” The spike parameter helps remove noise in the point cloud by removing points that are above or below the specified value. For instance, a spike size of 0.5 m will remove up- and down-spike points that are above or below 0.5 m from their neighbors within the step [81]. Finally, the bulge parameter constrains the tentative surface, defined by the TIN, being created in the algorithm [80]. The bulge defines how much the TIN can undulate up and down [81]. For instance, a bulge of 1.0 m will allow for ground points that create a surface that has undulations

no higher or lower than 1 m. Any points that create a larger bulge in the TIN will not be classified as ground [81].

The last step in the recommended sequence shown in Figure 21 merges the tiles used for processing into a new, classified point cloud [78]. Review of the results from this initial process showed a great deal of misclassified points. While large features such as trees and buildings were correctly classified as non-ground points, most of the forage in the fields was incorrectly classified as ground. The initial results precluded the use of the point cloud for creating a bare-earth DEM, and for use of that DEM along with a DSM created from the same classified point cloud for measuring plant height and HM [74].

In order to avoid misclassifying the field forage as ground, an iterative approach was used that followed the recommended sequence shown in Figure 21 but with progressively larger tiles, and progressively larger step, spike, and bulge parameters. This approach removes non-ground points on progressively larger scale within the point cloud. The misclassified points from the process shown in Figure 21 are a result of the local and relative comparison that is done by the classification algorithm. In order to classify relatively low-lying points representing the forage in a field as non-ground, the step, spike, and bulge parameters must be defined so as to limit the relative comparison to only the bare-earth surface and the forage plants [81]. However, the classification algorithm must also be able to distinguish between the bare-earth surface and larger features, such as stands of trees and large buildings. In short, a single step, bulge, or spike parameter cannot correctly classify both low-contrast changes in elevation, such as grasses against the bare ground, to higher-contrast changes in elevation, such as trees and buildings

against the bare ground. In order to capture both large and small changes in elevation, an iterative approach was used and is shown in Figure 22.

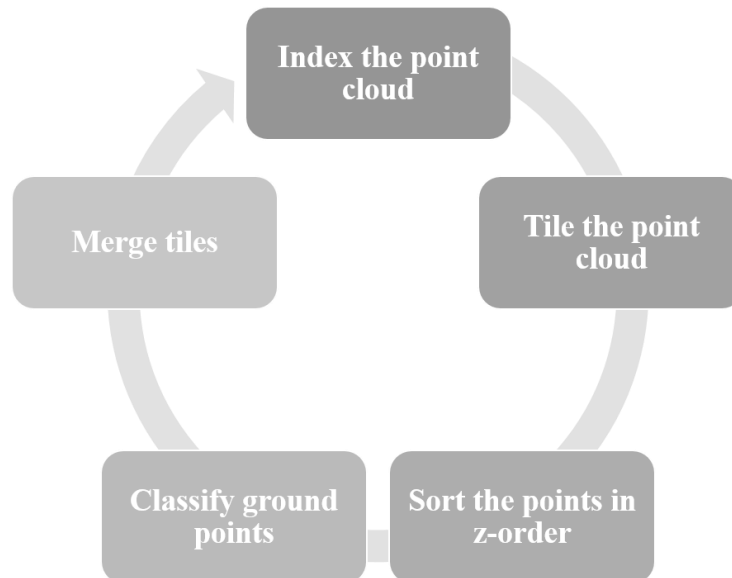


Figure 22. The iterative classification workflow.

The iterative process is repeated three times, each time increasing the tile size, step size, spike size, and bulge size. In the first iteration a very small tile size is used along with very small step, spike, and bulge parameters. The small step size filters non-ground points in a very small area with high sensitivity to small differences in elevation. The small step size will capture the lowest points within a very small moving window. The purpose of this first iteration is to try and capture only the lowest points in areas of low relief, such as in the planted Tifton 85 field, where large areas are devoid of trees and only have low grasses. The remaining two iterations serve to remove non-ground points from the initial classification pass by gradually increasing the step and tile size, and by increasing the spike and bulge tolerances. As the tile size increases, artifacts along the edges of tiles are smoothed. As the step size increases, relative heights between points are compared at a larger and larger scale, preserving ground points at a small scale, but removing them at larger scales. For example, the first pass retains valid ground points

between rows in a planted field, while the second and third passes remove invalid ground points from low berms and treetops. See Table 4 for the values used for each parameter in each iteration. These values were determined by testing incremental changes in the number of passes, tile size, step size, spike and bulge sizes and comparing the resulting classified point cloud to the UAS orthomosaic to see if improvements in classification were achieved. See Chapter 4 for an explanation of the results of these comparisons. If large areas of forage in pastures were classified as ground, or if large non-ground features such as trees or buildings were classified as ground, the parameters were adjusted. Additional iterations were added until improvements in the classification of the forage area of the fields were no longer apparent.

<b>Iteration</b>	<b>Tile Size (m)</b>	<b>Step (m)</b>	<b>Spike (m)</b>	<b>Bulge (m)</b>
<b>1</b>	250	1	0.05	None
<b>2</b>	500	5	0.1	None
<b>3</b>	1000	50	0.2	1

Table 4. The parameters used for the three classification iterations.

### **3.3 Digital Elevation and Surface Models**

The classified point clouds were imported into ArcGIS Desktop software to create bare-earth DEMs and DSMs. The goal of creating these two surfaces from the point cloud is to use them in creating detailed terrain and slope models, and to derive measures of plant height and HM. Ground points from the classified point clouds were used to create DEMs, which were created by generating a raster surface from the ground points in the classified point cloud. The average point spacing of the point cloud was used to determine an appropriate raster cell size. The raster cell size was set to 1 m, slightly larger than the average point spacing in the point clouds, to help smooth out any gaps where the point spacing was larger than the average value. A binning algorithm was used, which uses a moving window similar to the step used in the classification algorithm [82]. The binning algorithm was set to use only the lowest point within

the moving window to further help capture only the bare-earth points for the output DEM. A 1 m window size was used for the binning method as the output DEM resolution was set to 1 m so the value used for a single raster cell would reflect the elevation within the same area. Finally, nearest neighbor interpolation was used to create the output DEM, which assigns raster cell values based on the nearest point value to the raster cell center [83]. Figure 23 and Figure 24 show examples of the DEM and DSM derived from the UAS-SfM point cloud, respectively.

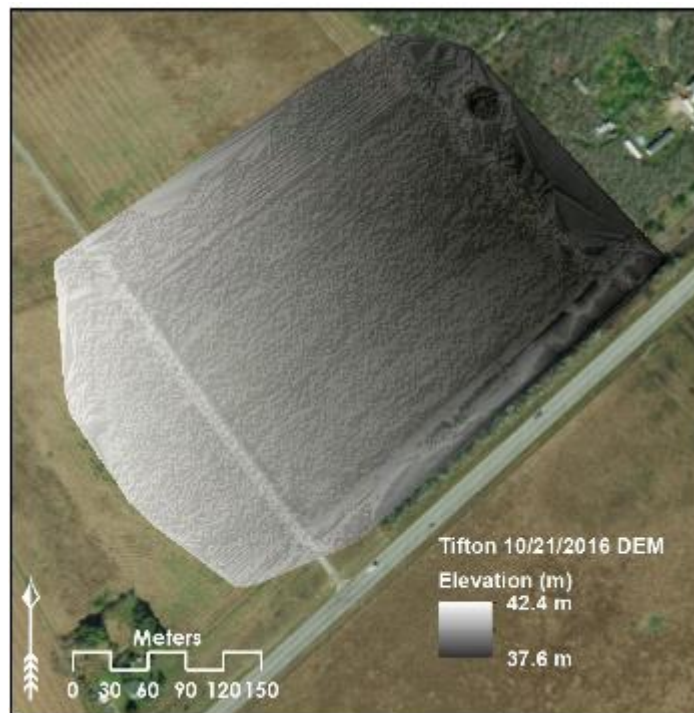


Figure 23. The UAS-SfM-derived digital elevation model for the October 2016 Tifton field flight.

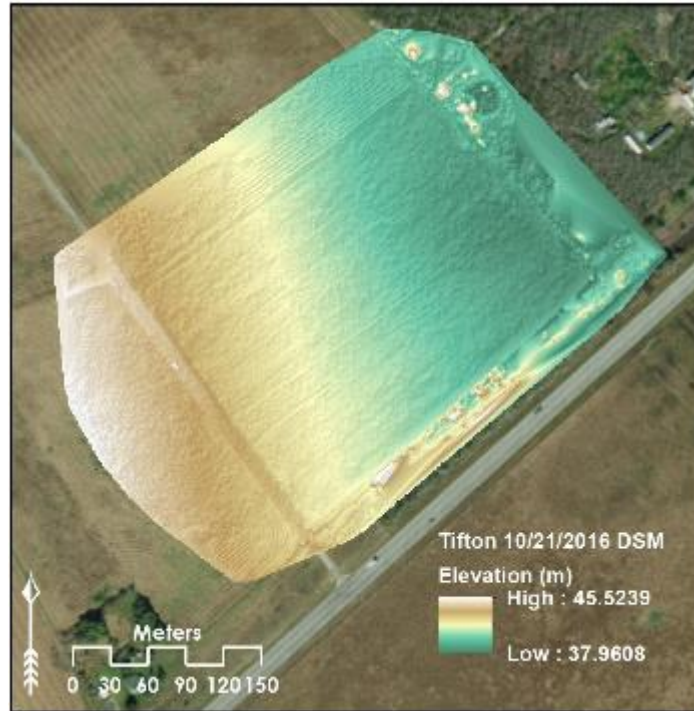


Figure 24. The UAS-SfM-derived digital surface model for the October 2016 Tifton field flight.

Attempts to improve the DEM surface so it could be used to generate a slope map were made by applying focal statistics to the DEM surface. The focal statistics used an average of values in a moving window across the DEM surface in an attempt to smooth the DEM [84]. This approach was used with a UAS-SfM DEM surface that was generated from the July 29 flight over the Brush field. Contours were generated at 0.1 m intervals to help visualize the smoothed DEM surface. The smoothed UAS-SfM-derived DEM for the Brush field is shown in Figure 25 with contours in 0.5-m intervals to help visualize the topographic surface.

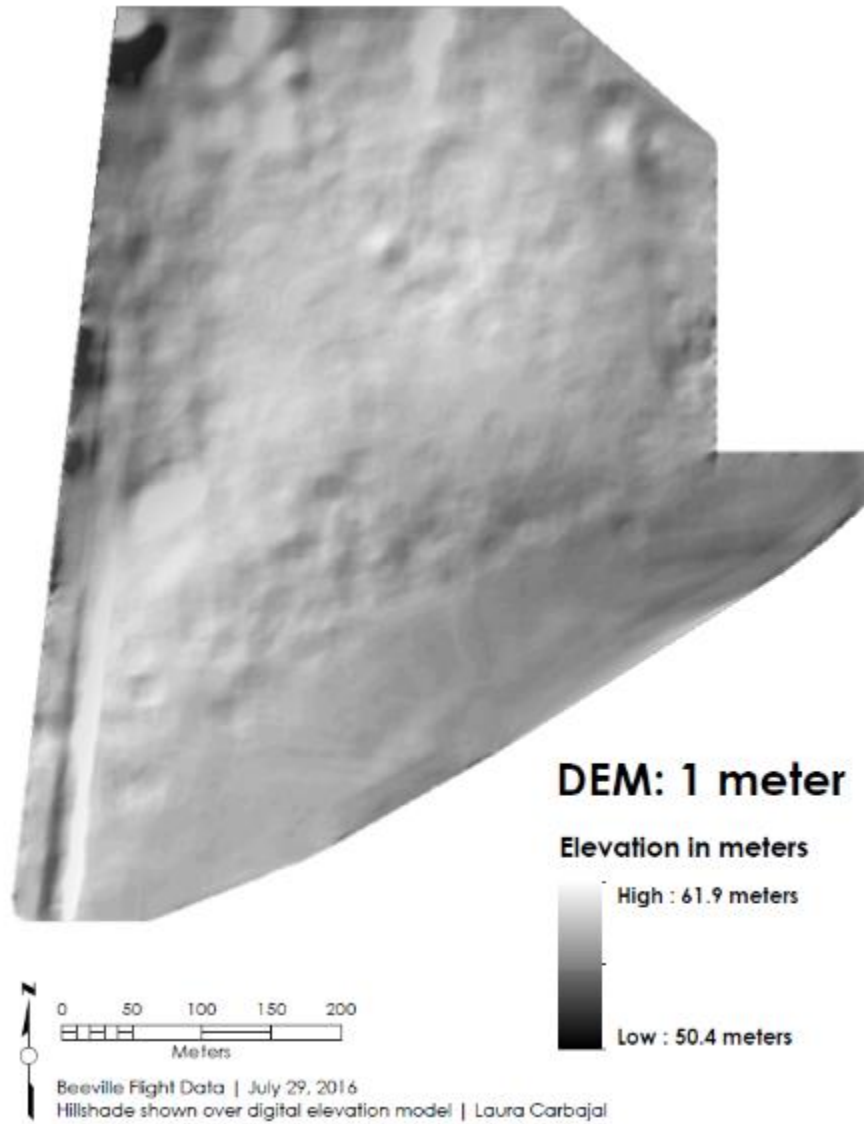


Figure 25. The smoothed DEM for the July Brush Field flight.



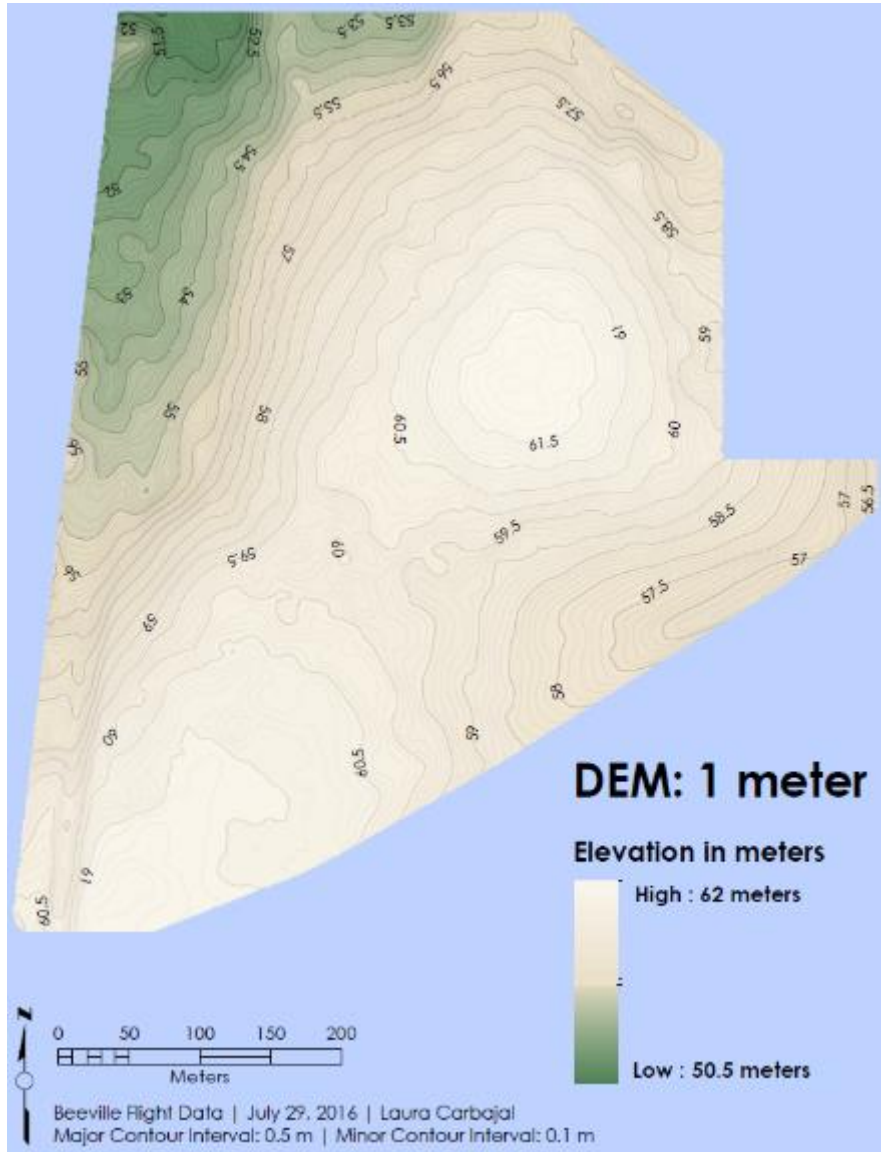


Figure 26. The smoothed DEM for the July Brush Field flight, visualized with contours.

### 3.4 Quadrat Identification

The PVC quadrats placed in the field before each flight must be identified in the UAS orthomosaic. The location of the quadrats is critical for comparing UAS-derived measurements from the classified point clouds, DEMs, and vegetation index rasters (described in the following section) with the measurements taken in the field and processed in the lab. The UAS-derived estimations of plant height and biomass, along with the spectral indices calculated from the

radiometrically-corrected UAS orthomosaic, are compared to the field measurements taken within each quadrat to see if the UAS-derived measurements can predict or significantly correlate with the field measurements.

For the 2016 field season, quadrat locations were heads-up digitized using the handheld GPS locations combined with visual inspection of the orthomosaic within about 3 meters of each GPS point. Only 60% of the quadrats could be positively and unambiguously identified from the 2016 field season. While field maps of the quadrats were available (Figure 19 and Figure 20), and approximate GPS positions were provided for almost all the 2016 flights, there were many instances where the quadrat simply wasn't visible in the orthomosaic. The height of surrounding vegetation and the flying height of the UAS were some of the factors that affected the visibility of quadrats in the orthomosaic.

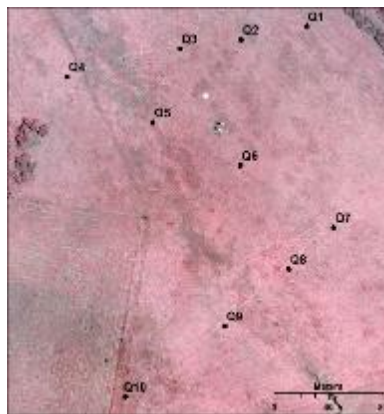


Figure 27. Quadrat layout for the Sandy Field. Heads-up digitized from the June 2016 data.

Quadrats that were identifiable in the 2016 orthomosaic were heads-up digitized by specifying the known length and deflection (90 degrees) of each quadrat side. Figure 27 shows the heads-up digitized quadrats from the June 2016 flights on the June 2016 orthomosaic. Two quadrat sizes were used in 2016, one inside the other, modeled after the 2014 Wang study. Only

the outer, larger quadrat (0.5 m<sup>2</sup>) is visible in the 2016 imagery. The smaller 0.1 m<sup>2</sup> within the 0.5 m<sup>2</sup> frame was not visible in any of the orthomosaics.

Significant pixel contamination is present in the 2016 quadrats identified in the orthomosaic. This pixel contamination creates pixels with high reflectance values due to the high reflectivity of the quadrat frames, which were made of white PVC pipe. Pixel contamination creates areas of very high pixel values due to the reflection of light off the white plastic piping, which obscures the reflectance signatures of the vegetation in that pixel area. These pixels are “contaminated” because their spectral responses do not represent the underlying vegetation well, and so are not useful for analysis. Pixel contamination was significant in the 2016 flights. To help remove its effects, the interior areas that appeared to be least affected by the reflection of sunlight off the PVC pipes were heads-up digitized as well.

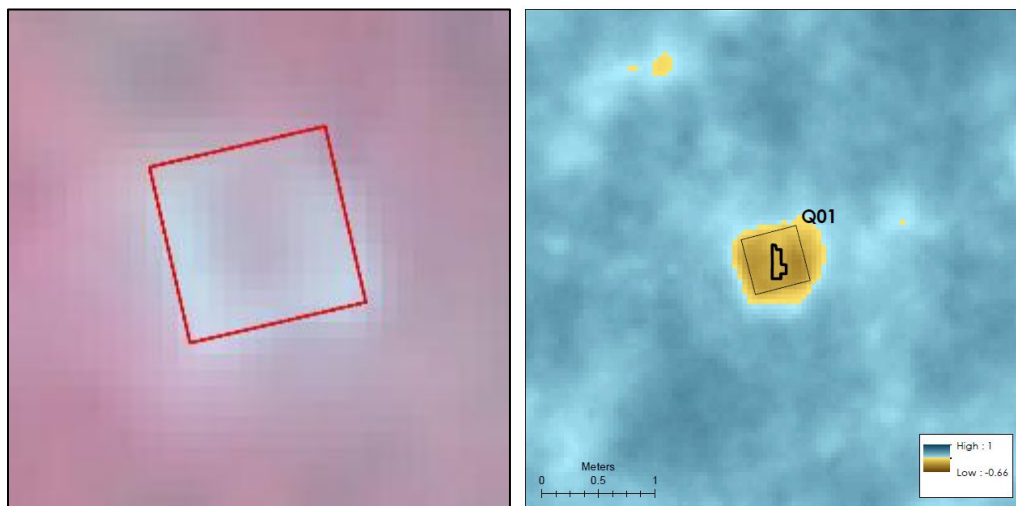


Figure 28 (a). The outline of a quadrat is shown here in red (left). The white pixels beneath it represent both the quadrat PVC piping and the reflective halo of pixel contamination surrounding the piping. (b) The interior traced quadrat area shown in bold black within the square quadrat boundary (right). Raster pixels represent NDVI values.

Identification of contaminated pixels was subjective, so contamination may have been better or worse than determined for this analysis. Contaminated pixels were identified via a visual inspection of each quadrat area. Pixels at or near the quadrat boundary that had a very

high value relative to the center of the quadrat were excluded. Since contamination gradually decreased away from the quadrat piping, however, there are likely varying effects of pixel contamination in the areas that were retained. This was not controlled for in the final analysis, and could benefit from a method that controls for pixel contamination, which may potentially yield different results.

After creating polygons for the quadrat frames, inner areas with little or no pixel contamination were heads-up digitized to create polygons. These polygon areas were used to extract the underlying raster data for analysis. Table 5 contains a summary of the number of quadrats identified for the 2016 flights.

<b>Flight Date</b>	<b>Field Name</b>	<b>GPS Points Available</b>	<b>Quadrats Identified</b>
<b>6/21/2016</b>	Sandy Field	10	10
<b>6/21/2016</b>	Tifton Field	0	0*
<b>07/29/2016</b>	Sandy Field	10	0**
<b>07/29/2016</b>	Tifton Field	10	08
<b>09/01/2016</b>	Sandy Field	10	05
<b>09/01/2016</b>	Tifton Field	10	0**
<b>10/21/2016</b>	Sandy Field	10	9***
<b>10/21/2016</b>	Tifton Field	10	10

Table 5. Summary of quadrat identification for 2016 flights.

\*Quadrats were visible but numbers could not be assigned because GPS data was not available/field map did not align with what was visible in the imagery.

\*\*Quadrats were not visible.

\*\*\*GPS location for Quadrat 1 was not located over reflectance image.

To address the issue of locating and identifying quadrats in the flight reflectance images, RTK GPS points of each quadrat corner were collected during the 2017 field season. A lower flying height was used for the 2017 flights to facilitate confirming quadrat locations and identifying uncontaminated pixels (Table 2). This produced consistent results for each flight, with no missing data from quadrats not visible in the orthomosaic. The 2017 quadrats were then

easily digitized using the RTK GPS control points as quadrat corners rather than as points of reference for a visual search.

Two quadrat sizes were used for the 2017 flights. Quadrats were placed side-by-side in the field. Quadrats were heads-up digitized for the month of May, as this month only had a single GPS location for each quadrat available. For the July, August, and September 2017 flights, RTK GPS locations of the quadrats were provided. The polyline features derived from the RTK GPS quadrat corner locations were converted to polygons to represent the quadrat areas. Interior polygons were then created for all quadrats in each flight that excluded pixels contaminated by the quadrat piping, following the same visual inspection procedure used for the 2016 flights to exclude contaminated pixels.

<b>Field Name</b>	<b>Month</b>	<b>GPS Points Available</b>	<b>Quadrats Identified (0.5 m<sup>2</sup>)</b>	<b>Quadrats Identified (1.0 m<sup>2</sup>)</b>
<b>Sandy Field</b>	May	10	10	10*
<b>Tifton Field</b>	May	10	10	10
<b>Sandy Field</b>	July	0**	10	10
<b>Tifton Field</b>	July	0**	10	10
<b>Sandy Field</b>	August	0**	10	10
<b>Tifton Field</b>	August	0**	10	10
<b>Sandy Field</b>	September	0**	10	10
<b>Tifton Field</b>	September	0**	10	10

Table 6. Summary of quadrat identification for 2017 flights.

\*GPS points give general location of quadrats. Quadrats visible in imagery. Only two sizes of quadrats were used.

\*\*GPS points were not provided. Quadrat locations were given directly as polyline features.

### 3.5 Vegetation Indices

As discussed in Chapter 1, vegetation indices, or VIs, are a subset of spectral indices developed to measure various biophysical properties of plants, such as biomass, chlorophyll content, and nitrogen content [9], [85], [86]. Different VIs are suitable for measuring different

plant properties. NDVI, also discussed in Chapter 1, is generally a good indicator of plant biomass, as is NGRDI (Normalized Green-Red Difference Index) [86], [87]. Green NDVI, or GNDVI, has also been shown to correlate well with plant biomass and with nitrogen content and is more sensitive to different concentrations of chlorophyll than NDVI [88], [89]. Enhanced NDVI was developed to improve the performance of the NDVI index for digital cameras, which respond differently to reflected light than the color infrared film first used with NDVI [90]. These four VIs—NDVI, GNDVI, NGRDI, and ENDVI—were selected for testing correlations of UAS-derived VIs with field measurements of plant biomass and crude protein content [91].

Table 7 shows the equations that define each of these VIs.

<b>Vegetation Index</b>	<b>Equation</b>	<b>Description</b>
<b>NDVI</b>	$\frac{(NIR - Red)}{(NIR + Red)}$	Normalized Difference Vegetation Index. Provides a measure of biomass/chlorophyll content [86], [92].
<b>GNDVI</b>	$\frac{(NIR - Green)}{(NIR + Green)}$	Normalized Difference Vegetation Index using the green band instead of the red. Also provides a measure of biomass/chlorophyll content, but can be more effective at later stages of growth [89], [93].
<b>NGRDI</b>	$\frac{(Green - Red)}{(Green + Red)}$	Normalized Green-Red Difference Index [86]
<b>ENDVI</b>	$\frac{(NIR + Green) - (2 * Red)}{(NIR + Green) + (2 * Red)}$	Enhanced NDVI Index [86], [90]

Table 7. Vegetation indices used and their associated equations.

For the 2016 flights, the VI rasters were created after verifying the reflectance image band identities. Each orthomosaic band was inspected over healthy vegetation to help verify the band identities. Figure 29a shows the three-band orthomosaic produced from one of the 2016 flights. Figure 29b shows the NIR band alone, over healthy vegetation. Healthy vegetation appears bright in the NIR band. Once the bands were identified, each VI was computed,

generating a new raster image. For the 2017 flights, the bands were already separated and identified after being radiometrically corrected in Pix4D, so band verification was not necessary. Additionally, the 2017 flights included the red-edge band (Table 1). The VIs were calculated using both the NIR and red-edge bands, except for NGRDI, which does not include the infrared band.

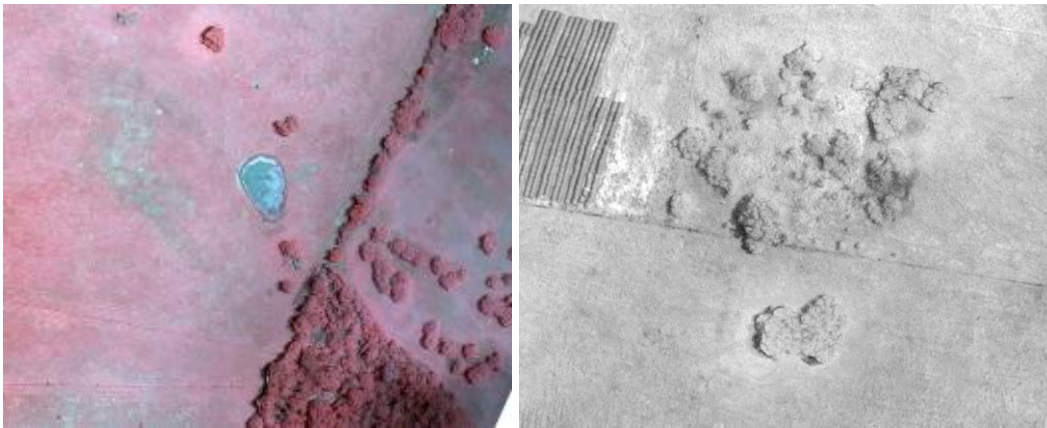


Figure 29. (a) An example of the false-color image created by combining the red, green, and NIR bands (left). (b) Green vegetation appears brighter in the NIR band (right).

The interior traced polygons created in the quadrat identification procedure defined the areas of the VI rasters that would be processed and compared to the field-collected data. Statistics were calculated for the interior of each quadrat for each VI raster, including the minimum, maximum, mean, and standard deviation of the VI raster cells values within each quadrat. The mean values from the VI raster cells, considered to be best representative of the quadrat area's spectral response, were used with the field measurements for statistical analysis. Correlation was calculated in order to see if the VIs and field measurements are linearly related, and to what degree. Linear regression was calculated to assess whether the VIs could be used to estimate or predict field measurements with any certainty. The results are discussed in the following chapter.

## CHAPTER 4: RESULTS AND DISCUSSION

### 4.1 Results

#### 4.1.1 UAS-SfM Point Cloud Classification

In order to evaluate the success of the UAS-SfM point cloud classification algorithm and input parameters such as tile size, step size, spike size, and bulge, five 3 m<sup>2</sup> test areas were created for each field. These test areas capture representative ground and non-ground surfaces such as trees, buildings, and forage in fields. Statistics were generated for each flight using both the raw and classified point clouds for these representative test areas. Table 8 contains descriptions of the test areas for both the Sandy and Tifton fields. Figure 30 shows images of the Sandy Field test areas; Figure 31 shows images of the Tifton Field test areas.

<b>Sandy Field Test Areas</b>	<b>Tifton Field Test Areas</b>
1. Field	1. Building Roof
2. Tree Stand	2. Tree Stand
3. Pond	3. Lone Tree
4. Lone Tree	4. Planted Field
5. Building Roof	5. Adjacent Field

Table 8. Summary of point cloud evaluation test areas for each field.

The total number of points classified as ground points were compared to the original number of points in the point cloud within the test area. See Table 2 to review the specifications of the eBee UAS and sensor. Only the 2016 flights were evaluated; based on results of the 2016 evaluation discussed in this and the section 4.1.2, the 2017 UAS-SfM point clouds were not evaluated.



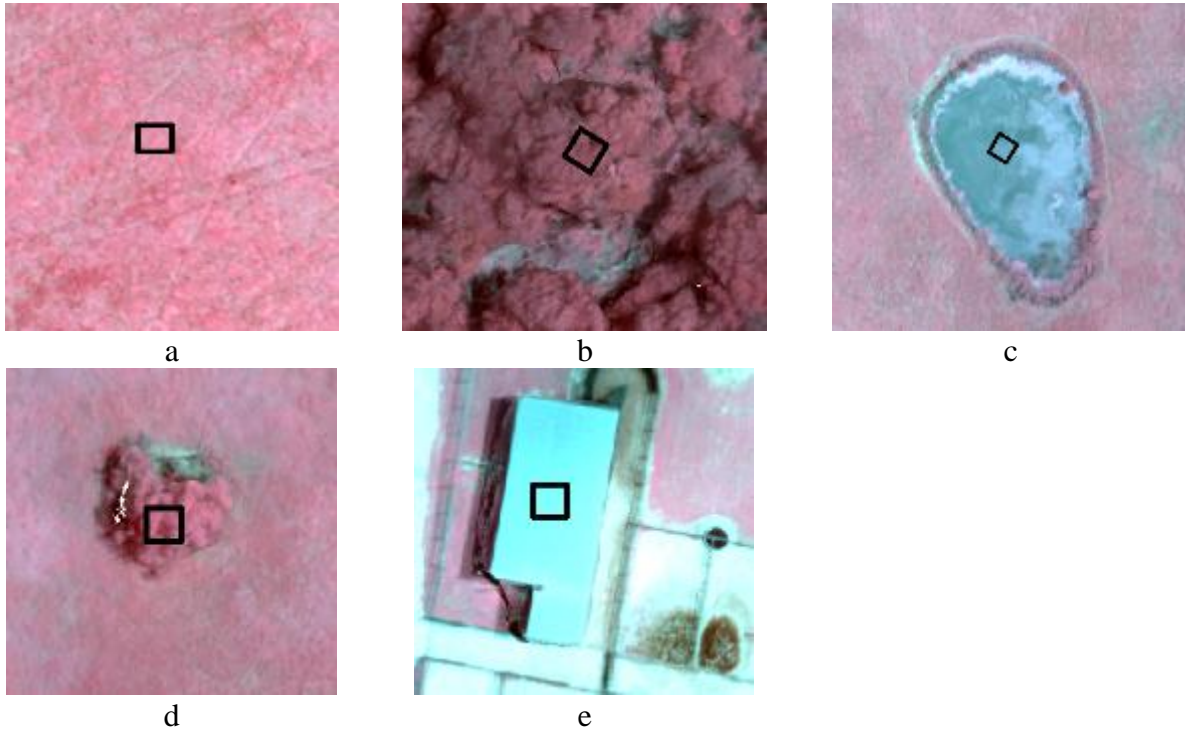


Figure 30. The Sandy Field test areas: (a) Field; (b) Tree Stand; (c) Pond; (d) Lone Tree; (e) Building Roof.

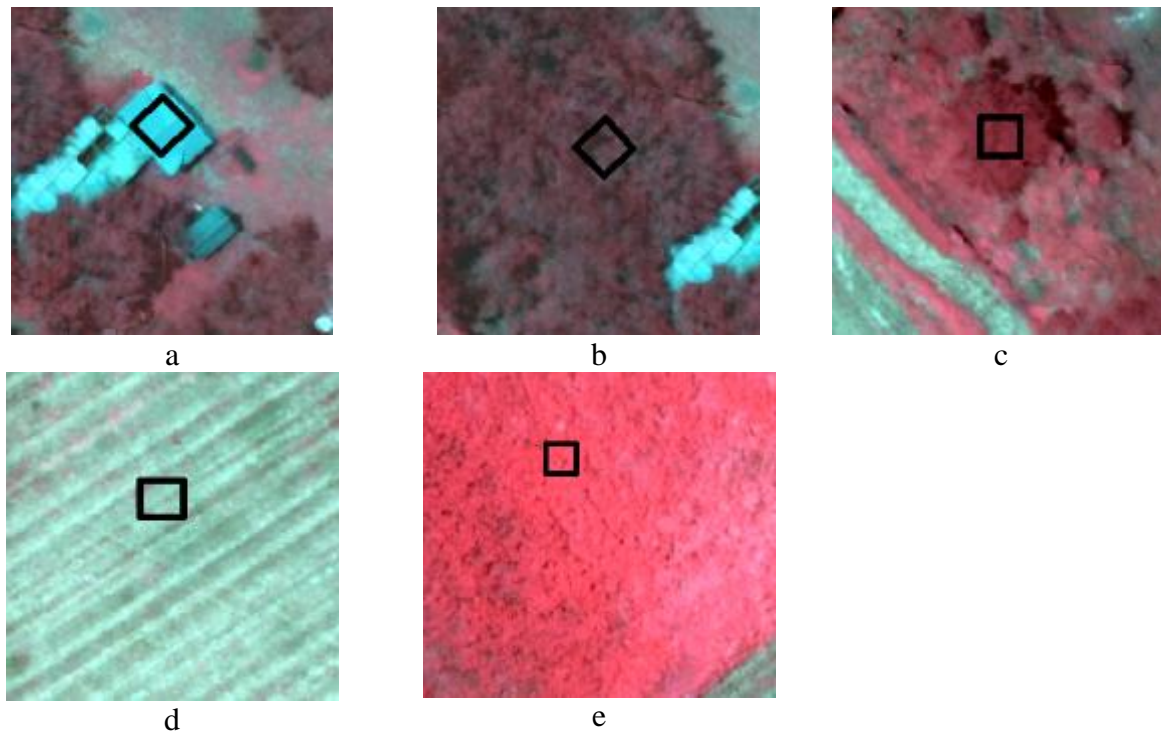


Figure 31. The Tifton Field test areas: (a) Building Roof; (b) Tree Stand; (c) Lone Tree; (d) Planted Field; (e) Adjacent Field

The ratio of ground to non-ground points was used to evaluate the point cloud classification in the test areas where the correct point classification is known a priori. The results are shown for the Sandy field (Figure 32) and for the Tifton field (Figure 33). In general, the non-ground test areas—tree stand, pond, lone tree, and building roof—successfully excluded non-ground points, with some significant misclassifications for the September 2016 flight of the Lone Tree test area in both the Sandy and Tifton fields. The Adjacent Field test area was available in the Tifton data and was used for general comparison against the Planted Field results. The fields were difficult to evaluate without ground truth data. Generally, the fields would include both ground and non-ground points; the forage plants, however, should ideally not be classified as ground as they are of primary interest for analysis. For this reason they were included as part of the point cloud classification evaluation.

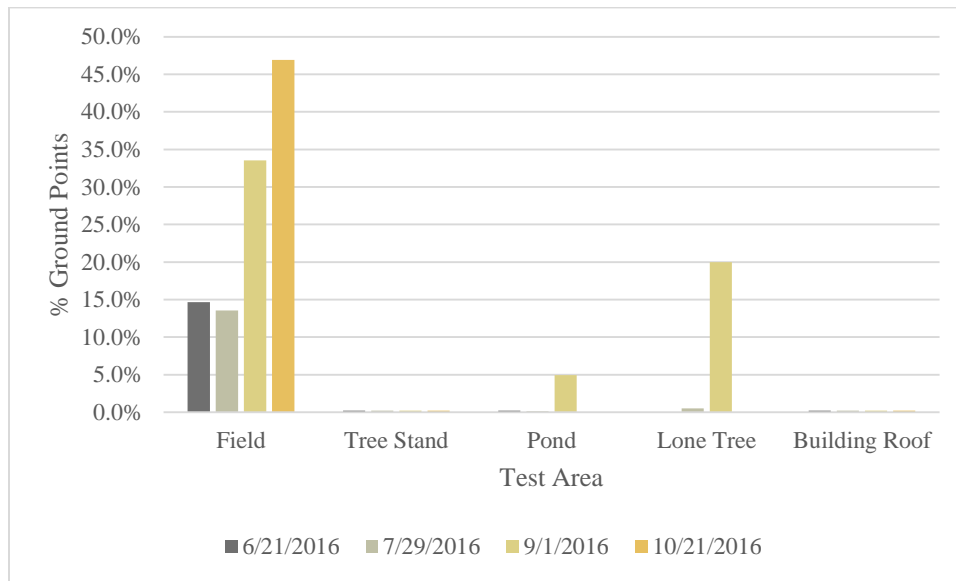


Figure 32: Percent ground points for the 2016 Sandy Field flights in the test areas.

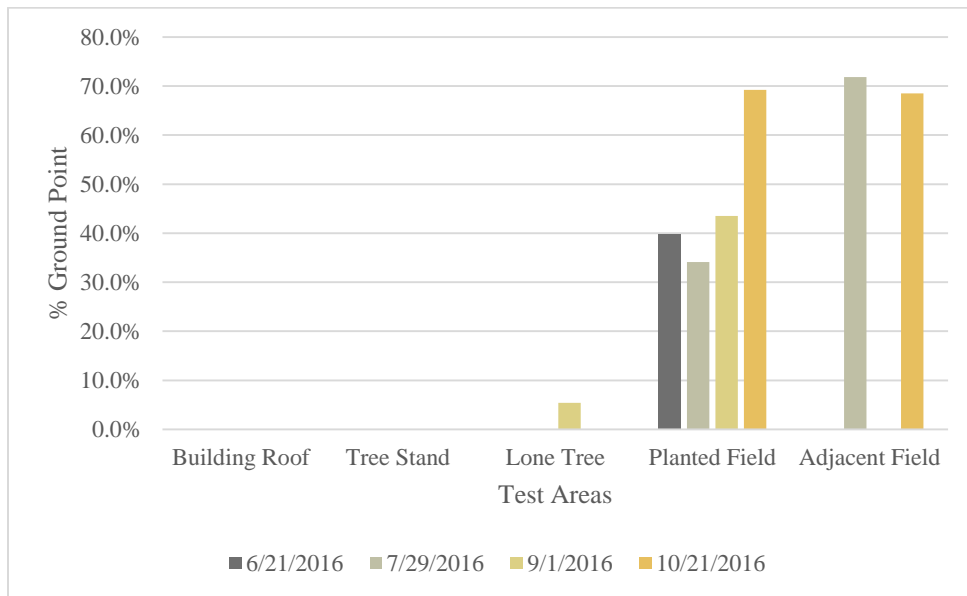


Figure 33: Percent ground points for the 2016 Tifton Field flights in the test areas.

The Field test area was of particular interest for the study as it was used for analyzing the point cloud structure and the vegetation indices. In both the Sandy and Tifton fields, there is a significant increase in the number of Field ground points as the growing season progresses. While both the Sandy and Tifton fields show a greater concentration of ground points in the Field test areas, there is a significantly larger proportion of ground points in the Tifton field, especially during the October flight. This may be due to the fact that the Tifton field was flown at almost half the altitude of the Sandy field, due to its smaller size. Figure 34 and Figure 35 summarize the point counts and point densities per test area for the Sandy and Tifton fields, respectively.

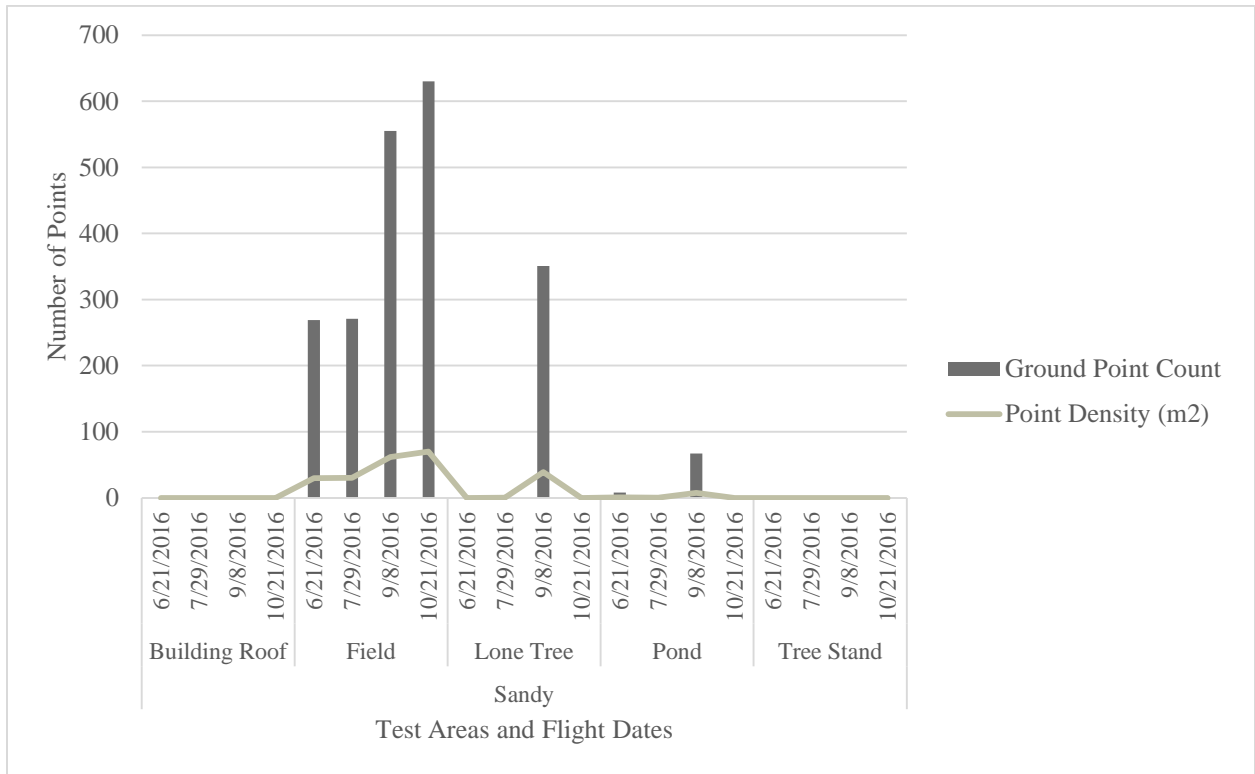


Figure 34. Point counts and densities per test area for the 2016 Sandy Field flights.

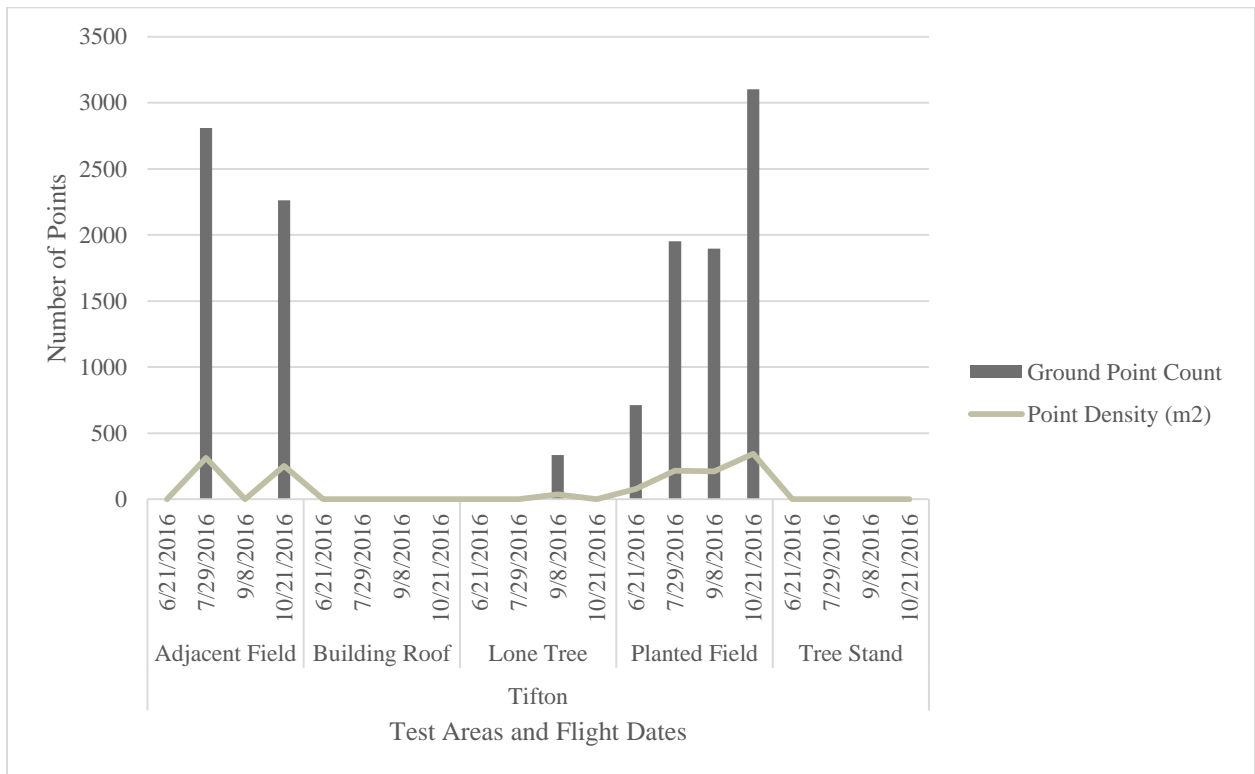


Figure 35. Point counts and densities per test area for the 2016 Tifton Field flights.

Based on the number and proportion of ground points in each test area, the iterative ground point classification algorithm consistently classified larger features such as trees and buildings as non-ground. This was true even in areas where trees completely filled the step size, as with the Tree Stand test areas. For test areas where ground points are present in the test area, additional ground-truth information would be required to determine whether the classification was successful. This is particularly true for the Field test areas, as they are of principle interest for the study. The iterative classification algorithm did not completely identify the field test areas as ground; this is ideal as there must be a distinction between the forage in the pastures and the ground beneath them in order to use the point cloud to derive accurate DEM and DSM surfaces that can be used to estimate HM and plant heights. Additional ground-truth information regarding the location and proportion of forage in each test area would help determine if the algorithm successfully captured only forage as non-ground points in the field test areas.

#### *4.1.2 Canopy Height Models*

UAS-SfM point clouds cannot capture ground surface that is not visible to the sensor. As a result, the classified point cloud is still a mixture of ground and vegetation even when the classification algorithm is successful at only capturing the lowest points within a moving window. This creates significant issues with generating a valid DEM. When the ground surface is inconsistently visible or obscured in the imagery, the classified point cloud can represent a false topography that combines the actual ground surface with low vegetation.

This was demonstrated by creating a difference raster or canopy height model (CHM) [94] from the DEM and DSM generated from the UAS-SfM point cloud (as described in Chapter 3). The CHM was created by subtracting the DEM from the DSM [95]. The result is a different surface that, assuming the DEM surface accurately represents the underlying

bare-earth ground surface, models the height of vegetation [94]. The cell values of a CHM represent the elevation of the DSM above or below the DEM. Where the difference raster has a value of zero (0), the DSM and DEM have the same elevation. An example of a CHM created from the UAS-SfM-derived DEM and DSM (Figure 23 and Figure 24) from October 2016 is shown in Figure 36. Figure 36 shows large portions of the CHM where its cell values are zero, indicating that the canopy height is also zero and thus these areas should represent the bare-earth surface. The areas of greatest canopy height appear along the edges of the field, particularly where there are trees.



Figure 36. The difference surface created from the October 2016 UAS-SfM-derived DEM and DSM.

In order to better evaluate the ability of the UAS-SfM-derived CHM to correctly estimate plant height, the average value for the CHM within each quadrat was compared to the average plant height measured for each quadrat in the field (Figure 37). The plant heights from the

canopy height model underestimate the measured heights from the quadrats. This is due to the fact that the UAS-SfM-derived DEM surface is essentially hovering above the actual ground surface. As the DEM had an overall higher elevation, when subtracted from the DSM it produced smaller height values when compared to the measured plant heights.

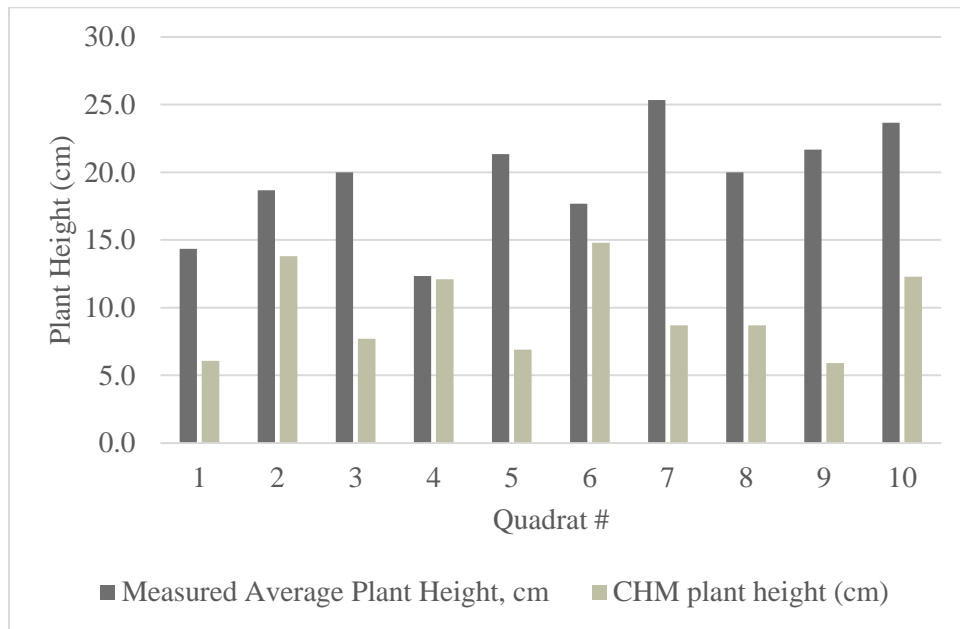


Figure 37. The measured plant heights vs difference raster heights for the interior quadrat areas (October 2016 flight).

#### 4.1.3 Vegetation Indices vs Field Measurements

As explained in Chapter 3, four VIs were calculated from the radiometrically-corrected UAS-SfM orthomosaic. Table 7 contains the equations used to calculate these VIs. The mean VI raster value was extracted from each quadrat, and linear regression analysis was performed using these mean VI values and each field measurements. No non-linear trends in the data were observed. A true month-to-month comparison of the fields is not possible with the 2016 data, as the quadrats were not consistently captured. The June 2016 flights, for instance, only resulted in data for the Sandy field as GPS data were not collected for the Tifton quadrats and the quadrat piping was not visible in the imagery. The 2016 flights resulted in at least one field from each

flight date providing data for analysis. The 2017 data consistently captured the quadrats, largely due to the fact that the quadrats were located using RTK GPS in the field, allowing for comparison between fields for each flight. Table 5 and Table 6 summarize the number of quadrats identified for the two field seasons.

Figure 38 shows the relative areas available for analysis from the 2016 and 2017 flights, based on both the number of quadrats available for analysis and the uncontaminated area within each quadrat. The difference in uncontaminated quadrat area available for analysis was a key consideration when interpreting and comparing the results from the 2016 and 2017 flights. A monthly comparison is included in Appendix 1 that shows the areas available for analysis from each flight alongside the  $r^2$  values.

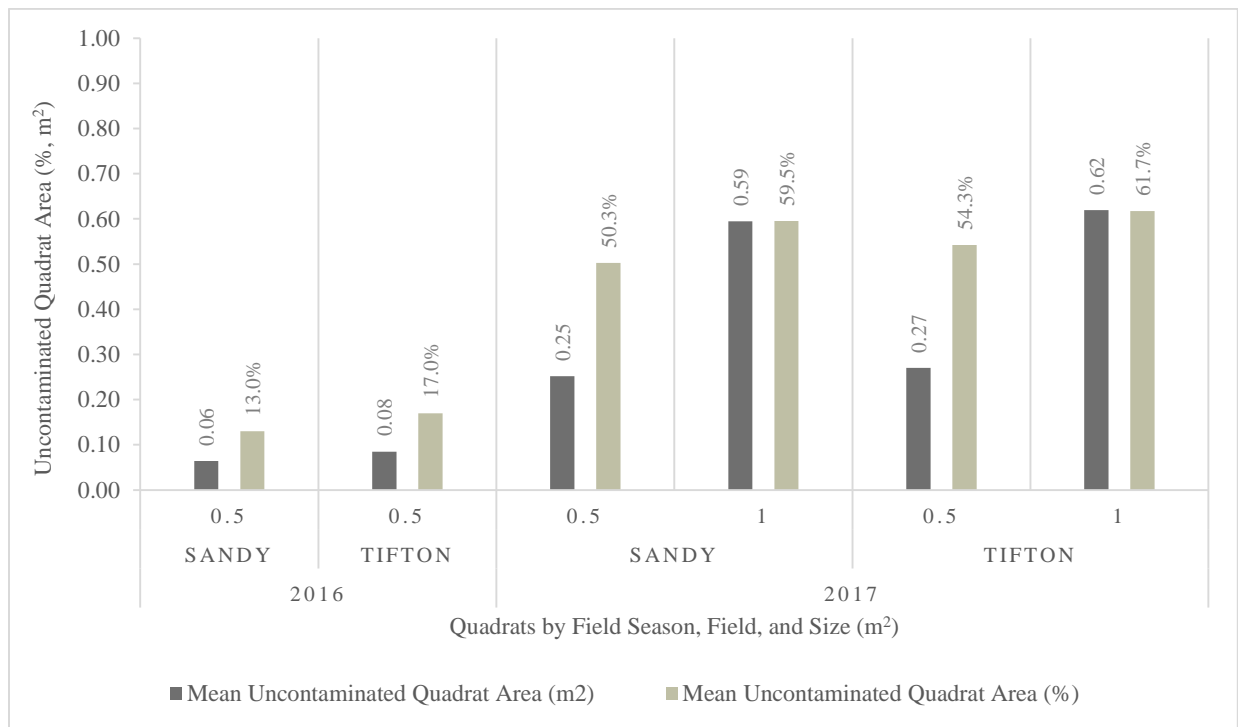


Figure 38. Uncontaminated areas (m<sup>2</sup> and %) for the 2016 and 2017 quadrats.



## *2016 Results*

Of the four field measures and VIs examined in the 2016 flights, the strongest correlation occurred in the Sandy field flights for the crude protein field measure (Figure 39). This field measure had relatively strong positive correlations with all the VIs. The VIs overall had inconsistent correlations between the Sandy and Tifton fields in the 2016 flights. The Sandy field shows a relatively strong correlation between all four VIs with the crude protein field measurements, but weak positive and even negative correlations with average plant height and HM. Dry matter (%) had weak positive correlation in the 2016 Sandy field data, but a weak negative association in the Tifton field data. The crude protein field measure had mostly negative correlations in the Tifton field flights. There was very little consistency of correlation between the two fields for the 2016 flights. Except for the Sandy field crude protein results, the field measures had weak correlations with the VIs in the 2016 data. It is interesting to note that the HM field measures consistently had a weak negative association with most of the vegetation indices in the 2016 flights, but a stronger positive correlation for the NGRDI VI that was present in data from both fields. In general, however, the correlation between field measures and vegetation indices in 2016 is inconsistent.

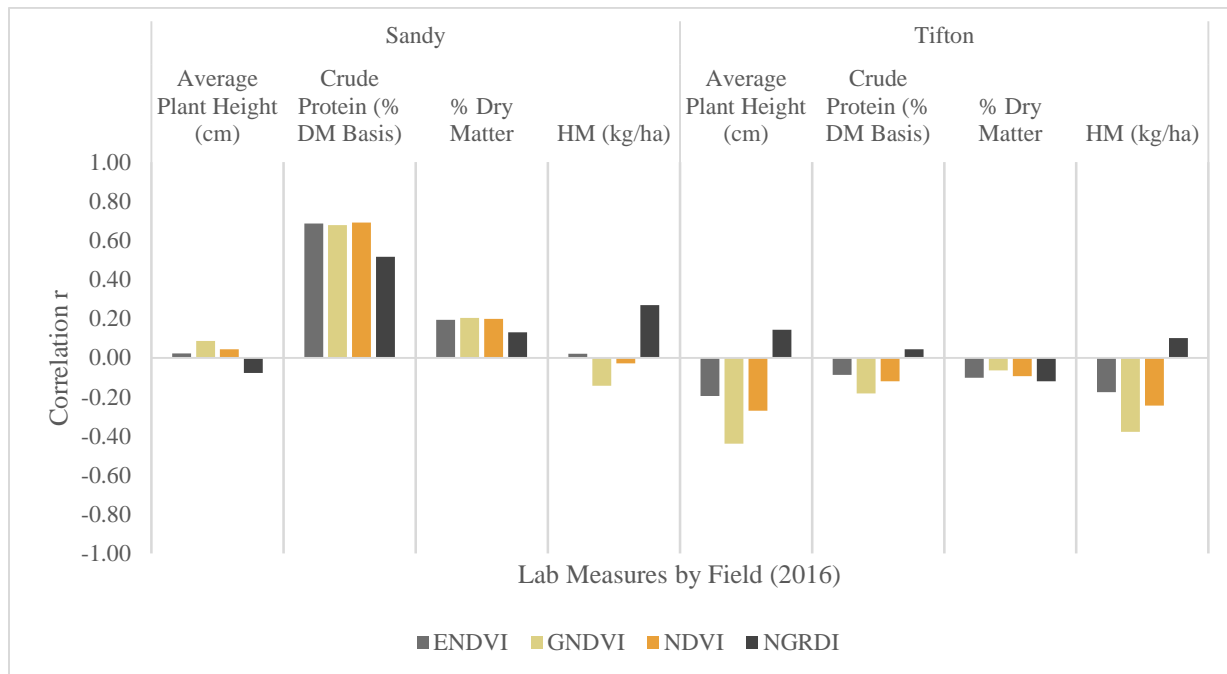


Figure 39. Correlation between field measures and vegetation indices by field for the 2016 flights.

Regression analysis was done for all of the 2016 flights by combining each of the flights and separating the results by field measure and VI. In this regression analysis done for the year as a whole there are no significant regressions between any of the VIs and the field measures. Moreover, the low  $r^2$  values indicate that very little variability in each VI accounts for the variability observed in the field measurements. Table 9 has the  $r^2$  values for each VI and field measure, with the VIs ranked in order of their mean  $r^2$  value. Note that P-values for the regression models (Table 9) are not significant when taking the average of both the Sandy and Tifton fields. See Figure 41 for results individualized by field.

<b>Vegetation Index &amp; Field Measure</b>	<b><math>r^2</math></b>	<b>P</b>
<b>NGRDI</b>	<b>0.21</b>	<b>0.53</b>
<b>%DM</b>	0.17	0.59
<b>Average Plant Height (cm)</b>	0.34	0.64
<b>CP (%DM Basis)</b>	0.19	0.44
<b>HM kg/ha</b>	0.14	0.45
<b>ENDVI</b>	<b>0.21</b>	<b>0.57</b>

<b>%DM</b>	0.26	0.52
<b>Average Plant Height (cm)</b>	0.29	0.68
<b>CP (%DM Basis)</b>	0.19	0.37
<b>HM kg/ha</b>	0.09	0.70
<b>NDVI</b>	<b>0.20</b>	<b>0.51</b>
<b>%DM</b>	0.28	0.53
<b>Average Plant Height (cm)</b>	0.25	0.56
<b>CP (%DM Basis)</b>	0.16	0.32
<b>HM kg/ha</b>	0.09	0.61
<b>GNDVI</b>	<b>0.17</b>	<b>0.37</b>
<b>%DM</b>	0.21	0.57
<b>Average Plant Height (cm)</b>	0.16	0.38
<b>CP (%DM Basis)</b>	0.11	0.24
<b>HM kg/ha</b>	0.19	0.32

Table 9. Performance of VIs overall for the 2016 flights for both the Sandy and Tifton fields. The p-values indicate the significance of the regression models between each of the VIs and the field measurements.

Certain months had much better individual performance, however; these values can be seen in the monthly analysis in Appendix 1. Figure 40 shows the results of the yearly analysis by field, VI, and field measure. In the regression analyses for the Tifton field, average plant height accounted for the most variation when analyzed with any VI. However, this variation was still below 50%, and all regressions were nonsignificant. The regression model for the crude protein field measure in the Sandy Field (Figure 41) was the most significant ( $P < 0.05$ ), and performed comparably well with all vegetation indices. The variation accounted for with this field measure was still relatively low ( $< 30\%$ ).

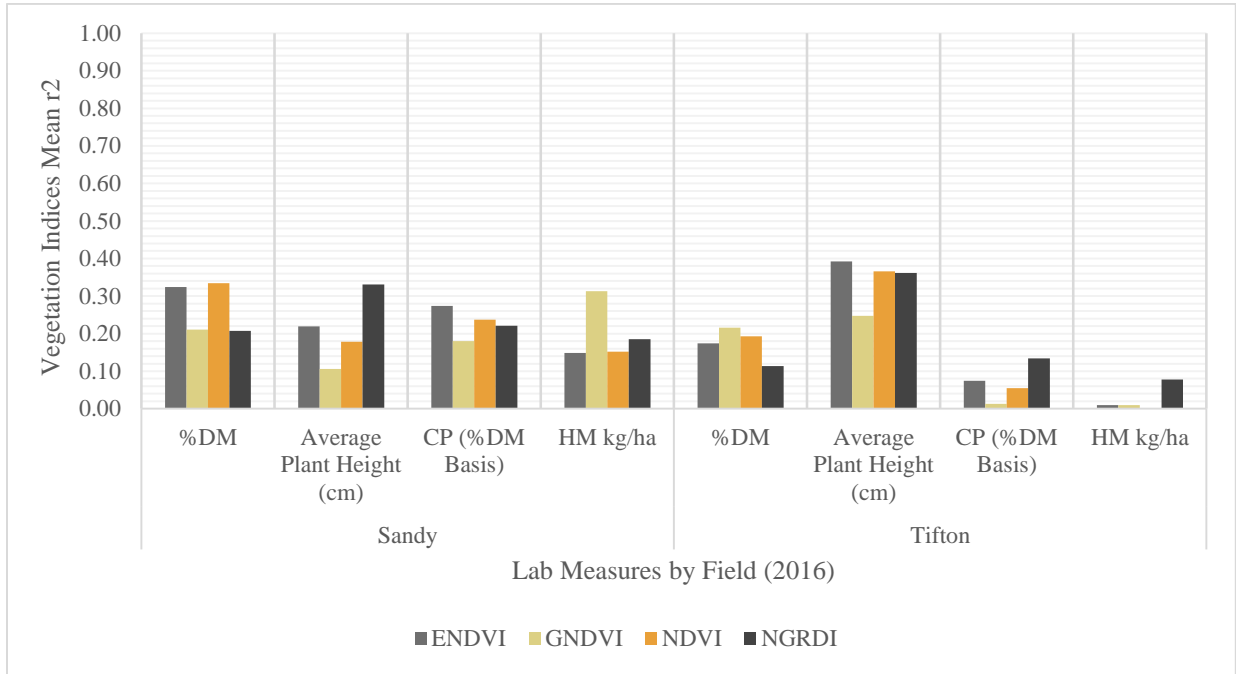


Figure 40. Performance of each of the vegetation indices for each field measurement by field for the 2016 flights.

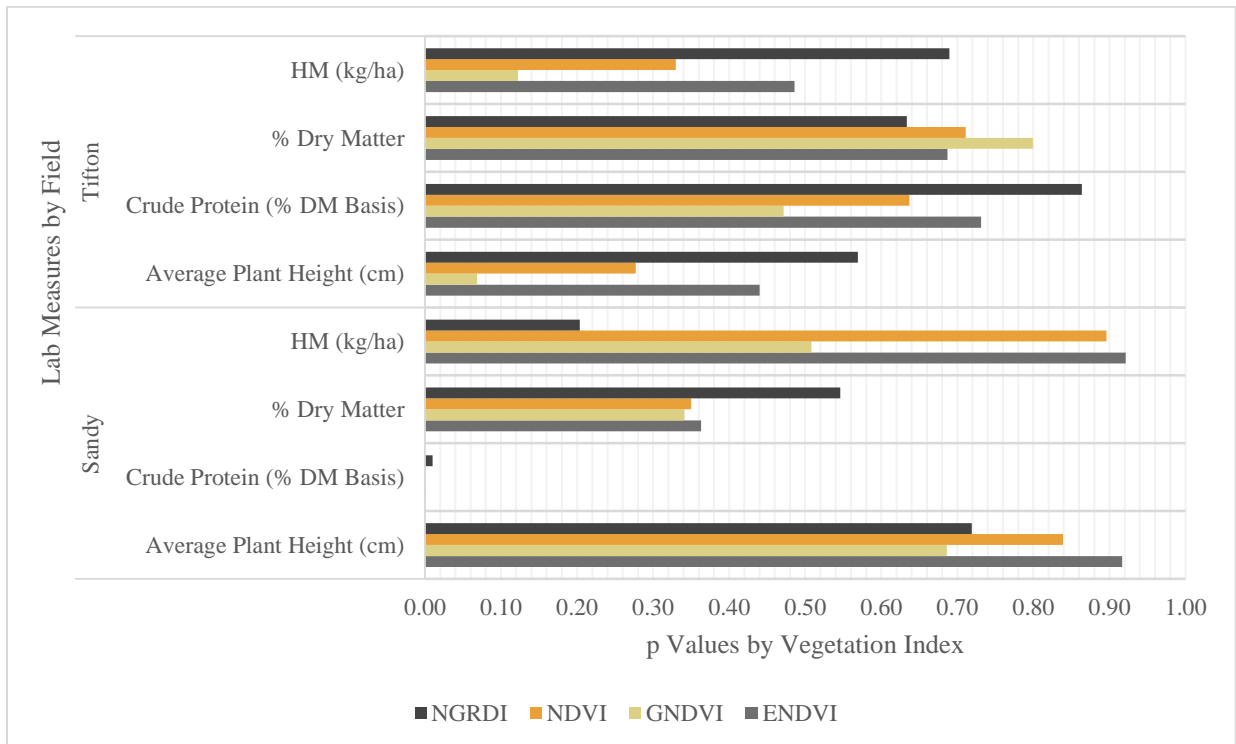


Figure 41. P-values resulting from the linear regression analysis for the 2016 flights.

Monthly results from each flight are shown in Appendix I. Each figure shows the results of the regression analyses for a single field measure and all the VIs, by month and field. The figures for the 2016 flights— Figure 47, Figure 49, Figure 51, and Figure 53— generally show the highest associations between VIs and field measurements for the June 2016 Sandy field flights. This can be seen with HM (Figure 47, Appendix I), average plant height (Figure 49, Appendix I), and % Crude Protein (CP) (Figure 53, Appendix I). This was true except for the % Dry Matter (DM) field measurement (Figure 51), which had very strong associations in the September 2016 Sandy field flight. There were no identifiable quadrats for the Tifton field for that same month for comparison. In general, the Tifton flights in 2016 had the strongest associations during the month of July. There were no identifiable quadrats for the Sandy field for July for comparison in 2016. Interestingly, the Tifton flights in 2016 had almost no association between any of the VIs and HM (Figure 47), and extremely weak associations with % CP (Figure 53), but the Sandy field flights in 2016 show a very different pattern with  $r^2$  values around 0.5 for these field measurements and several VIs.

### *2017 Results*

The 2017 results showed significantly stronger correlations. Figure 42 shows these correlation values. The correlations were strongest for HM. The HM correlations were consistently positive for all vegetation indices between both the Sandy and Tifton fields. The NDVI vegetation index provided the most consistent positive association with HM between the two fields. Crude protein had relatively strong correlations with all vegetation indices as well, but only in the Sandy field; the Tifton field again showed the opposite trend. DM and average plant height have weak negative correlations in 2017, nearly opposite to the year before, but are more consistent between the two fields in this season.

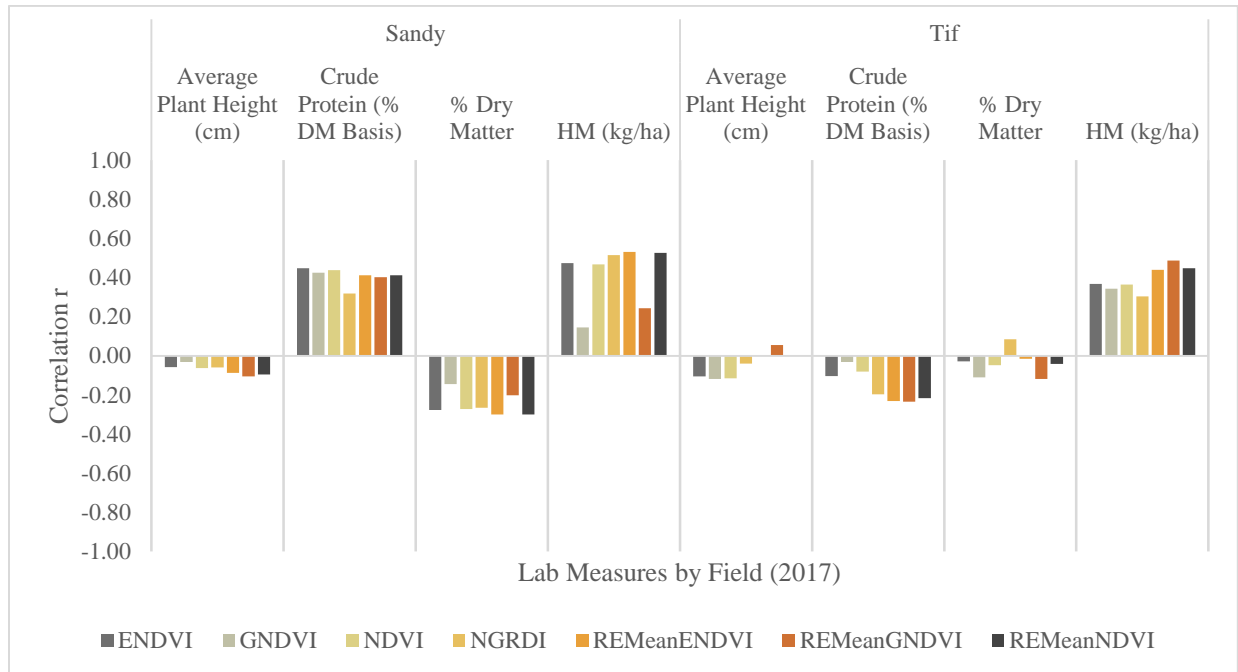


Figure 42. Correlation between field measures and vegetation indices by field for the 2017 flights. The VIs using the red-edge band are indicated using a “RE” prefix.

Linear regression analysis was done for all the 2017 flights combined. The results were separated by field measure and VI. The 2017 regression models had lower average  $r^2$  values, but within each VI, these  $r^2$  values were fairly consistent (Table 10). For all regressions, these low  $r^2$  values indicate considerable scatter of data points around the regression line, and further indicate that very little variation in the field measurements are explained by regression the VIs. However, there are significant linear relationships between the VIs and field measurements that indicate some of the VIs can potentially be used to predict the field measurements, but with low accuracy.

Only GNDVI and its red-edge version had significantly weaker associations than the other VIs (Table 10). Table 10 has the  $r^2$  values for each VI and field measure, with the VIs ranked in order of their mean  $r^2$  value. Note that the p-values for the regression models taking the average of both fields and quadrat sizes for all 2017 flights (Table 10) are much more significant than in 2016.

<b>Vegetation Index &amp; Field Measure</b>	<b>r<sup>2</sup></b>	<b>P</b>
<b>ENDVI (Red Edge)</b>	<b>0.16</b>	<b>0.71</b>
%DM	0.11	0.45
Average Plant Height (cm)	0.09	0.71
CP (%DM Basis)	0.20	0.02
HM kg/ha	0.25	<i>P &lt; .0001</i>
<b>ENDVI</b>	<b>0.16</b>	<b>0.27</b>
%DM	0.11	0.41
Average Plant Height (cm)	0.09	0.48
CP (%DM Basis)	0.19	0.18
HM kg/ha	0.25	<i>P &lt; .0001</i>
<b>NDVI (Red Edge)</b>	<b>0.16</b>	<b>0.27</b>
%DM	0.11	0.36
Average Plant Height (cm)	0.08	0.70
CP (%DM Basis)	0.19	0.03
HM kg/ha	0.25	<i>P &lt; .0001</i>
<b>NDVI</b>	<b>0.15</b>	<b>0.26</b>
%DM	0.11	0.34
Average Plant Height (cm)	0.08	0.44
CP (%DM Basis)	0.18	0.24
HM kg/ha	0.25	<i>P &lt; .0001</i>
<b>NGRDI</b>	<b>0.15</b>	<b>0.24</b>
%DM	0.12	0.24
Average Plant Height (cm)	0.12	0.67
CP (%DM Basis)	0.15	0.04
HM kg/ha	0.22	<i>P &lt; .0001</i>
<b>GNDVI</b>	<b>0.12</b>	<b>0.32</b>
%DM	0.12	0.27
Average Plant Height (cm)	0.06	0.54
CP (%DM Basis)	0.12	0.39
HM kg/ha	0.17	0.10
<b>GNDVI (Red Edge)</b>	<b>0.10</b>	<b>0.18</b>
%DM	0.09	0.18
Average Plant Height (cm)	0.05	0.49
CP (%DM Basis)	0.11	0.02
HM kg/ha	0.14	0.01

Table 10. Performance of VIs overall for the 2017 flights. The p-values indicate the significance of the regression models between each of the VIs and the field measurements.

The HM regression models only account for 25% of the total variation ( $P < 0.05$ ); Appendix 1, however, shows that some individual flights produced much higher  $r^2$  values. The  $r^2$  values and p-values for the regression analysis of the four field measures and VIs for 2017 are shown in Figure 43 and Figure 44, respectively.

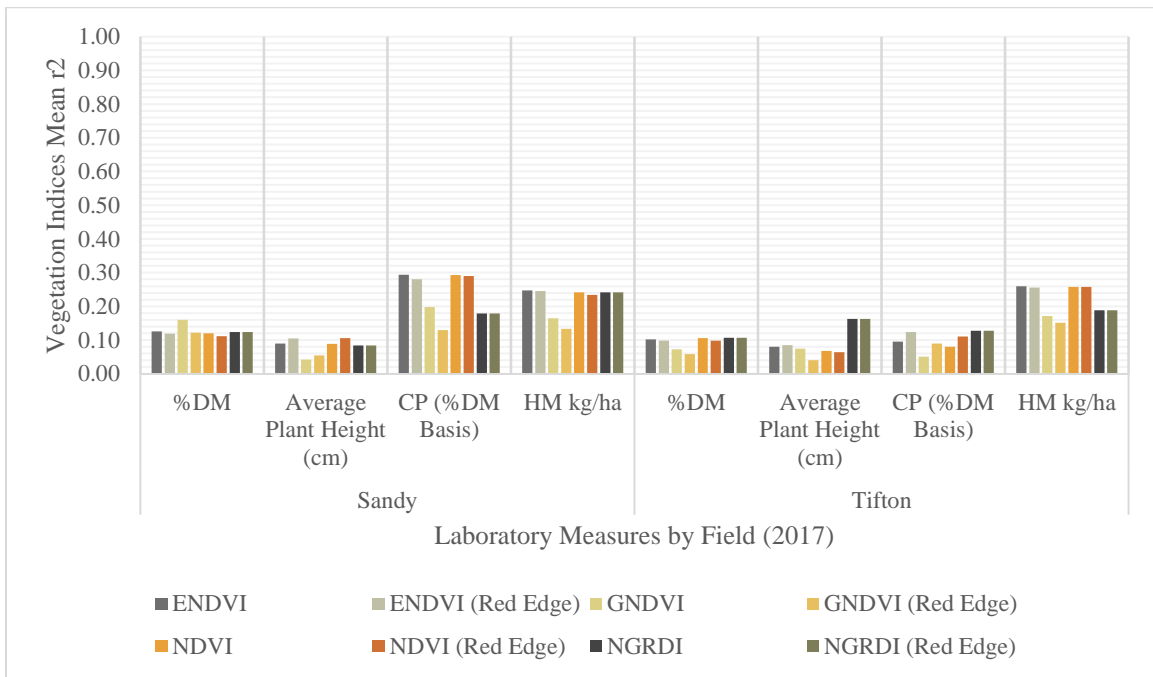


Figure 43. Performance of each of the vegetation indices for each field measurement by field for the 2017 flights. The VIs using the red-edge band are indicated using a “RE” prefix.



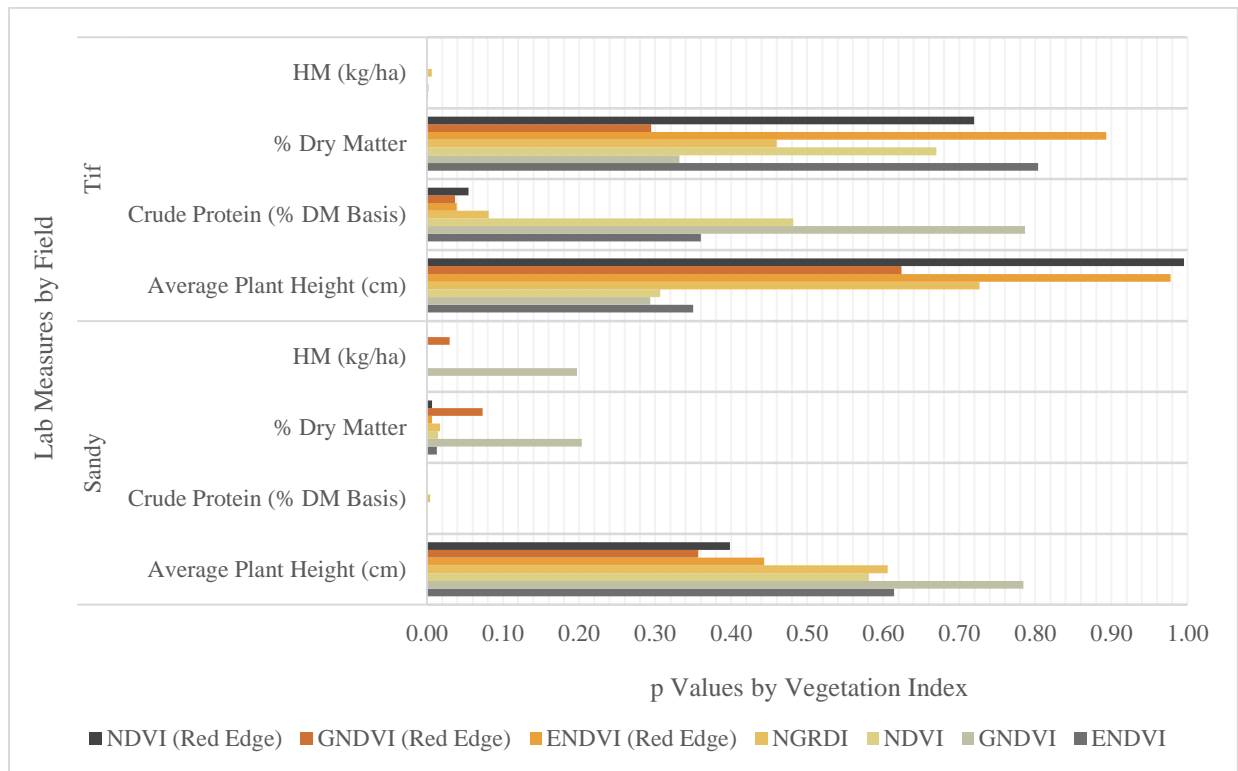


Figure 44. P-values resulting from the linear regression analysis for the 2017 flights.

The crude protein regression models for the Sandy field flights perform slightly better than HM in 2017. These models accounted for nearly 30% of the overall variation ( $P < 0.05$ ) when considering the regression models using the larger quadrat size. The July and August Sandy Field flights, shown in Appendix 1 (Figure 54), produced regression models that accounted for nearly 50% of the overall variation and performed well with several vegetation indices for the Sandy field flights in July and August.

Crude protein measurements and HM both had the strongest regressions with ENDVI and NDVI vegetation indices when looking at monthly results for 2017. Based on the regression results, there appears to be a slight advantage to using the red-edge-based VIs over the NIR-based VIs in this study for the NDVI and ENDVI indices.

The monthly figures in Appendix I for the 2017 flights—Figure 48, Figure 50, Figure 52, and Figure 54— show very different results from 2016. HM has significant associations for the

month of May in the Tifton field, but relatively weak associations for the month of September in both fields (Figure 48). This contradicts the 2016 result where September had a relatively stronger association for HM with both GNDVI and NGRDI in the September 2016 Sandy field flight, and almost no association at all for any month in the 2016 Tifton field flights. The 2017 flights showed weak associations for all months and both fields for average plant height (Figure 50). %DM likewise had weak associations throughout the year in both fields with all VIs (Figure 52). %CP, on the other hand, showed stronger associations around 0.5 in the 2017 July and August Sandy field flights (Figure 54).

### Combined Results

Filtering the results of the regression analysis for both years, both fields, and all quadrat sizes to consider only those results where  $P < 0.05$ , only results from the 2017 flights remain. Table 11 shows the  $r^2$  and regression equation p-values for all flights where  $P < 0.05$ . The NDVI and ENDVI indices calculated with a red-edge appear to have a slight advantage over the rest of the VIs, particularly with the crude protein and HM field measurements.

Vegetation Index & Field Measure	$r^2$	P
<b>ENDVI (Red Edge)</b>		
CP (%DM Basis)	0.2	0.02
HM kg/ha	0.25	$P < .0001$
<b>ENDVI</b>		
HM kg/ha	0.25	$P < .0001$
<b>NDVI (Red Edge)</b>		
CP (%DM Basis)	0.19	0.03
HM kg/ha	0.25	$P < .0001$
<b>NDVI</b>		
HM kg/ha	0.25	$P < .0001$
<b>NGRDI</b>		
CP (%DM Basis)	0.15	0.04

HM kg/ha	0.22	$P < .0001$
<b>GNDVI (Red Edge)</b>		
CP (%DM Basis)	0.11	0.02
HM kg/ha	0.14	0.01

Table 11. Results filtered to display only those results whose p values are  $< 0.05$ . Only the 2017 flights generated results where  $P < 0.05$ .

Figure 45 shows the regression plot ( $P < .0001$ ) for HM and red-edge NDVI for the 2017 Sandy Field flights for the 1 m quadrat size. Figure 46 shows the regression plot ( $P < .0001$ ) for crude protein and ENDVI for the 2017 Sandy Field flights for the 1 m quadrat size. For both plots, the scatter of data points around the least squares regression line are reflected in the low  $r^2$  values.

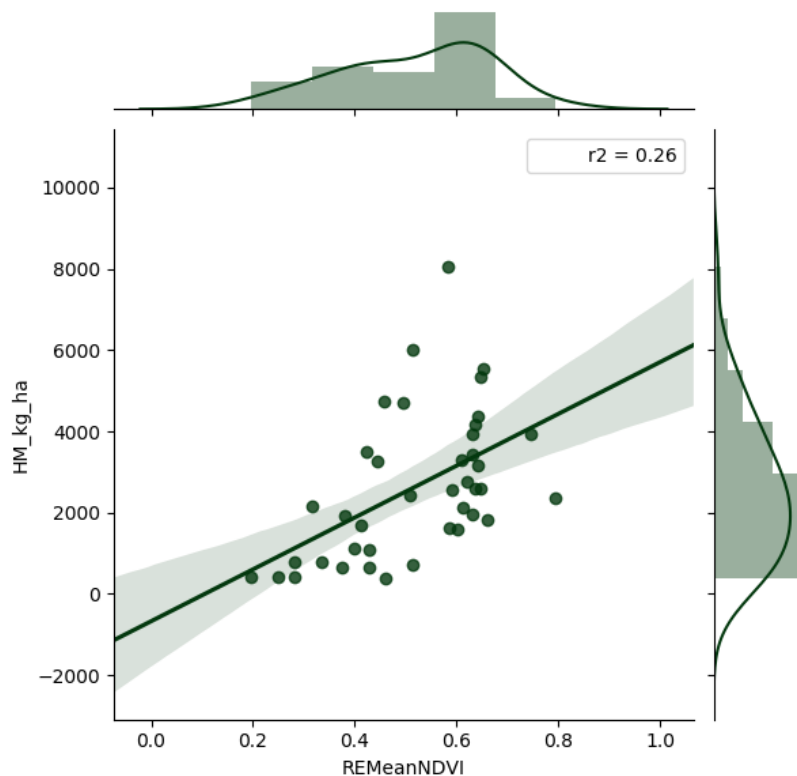


Figure 45. Regression plot and marginal histogram of NDVI using the red-edge band and HM for the 2017 Sandy Field flights using the 1m quadrat size.

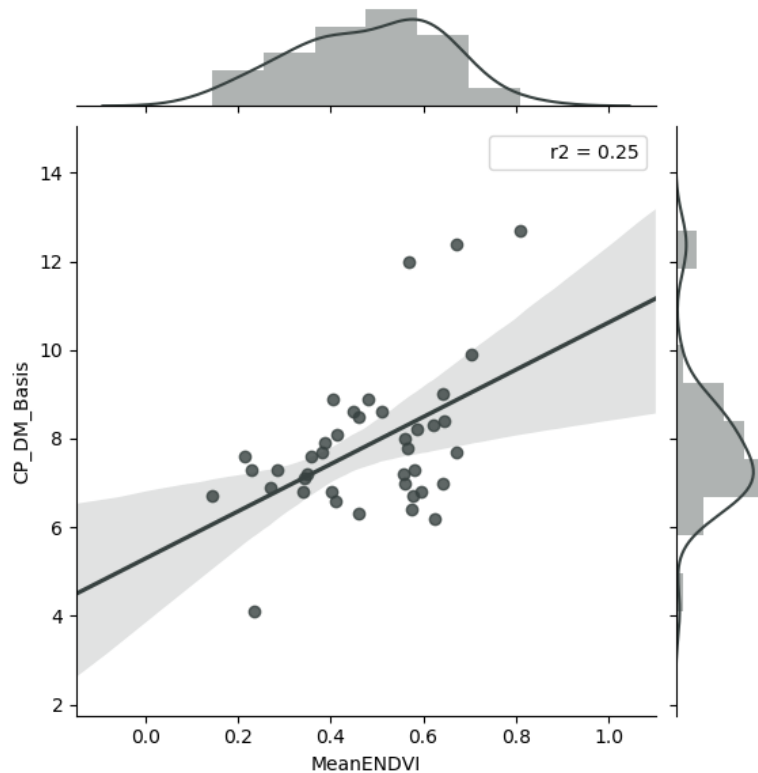


Figure 46. Regression plot and marginal histogram of ENDVI and crude protein for the 2017 Sandy Field flights using the 1m quadrat size.

## 4.2 Discussion

### 4.2.1 UAS-SfM DEM Products for Grazing land Management

The UAS-SfM-derived DEMs created for this study were of limited utility for generating an accurate CHM due to the fact that the ground surface could not consistently be captured by the sensor. Capturing the ground surface using a UAS will pose a challenge depending on the time of year and the unique topography being captured. For instance, the Brush field DEM (Figure 25), produced a smoother-appearing surface than the Tifton field DEM (Figure 23). This is largely due to the fact that the Brush field has less dense vegetation and more areas where the ground surface was visible to the sensor. The variation in these two fields suggests that UAS-SfM-derived DEMs will necessarily be inconsistent in their ability to capture the ground surface, and of limited utility for generating CHMs.

As the UAS-SfM DSM captures a great deal of detail and contains the primary data of interest—that is, it captures the vegetation canopy—it would be possible to use a UAS-SfM DSM in conjunction with a DEM acquired using a LiDAR sensor that could more easily capture the ground surface, regardless of vegetation cover. Another option, at least for planted fields, would be to have UAS flights specifically for the purpose of capturing DEM data just after hay is harvested [95]. It may be that flights conducted during the winter are better able to capture the bare-earth surface without the aid of a LiDAR sensor. The DEM would need to be of adequate resolution in order for the canopy heights to retain the accuracy of the DSM [95]; estimates using lower-resolution DEMs may still be useful for grazing land management purposes, however, and could be a worthwhile target for future research.

#### *4.2.2 UAS Vegetation Indices for Forage Estimation*

##### *Comparison of Flights*

Overall the quality and quantity of the data captured in 2017 was much improved for the purpose of this study. Most importantly, the quadrat locations were consistently captured using RTK GPS. This ensured that every flight yielded usable data. In addition to consistently locating quadrats, the largest quadrat size was twice the size of the largest 2016 quadrat, and the two quadrat sizes were placed adjacent to one another in the field instead of nesting or superimposing the frames. Larger quadrats with no interior piping frames provided a much greater area available for analysis with less pixel contamination.

Figure 38 shows the disparity between the 2016 and 2017 flights in terms of the areas available for analysis. The 2017 flights had two visible quadrat sizes and far less pixel contamination. The 2016 flights not only had fewer visible quadrats, but the amount of pixel contamination was not only visibly more significant but likely had a strong impact on the results

of the analysis. The effect of soil background on spectral response has been shown to be significant [85], [96]. Lighter-colored soils have been shown to reduce NDVI values, so it may be that the PVC piping of the quadrats behaved like a highly-reflective, light-colored soil [85]. Adding to the complexity, soil brightness has been shown to affect VIs differently, depending on the spectral bands used [96]. Along with the relatively small area available for analysis, mixed spectral response from vegetation, soil, and the PVC quadrat piping may explain the seemingly erratic results from the 2016 flights. PVC quadrat piping was used again in 2017, but the 2016 flights used smaller quadrats where the impact of the quadrat piping on the spectral response may have been greater.

In this study, both the underlying soil types and the material used to create the quadrats impacted the results. While the effect of the spectral response of the PVC piping was somewhat ameliorated by tracing the interior of the quadrat areas to exclude visually affected pixels, it is not known to what extent the PVC quadrat piping had on the results. Since dark-colored soils can likewise impact the results of VIs, it may be that any material used to outline a quadrat will impact the quadrat's spectral response. Results could be improved by placing non-reflective markers at quadrat corners located by RTK GPS. Then a quadrat frame could be placed using the corner markers for a guide after each flight to facilitate the field measurements.

Finally, the 2017 flights used an irradiance sensor to help control for variations in lighting conditions, while the 2016 flights did not. The impact of the lighting conditions on the 2016 VI results are unknown, but the use of the irradiance sensor and the accompanying radiometric corrections to the orthomosaic used to create the VI rasters allow for more consistent results [97].

## *VI Assessment*

Referring back to Table 9 and Table 10, there was no one VI that had exceptionally better performance than the others. In 2016, NGRDI, ENDVI, and NDVI had comparable mean  $r^2$  values when considering all field measurements. NGRDI and ENDVI associated most strongly with average plant height ( $r^2$  of 0.34 and 0.29, respectively) while NDVI had its strongest associations with %DM in the 2016 flights. GNDVI was the weakest in the 2016 flights (Table 9), although it associated more strongly with HM in the 2016 flights than the other three VIs ( $r^2 = 0.19$ ). None of these average  $r^2$  values explain even 50% of the variations in the measurements, although some months had very high  $r^2$  values in 2016, as discussed in the previous section (Appendix I).

In 2017 the average  $r^2$  values are lower (Table 10), with the highest being 0.16 for ENDVI and its red-edge counterpart, and the red-edge NDVI. Overall the VIs in 2017 performed similarly, with average  $r^2$  values of 0.15 or 0.16 for all lab measurements. The red-edge VIs performed almost identically to their non-red-edge counterparts, seeming to perform slightly better with the % CP field measurements with the ENDVI and NDVI indices. As in 2016, some months had much higher than average correlations. The May 2017 flight of the Tifton field had  $r^2$  values approached 0.7 for the ENDVI and NDVI indices with the HM field measurement.

In their 2014 paper, Wang et al [7] showed decreasing performance of NDVI at predicting HM with increased flying height. A low flying height, on the other hand, produced very strong associations in their regression models ( $r^2 = 0.94$ ,  $p < 0.01$ ) [7]. While the opposite trend was observed in this study—flying height was lowered between 2016 and 2017, but the average  $r^2$  values decreased for all VIs and field measurements—many other parameters changed

as well, including the quadrat size and sensor. Future work may target lower flying heights with the eBee SQ sensor to see if the predictive power of the VIs increases at lower flying heights.

### *Field Measurements*

It is not clear from the data why a difference exists between the Sandy and Tifton fields in the results of the regression analysis for the same VI and field measurement combinations. Some important differences may be accounted for by the different forage species in each pasture and the management. The Sandy field was planted nearly 50 years ago and is not harvested annually for hay the way the Tifton field is. This could create significant differences in the growth habit and overall forage density, quantity, and nutritive value in each field.

Differences between crude protein regression analysis results in the Sandy and Tifton fields (Figure 53 and Figure 54 in Appendix I) may be due to the expression of crude protein on a DM basis instead of total. It may be that there is a stronger correlation of the vegetation indices with crude protein depending upon the amount of DM present in the sample. This could be investigated with future analyses involving different crude protein calculations.

### *Potential Sources of Error: Pixel Contamination*

While all reasonable efforts were made to control for error in the field data collection and subsequent UAS-derived VI analyses, potential sources of error remain that likely affected the results of this study. The 2016 quadrats had relatively small uncontaminated interior areas (less than 20% of the total quadrat area) to use for analysis. The 2016 flights also nested the smaller quadrats inside the larger quadrat frames, so while these smaller frames were not visible in the imagery and could not be analyzed separately in this study, the reflection of light from the smaller quadrat frames contributed to the overall pixel values. The high  $r^2$  values from the 2016 flights may be spurious given the relatively small area available for analyses, and may also be



significantly affected by the presence of the smaller quadrat frames within the interior quadrat areas.

The material used for the quadrat boundaries, PVC piping, is highly reflective and likely contributed to the results even in the 2017 flights. This highly visible material was instrumental in locating and digitizing the quadrats for the 2016 flights, when only the general quadrat locations were known. In 2017, however, the quadrat locations were collected using RTK GPS, making the highly reflective material of the quadrat frames unnecessary. A non-reflective material may improve the accuracy of results when RTK GPS quadrat locations are collected.

The determination of contaminated vs uncontaminated pixels for this study was subjective and had a large impact on the outcome of the study. The pixels selected for analysis were visually compared to their neighbors, but there was no benchmark pixel or stretch value used to determine what constituted the presence of contamination or an unacceptable level of contamination. This subjective pixel selection likely had a profound impact on the 2016 results as there were significantly fewer quadrats that were identified from the imagery, making the area available for analysis have a larger impact on the overall results for the year. The 2017 reflectance data was provided as separate raster bands instead of composite R-G-NIR images, which may have impacted the perception of pixel contamination even though the same visual selection process was used. For these reasons, the author recommends using a low- or non-reflective material in future flights and continued use of RTK GPS to place the quadrat corners in the imagery.

#### *Potential Sources of Error: Lighting Conditions*

As mentioned previously, the 2017 sensor, the Parrot Sequoia, has an upward-facing irradiance sensor that allows for a signal correction depending upon the lighting conditions at the

time of data collection [56], [59]. The 2016 flights, however, used a modified consumer-grade camera that did not allow for signal correction based on the lighting conditions. This means that the 2017 flights are more directly comparable to each other, while it is not known to what degree ambient lighting conditions may have affected the results of the 2016 flights, or whether the same months between years can be realistically compared to each other. The orthomosaics from the 2016 flights were not radiometrically calibrated to be directly comparable to each other, which causes issues when comparing between different fields on the same flight date, and between the same fields on different flight dates. Depending on the weather, the lack of an irradiance sensor may even cause more profound issues with an orthomosaic where images mosaicked together from the same flight and field cannot be directly compared. This could be the case if, for instance, a cloud passes over the sun during a flight. While the calibration targets help correct for these potential issues, the use of the irradiance sensor provides additional control for environmental conditions and better measurements of the spectral response of the objects being measured [56], [59], [98]. The impact to this study is that the use of the irradiance sensor in 2017 is another factor preventing direct comparison of the results generated from the 2016 flights, and may have influenced the results of the 2016 flights, as the lack of the irradiance calibration leads to a less accurate measurement of spectral responses [98], [99].

## CHAPTER 5: CONCLUSION AND FUTURE WORK

This study used UAS-SfM point clouds with orthomosaics from multispectral sensors to create DEMs, DSMs, and VIs to estimate biophysical parameters of plants such as plant height, biomass, crude protein content, and DM. UAS-SfM point clouds were classified using an iterative algorithm to separate ground from non-ground points in order to try and create a bare-earth DEM for use with the UAS-SfM DSM to create canopy height models. The point cloud classification was evaluated using test areas with known ground or non-ground features. The canopy height models were evaluated by comparing them to field measurements of average plant height.

Four separate VIs were created from the radiometrically corrected orthomosaic collected by the multispectral sensor. Values from each VI were extracted from quadrat locations in the orthomosaic that corresponded to field measurement locations. Field measurements were taken for each flight within quadrat locations distributed throughout the study area, in order to be compared to the flight data. Linear regression analyses were then performed against the VIs and the field measurements to determine whether a significant regression exists between one or more of the VIs with one or more field measurements.

The point cloud classification was found to be accurate in areas of high relief, but did not perform well enough where the ground surface was not visible to produce an accurate DEM. The canopy height models generated using this DEM were likewise shown to be poor predictors of measured plant height. With respect to the VIs, it was found that there is a significant regression between HM and NDVI and ENDVI, particularly when using the red-edge band in place of the NIR spectral band. The 2017 May flight over the Tifton field generated the most significant regression in the study. There were lesser but still significant regressions between

HM and the other vegetation indices used in this study. Crude protein content needs further study as it showed some promising but inconsistent results.

This study found promising results for using UAS-SfM-derived products to model plant biophysical properties. Additional improvements to experimental design, including controlling for pixel contamination and experimenting with lower flying heights, may yield stronger regressions with greater ability to predict field measurements. This study demonstrates the potential for UAS-SfM products to provide a powerful tool for monitoring forage health and productivity in grazing lands.

### **5.1 Future Research**

The DEMs generated in this study from the UAS-SfM point cloud were limited by the inability of the sensors to see the ground during flight. DEM quality could be improved by flying fields after hay harvesting or in the winter, when vegetation cover is minimal. This could then be used in conjunction with a UAS-SfM-derived DSM collected during the growing season. This would allow for a more accurate canopy height model to be calculated.

Pixel contamination posed a significant problem for this study and could be greatly reduced by using RTK-GPS for locating quadrat corners, placing a non-reflective marker at each corner, and then performing the UAS flight. Quadrat frames could then be placed on the corner markers in the field to facilitate the field measurements, using the corner markers as a guide. In this way the material used to define the quadrat boundaries would not affect the spectral response of the quadrat areas collected by the UAS sensor.

Lower flying heights were demonstrated by Wang et al [7] to have a significant impact on the strength of the regression between VIs and HM. While the flying heights were lowered in

the 2017 flights, it may be that lowering them further will help improve the results. Larger quadrat sizes may also help improve results, along with, or independently of, the flying height.

Preliminary work was done in this study on using point cloud metrics and structure to try and estimate field measurements of forage. This work is included in Appendix 2. Additional point cloud metrics such as point density and percentile heights should be analyzed to supplement the work done on the standard deviations of the heights within the quadrats to see if these metrics provide a useful tool for predicting field measurements of plant height and biomass.

## REFERENCES

- [1] “USDA/NASS 2017 State Agriculture Overview for Texas.” [Online]. Available: [https://www.nass.usda.gov/Quick\\_Stats/Ag\\_Overview/stateOverview.php?state=TEXAS](https://www.nass.usda.gov/Quick_Stats/Ag_Overview/stateOverview.php?state=TEXAS). [Accessed: 22-Aug-2018].
- [2] “Texas Ag Stats.” [Online]. Available: <http://www.texasagriculture.gov/About/TexasAgStats.aspx>. [Accessed: 22-Aug-2018].
- [3] C. Zhang and J. Kovacs, “The application of small unmanned aerial systems for precision agriculture: a review,” *Precis. Agric.*, vol. 13, no. 6, pp. 693–712, Dec. 2012.
- [4] A. McBratney, B. Whelan, T. Ancev, and J. Bouma, “Future Directions of Precision Agriculture,” *Precis. Agric.*, vol. 6, no. 1, pp. 7–23, Feb. 2005.
- [5] D. J. Mulla, “Twenty five years of remote sensing in precision agriculture: Key advances and remaining knowledge gaps,” *Biosyst. Eng.*, vol. 114, no. 4, pp. 358–371, Apr. 2013.
- [6] R.R. Pullanagari, I. Yule, W. King, D. Dalley, and R. Dynes, “The Use of Optical Sensors to Estimate Pasture Quality,” *Int. J. Smart Sens. Intell. Syst.*, vol. 4, no. 1, pp. 125–137, Mar. 2011.
- [7] Chuyuan Wang, K. P. Price, D. van der Merwe, Nan An, and Huan Wang, “Modeling Above-Ground Biomass in Tallgrass Prairie Using Ultra-High Spatial Resolution sUAS Imagery,” *Photogramm. Eng. Remote Sens.*, vol. 80, no. 12, p. 1151, Dec. 2014.
- [8] “Spectral Indices.” [Online]. Available: <https://www.harrisgeospatial.com/docs/SpectralIndices.html>. [Accessed: 14-Oct-2018].
- [9] “Measuring Vegetation (NDVI & EVI),” 30-Aug-2000. [Online]. Available: [https://earthobservatory.nasa.gov/Features/MeasuringVegetation/measuring\\_vegetation\\_2.php](https://earthobservatory.nasa.gov/Features/MeasuringVegetation/measuring_vegetation_2.php). [Accessed: 14-Oct-2018].
- [10] “Vegetation Analysis: Using Vegetation Indices in ENVI,” *Harris Geospatial Solutions*. [Online]. Available: <https://www.harrisgeospatial.com/Learn/Whitepapers/TabId/2359/ArtMID/10212/ArticleID/16162/Vegetation-Analysis-Using-Vegetation-Indices-in-ENVI.aspx>. [Accessed: 01-Sep-2018].
- [11] “USDA ERS - Major Land Uses.” [Online]. Available: <https://www.ers.usda.gov/data-products/major-land-uses/>. [Accessed: 28-Nov-2018].
- [12] A. S. Laliberte, J. E. Herrick, A. Rango, and C. Winters, “Acquisition, Orthorectification, and Object-based Classification of Unmanned Aerial Vehicle (UAV) Imagery for Rangeland Monitoring,” *Photogramm. Eng. Remote Sens.*, vol. 76, no. 6, pp. 661–672, Jun. 2010.
- [13] “Fly under the Small UAS Rule.” [Online]. Available: [https://www.faa.gov/uas/getting\\_started/part\\_107/#reg\\_req](https://www.faa.gov/uas/getting_started/part_107/#reg_req). [Accessed: 14-Oct-2018].

- [14] J. Torres-Sánchez, J. M. Peña, A. I. de Castro, and F. López-Granados, “Multi-temporal mapping of the vegetation fraction in early-season wheat fields using images from UAV,” *Comput. Electron. Agric.*, vol. 103, pp. 104–113, Apr. 2014.
- [15] J. Torres-Sánchez, F. López-Granados, and J. M. Peña, “An automatic object-based method for optimal thresholding in UAV images: Application for vegetation detection in herbaceous crops,” *Comput. Electron. Agric.*, vol. 114, pp. 43–52, Jun. 2015.
- [16] R. Jannoura, K. Brinkmann, D. Uteau, C. Bruns, and R. G. Joergensen, “Monitoring of crop biomass using true colour aerial photographs taken from a remote controlled hexacopter,” *Biosyst. Eng.*, vol. 129, pp. 341–351, Jan. 2015.
- [17] J. Gago *et al.*, “UAVs challenge to assess water stress for sustainable agriculture,” *Agric. Water Manag.*, vol. 153, pp. 9–19, May 2015.
- [18] M. G. Trotter, D. W. Lamb, G. E. Donald, and D. A. Schneider, “Evaluating an active optical sensor for quantifying and mapping green herbage mass and growth in a perennial grass pasture,” *Crop Pasture Sci.*, vol. 61, no. 5, p. 389, 2010.
- [19] P. J. Van Soest, *Nutritional ecology of the ruminant*. Cornell University Press, 1994.
- [20] S. W. Todd, R. M. Hoffer, and D. G. Milchunas, “Biomass estimation on grazed and ungrazed rangelands using spectral indices,” *Int. J. Remote Sens.*, vol. 19, no. 3, pp. 427–438, Jan. 1998.
- [21] R. F. Barnes, C. J. Nelson, M. Collins, K. J. Moore, and others, *Forages. Volume 1: An introduction to grassland agriculture*. Iowa State University Press, 2003.
- [22] J. Hunt *et al.*, “Applications and Research Using Remote Sensing for Rangeland Management,” *Photogramm. Eng. Remote Sens.*, vol. 69, no. 6, pp. 675–693, Jun. 2003.
- [23] P. j. Starks, D. Zhao, W. a. Phillips, and S. w. Coleman, “Herbage mass, nutritive value and canopy spectral reflectance of bermudagrass pastures,” *Grass Forage Sci. J. Br. Grassl. Soc.*, no. 2, 2006.
- [24] M. Weinmann, *Reconstruction and Analysis of 3D Scenes: From Irregularly Distributed 3D Points to Object Classes*. Springer International Publishing, 2016.
- [25] M. J. Westoby, J. Brasington, N. F. Glasser, M. J. Hambrey, and J. M. Reynolds, “‘Structure-from-Motion’ photogrammetry: A low-cost, effective tool for geoscience applications,” *Geomorphology*, vol. 179, pp. 300–314, Dec. 2012.
- [26] D. G. Lowe, “Distinctive image features from scale-invariant keypoints,” *Int. J. Comput. Vis.*, vol. 60, no. 2, pp. 91–110, 2004.
- [27] M. R. James and S. Robson, “Straightforward reconstruction of 3D surfaces and topography with a camera: Accuracy and geoscience application,” *J. Geophys. Res. Earth Surf.*, vol. 117, no. F3, p. F03017, Sep. 2012.

- [28] A. S. Woodget, P. E. Carbonneau, F. Visser, and I. P. Maddock, “Quantifying submerged fluvial topography using hyperspatial resolution UAS imagery and structure from motion photogrammetry,” *Earth Surf. Process. Landf.*, vol. 40, no. 1, pp. 47–64, Jan. 2015.
- [29] “(PDF) Exploring the use of 3D GIS as an analytical tool in archaeological excavation practice.” [Online]. Available: [https://www.researchgate.net/publication/303824023\\_Exploring\\_the\\_use\\_of\\_3D\\_GIS\\_as\\_an\\_analytical\\_tool\\_in\\_archaeological\\_excavation\\_practice?\\_sg=nDjrv0M-KqWAGma\\_JH2yqOO8P9Jqo7cjHmLDt22ZvT7FTzKDTX6rYd1jgSh1aTokZzsr6ZC71A](https://www.researchgate.net/publication/303824023_Exploring_the_use_of_3D_GIS_as_an_analytical_tool_in_archaeological_excavation_practice?_sg=nDjrv0M-KqWAGma_JH2yqOO8P9Jqo7cjHmLDt22ZvT7FTzKDTX6rYd1jgSh1aTokZzsr6ZC71A). [Accessed: 01-Sep-2018].
- [30] Y. Reshetyuk and S.-G. Mårtensson, “Generation of Highly Accurate Digital Elevation Models with Unmanned Aerial Vehicles,” *Photogramm. Rec.*, vol. 31, no. 154, pp. 143–165, Jun. 2016.
- [31] Biplov Bhandari, Upendra Oli, Niroz Panta, and Uttam Pudasaini, “Generation of High Resolution DSM Using UAV Images,” in *From the Wisdom of the Ages to the Challenges of the Modern World*, Sofia, Bulgaria, 2015.
- [32] “DEM, DSM & DTM Differences - A Look at Elevation Models in GIS,” *GIS Geography*, 09-Mar-2016. .
- [33] J. Estornell, L. A. Ruiz, B. Velázquez-Martí, and A. Fernández-Sarría, “Estimation of shrub biomass by airborne LiDAR data in small forest stands,” *For. Ecol. Manag.*, vol. 262, no. 9, pp. 1697–1703, Nov. 2011.
- [34] E. W. Bork and J. G. Su, “Integrating LIDAR data and multispectral imagery for enhanced classification of rangeland vegetation: A meta analysis,” *Remote Sens. Environ.*, vol. 111, no. 1, pp. 11–24, Nov. 2007.
- [35] J. L. R. Jensen and A. J. Mathews, “Assessment of Image-Based Point Cloud Products to Generate a Bare Earth Surface and Estimate Canopy Heights in a Woodland Ecosystem,” *Remote Sens.*, vol. 8, no. 1, p. 50, Jan. 2016.
- [36] L. Javernick, J. Brasington, and B. Caruso, “Modeling the topography of shallow braided rivers using Structure-from-Motion photogrammetry,” *Geomorphology*, vol. 213, pp. 166–182, May 2014.
- [37] D. W. Bailey, D. D. Kress, D. C. Anderson, D. L. Boss, and E. T. Miller, “Relationship between terrain use and performance of beef cows grazing foothill rangeland,” *J. Anim. Sci.*, vol. 79, no. 7, pp. 1883–1891, Jul. 2001.
- [38] J. Geipel, J. Link, W. Claupein, J. Geipel, J. Link, and W. Claupein, “Combined Spectral and Spatial Modeling of Corn Yield Based on Aerial Images and Crop Surface Models Acquired with an Unmanned Aircraft System,” *Remote Sens.*, vol. 6, no. 11, pp. 10335–10355, Oct. 2014.



- [39] M. Possoch, S. Bieker, D. Hoffmeister, A. Bolten, J. Schellberg, and G. Bareth, “Multi-Temporal Crop Surface Models Combined with the Rgb Vegetation Index from Uav-Based Images for Forage Monitoring in Grassland,” in *The International Archives of Photogrammetry, Remote Sensing and Spatial Information Sciences; Gottingen*, Gottingen, Germany, Gottingen, 2016, vol. XLI-B1, pp. 991–998.
- [40] J. Schellberg, M. J. Hill, R. Gerhards, M. Rothmund, and M. Braun, “Precision agriculture on grassland: Applications, perspectives and constraints,” *Eur. J. Agron.*, vol. 29, no. 2, pp. 59–71, Aug. 2008.
- [41] Jamie Foster, “Background info on Beeville fields - lauraecarbajal@gmail.com - Gmail.”
- [42] L. Russell, D. P. Anderson, M. T. Bochat, B. D. Yanta, J. Paschal, and A. M. Young, “Effects of Brahman Influence on Breeding Female Prices in South Texas,” 2015.
- [43] “Forage Agronomy | Texas A&M Research & Extension Center at Corpus Christi.” [Online]. Available: <https://ccag.tamu.edu/forage-agronomy/>. [Accessed: 24-Oct-2018].
- [44] “South Texas study results show Brahman, crossbred influence receive higher premiums,” *AgriLife Today*, 15-Jul-2014. [Online]. Available: <https://today.agrilife.org/2014/07/15/south-texas-study-results-show-brahman-crossbred-influence-receive-higher-premiums/>. [Accessed: 24-Oct-2018].
- [45] “Huisache | Texas Natural Resources Server.” [Online]. Available: <https://texnat.tamu.edu/about/brush-busters/huisache/>. [Accessed: 02-Sep-2018].
- [46] “Plants of Texas Rangelands » Huisache.” [Online]. Available: <https://rangeplants.tamu.edu/plant/huisache/>. [Accessed: 02-Sep-2018].
- [47] “Plants of Texas Rangelands » Mesquite.” [Online]. Available: <https://rangeplants.tamu.edu/plant/mesquite/>. [Accessed: 02-Sep-2018].
- [48] “AgriLife Extension expert talks Bermuda grass 101,” *AgriLife Today*, 26-May-2018. [Online]. Available: <https://today.agrilife.org/2018/05/26/agrilife-extension-expert-talks-bermuda-grass-101/>. [Accessed: 02-Sep-2018].
- [49] “Plants of Texas Rangelands » Buffelgrass.” [Online]. Available: <https://rangeplants.tamu.edu/plant/buffelgrass/>. [Accessed: 28-Nov-2018].
- [50] “TIFTON 85 BERMUDAGRASS.” [Online]. Available: <http://www.tifton.uga.edu/fat/tifton85.htm>. [Accessed: 02-Sep-2018].
- [51] “SoilWeb.” [Online]. Available: [https://casoilresource.lawr.ucdavis.edu/soil\\_web/ssurgo.php?action=list\\_mapunits&areasymbol=tx025](https://casoilresource.lawr.ucdavis.edu/soil_web/ssurgo.php?action=list_mapunits&areasymbol=tx025). [Accessed: 02-Sep-2018].
- [52] “senseFly - eBee,” *senseFly*. [Online]. Available: <https://www.sensefly.com/drone/ebee-mapping-drone>. [Accessed: 02-Jun-2018].

- [53] *S110 RGB/NIR/RE camera User Manual*, Revision 3. Cheseaux-Lausanne, Switzerland: senseFly Ltd, 2014.
- [54] Jake Berryhill, “Info on Beeville postprocessing - lauraecarbajal@gmail.com - Gmail.”
- [55] “Light Sensors: the Basics (DLS and Sunshine Sensor),” *MicaSense Knowledge Base*. [Online]. Available: <http://support.micasense.com/hc/en-us/articles/115002782008-Light-Sensors-the-Basics-DLS-and-Sunshine-Sensor->. [Accessed: 22-Oct-2018].
- [56] “What does the Sunshine (Irradiance) Sensor on Sequoia do?,” *MicaSense Knowledge Base*. [Online]. Available: <http://support.micasense.com/hc/en-us/articles/216533688-What-does-the-Sunshine-Irradiance-Sensor-on-Sequoia-do->. [Accessed: 22-Oct-2018].
- [57] senseFly Parrot Group, “Parrot Sequoia Technical Specifications.” senseFly Ltd.
- [58] D. N. H. Horler, M. Dockray, J. Barber, and A. R. Barringer, “Red edge measurements for remotely sensing plant chlorophyll content,” *Adv. Space Res.*, vol. 3, no. 2, pp. 273–277, Jan. 1983.
- [59] “senseFly - eBee SQ,” *senseFly*. [Online]. Available: <https://www.sensefly.com/drone/ebec-sq-agriculture-drone>. [Accessed: 02-Jun-2018].
- [60] “eMotion Ag - senseFly.” [Online]. Available: <https://www.sensefly.com/software/emotion-ag/>. [Accessed: 03-Sep-2018].
- [61] “Ground sampling distance (GSD),” *Support*. [Online]. Available: <http://support.pix4d.com/hc/en-us/articles/202559809-Ground-sampling-distance-GSD->. [Accessed: 25-Oct-2018].
- [62] “Info on Beeville, Field Data Collection - lauraecarbajal@gmail.com - Gmail.” [Online]. Available: <https://mail.google.com/mail/u/0/#inbox/KtbxLzFrMrHrGrnhnPvRIJWVcnkxkZhzvq>. [Accessed: 24-Oct-2018].
- [63] NFTA, “Moisture Task Force Report, 2.2.2.5 Laboratory Dry Matter by Oven Drying for 3 hours at 105C,” 2001.
- [64] Association of Official Analytical Chemists, *Official Methods of Analysis*, 16th ed. Arlington, VA, USA: Association of Official Analytical Chemists Inc., 1995.
- [65] “How to process Sequoia imagery,” *Support*. [Online]. Available: <http://support.pix4d.com/hc/en-us/articles/209362146-How-to-process-Sequoia-imagery>. [Accessed: 25-Oct-2018].
- [66] “Radiometric calibration target,” *Support*. [Online]. Available: <http://support.pix4d.com/hc/en-us/articles/206494883-Radiometric-calibration-target>. [Accessed: 26-Oct-2018].

- [67] “What does step 1. Initial Processing do?,” *Support*. [Online]. Available: <http://support.pix4d.com/hc/en-us/articles/202559339-What-does-step-1-Initial-Processing-do->. [Accessed: 26-Oct-2018].
- [68] T. Schenk, “Towards automatic aerial triangulation,” *ISPRS J. Photogramm. Remote Sens.*, vol. 52, no. 3, pp. 110–121, Jun. 1997.
- [69] O. Küng *et al.*, “The Accuracy of Automatic Photogrammetric Techniques on Ultra-light UAV Imagery,” 2011.
- [70] D. Gomez-Candon, A. I. Castro, and F. Lopez-Granados, “Assessing the accuracy of mosaics from unmanned aerial vehicle (UAV) imagery for precision agriculture purposes in wheat,” *Precis. Agric.*, no. 1, p. 44, 2014.
- [71] “Radiometric corrections,” *Support*. [Online]. Available: <http://support.pix4d.com/hc/en-us/articles/202559509-Radiometric-corrections>. [Accessed: 26-Oct-2018].
- [72] A. S. Laliberte, M. A. Goforth, C. M. Steele, and A. Rango, “Multispectral remote sensing from unmanned aircraft: image processing workflows and applications for rangeland environments,” *ARS USDA Submiss.*, no. 11, 2011.
- [73] L. Wallace *et al.*, “Assessment of Forest Structure Using Two UAV Techniques: A Comparison of Airborne Laser Scanning and Structure from Motion (SfM) Point Clouds,” *Forests*, vol. 7, no. 3, p. 62, Mar. 2016.
- [74] S. Cooper *et al.*, “Examination of the Potential of Terrestrial Laser Scanning and Structure-from-Motion Photogrammetry for Rapid Nondestructive Field Measurement of Grass Biomass,” *Remote Sens.*, vol. 9, no. 6, p. 531, May 2017.
- [75] rapidlasso and Martin Isenburg, “LAStools: converting, filtering, viewing, processing, and compressing LIDAR data in LAS format.” [Online]. Available: <http://www.cs.unc.edu/~isenburg/lastools/>. [Accessed: 18-Nov-2016].
- [76] M. Isenburg, “Processing Large Dense-Matching Point Clouds,” *rapidlasso GmbH*, 25-Aug-2014. .
- [77] M. Isenburg, “LASindex – spatial indexing of LiDAR data,” *rapidlasso GmbH*, 03-Dec-2012. .
- [78] “lastile,” *rapidlasso GmbH*, 26-Dec-2012. .
- [79] “lassort,” *rapidlasso GmbH*, 26-Dec-2012. .
- [80] Axelsson, Peter, “DEM Generation from Laser Scanner Data Using Adaptive TIN Models,” *Int. Arch. Photogramm. Remote Sens.*, vol. XXXIII, no. Part B4/1, pp. 110–117, 2000.
- [81] “lasground,” *rapidlasso GmbH*, 23-Dec-2012. .

- [82] H. Kim *et al.*, “An Efficient Implementation of a Local Binning Algorithm for Digital Elevation Model Generation of LiDAR/ALSM Dataset,” *AGU Fall Meet. Abstr.*, vol. 2006, pp. G53C-0921, Dec. 2006.
- [83] S. Wu, J. Li, and G. H. Huang, “A study on DEM-derived primary topographic attributes for hydrologic applications: Sensitivity to elevation data resolution,” *Appl. Geogr.*, vol. 28, no. 3, pp. 210–223, Jul. 2008.
- [84] “How Focal Statistics works—Help | ArcGIS for Desktop.” [Online]. Available: <http://desktop.arcgis.com/en/arcmap/10.3/tools/spatial-analyst-toolbox/how-focal-statistics-works.htm>. [Accessed: 30-Oct-2018].
- [85] A. R. Huete and R. D. Jackson, “Suitability of spectral indices for evaluating vegetation characteristics on arid rangelands,” *Remote Sens. Environ.*, vol. 23, no. 2, pp. 213-IN8, Nov. 1987.
- [86] J. Rasmussen, G. Ntakos, J. Nielsen, J. Svensgaard, R. N. Poulsen, and S. Christensen, “Are vegetation indices derived from consumer-grade cameras mounted on UAVs sufficiently reliable for assessing experimental plots?,” *Eur. J. Agron.*, vol. 74, pp. 75–92, Mar. 2016.
- [87] H. Zheng *et al.*, “Evaluation of RGB, Color-Infrared and Multispectral Images Acquired from Unmanned Aerial Systems for the Estimation of Nitrogen Accumulation in Rice,” *Remote Sens.*, vol. 10, no. 6, p. 824, May 2018.
- [88] S. M. Moges, W. R. Raun, R. W. Mullen, K. W. Freeman, G. V. Johnson, and J. B. Solie, “Evaluation of Green, Red, and Near Infrared Bands for Predicting Winter Wheat Biomass, Nitrogen Uptake, and Final Grain Yield,” *J. Plant Nutr.*, vol. 27, no. 8, pp. 1431–1441, Jan. 2005.
- [89] A. A. Gitelson, Y. J. Kaufman, and M. N. Merzlyak, “Use of a green channel in remote sensing of global vegetation from EOS-MODIS,” *Remote Sens. Environ.*, vol. 58, no. 3, pp. 289–298, Dec. 1996.
- [90] “ENDVI.” [Online]. Available: <https://www.maxmax.com/endvi.htm>. [Accessed: 28-Oct-2018].
- [91] C. Zhao, L. Liu, J. Wang, W. Huang, X. Song, and C. Li, “Predicting grain protein content of winter wheat using remote sensing data based on nitrogen status and water stress,” *Int. J. Appl. Earth Obs. Geoinformation*, vol. 7, no. 1, pp. 1–9, May 2005.
- [92] J. W. Rouse, “Monitoring vegetation systems in the Great Plains with ERTS,” 1974.
- [93] A. A. Gitelson, Y. J. Kaufman, R. Stark, and D. Rundquist, “Novel algorithms for remote estimation of vegetation fraction,” *Remote Sens. Environ.*, vol. 80, no. 1, pp. 76–87, Apr. 2002.

- [94] J. Lisein *et al.*, “A Photogrammetric Workflow for the Creation of a Forest Canopy Height Model from Small Unmanned Aerial System Imagery,” *Forests*, vol. 4, no. 4, pp. 922–944, Nov. 2013.
- [95] Grenzdörffer, G.J., “Crop height determination with UAS point clouds,” *Int. Arch. Photogramm. Remote Sens. Spat. Inf. Sci.*, vol. XL–1, 2014.
- [96] A. R. Huete, R. D. Jackson, and D. F. Post, “Spectral response of a plant canopy with different soil backgrounds,” *Remote Sens. Environ.*, vol. 17, no. 1, pp. 37–53, Feb. 1985.
- [97] A. S. Laliberte, C. Winters, and A. Rango, “UAS remote sensing missions for rangeland applications,” *Geocarto Int.*, vol. 26, no. 2, pp. 141–156, Apr. 2011.
- [98] J. Kelcey, A. Lucieer, J. Kelcey, and A. Lucieer, “Sensor Correction of a 6-Band Multispectral Imaging Sensor for UAV Remote Sensing,” *Remote Sens.*, vol. 4, no. 5, pp. 1462–1493, May 2012.
- [99] S. Del Pozo *et al.*, “Vicarious Radiometric Calibration of a Multispectral Camera on Board an Unmanned Aerial System,” *Remote Sens.*, vol. 6, no. 3, pp. 1918–1937, Feb. 2014.

LIST OF APPENDICES

APPENDIX	PAGE
APPENDIX 1: MONTHLY FLIGHT RESULTS.....	86
APPENDIX 2: UAS-SFM POINT CLOUD METRICS VS FORAGE MEASUREMENTS.....	90
APPENDIX 3: POINT CLOUD CLASSIFICATION CODE.....	92

## APPENDIX 1: MONTHLY FLIGHT RESULTS

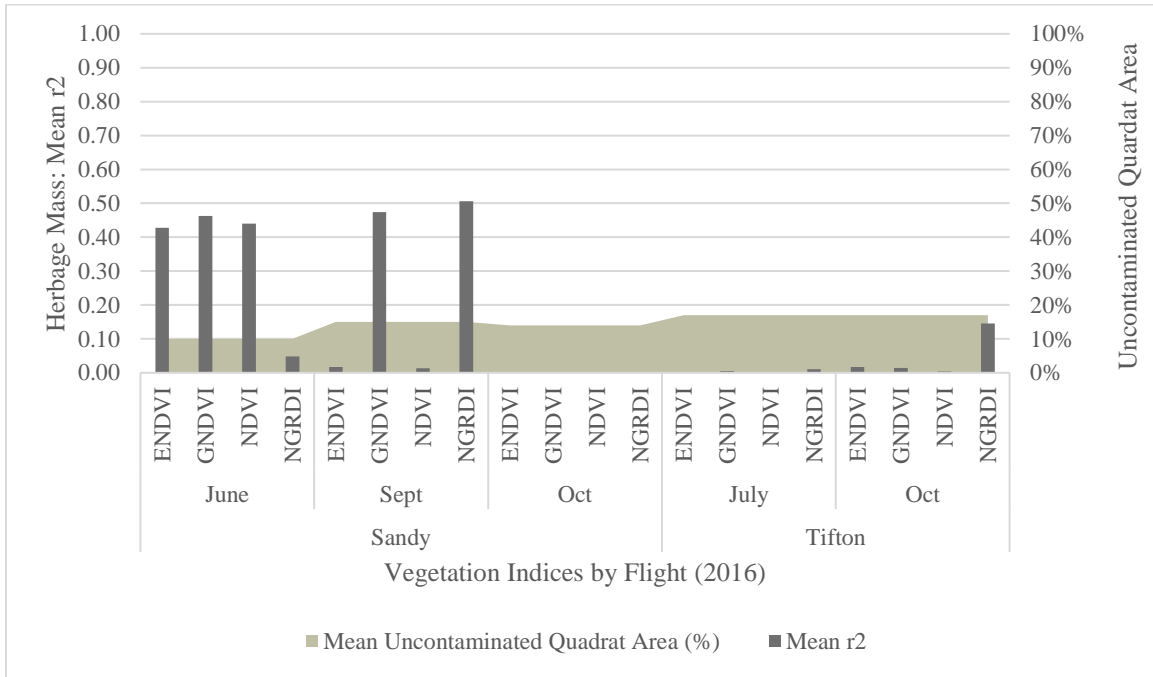


Figure 47.  $r^2$  values based on the regression analysis of each VI vs HM for the 2016 flights. The mean uncontaminated quadrat area (%) is also shown as an area plot.

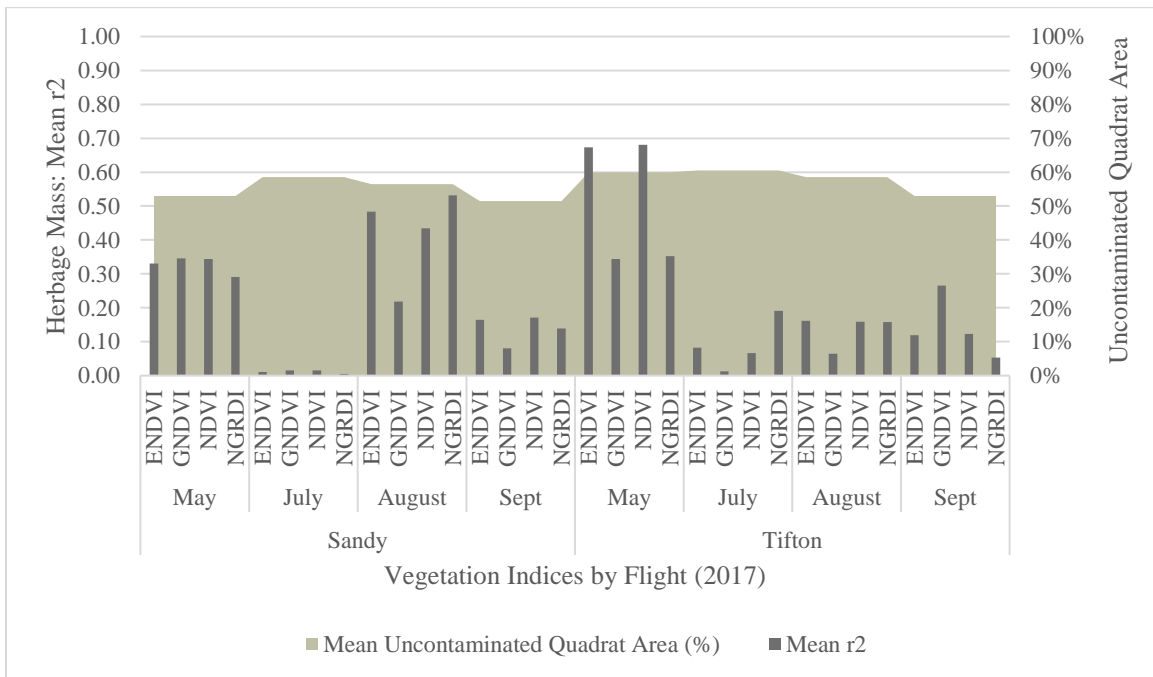


Figure 48.  $r^2$  values based on the regression analysis of each VI vs HM for the 2017 flights. The mean uncontaminated quadrat area (%) is also shown as an area plot.

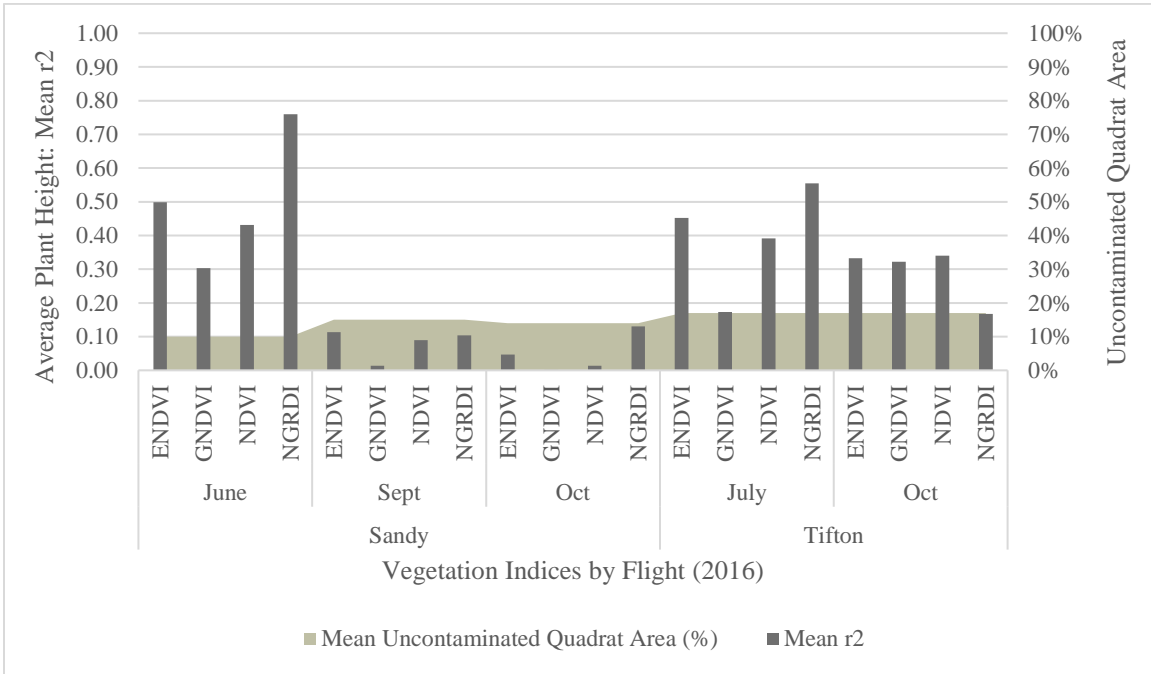


Figure 49.  $r^2$  values based on the regression analysis of each VI vs average plant height in centimeters for the 2016 flights. The mean uncontaminated quadrat area (%) is also shown as an area plot.

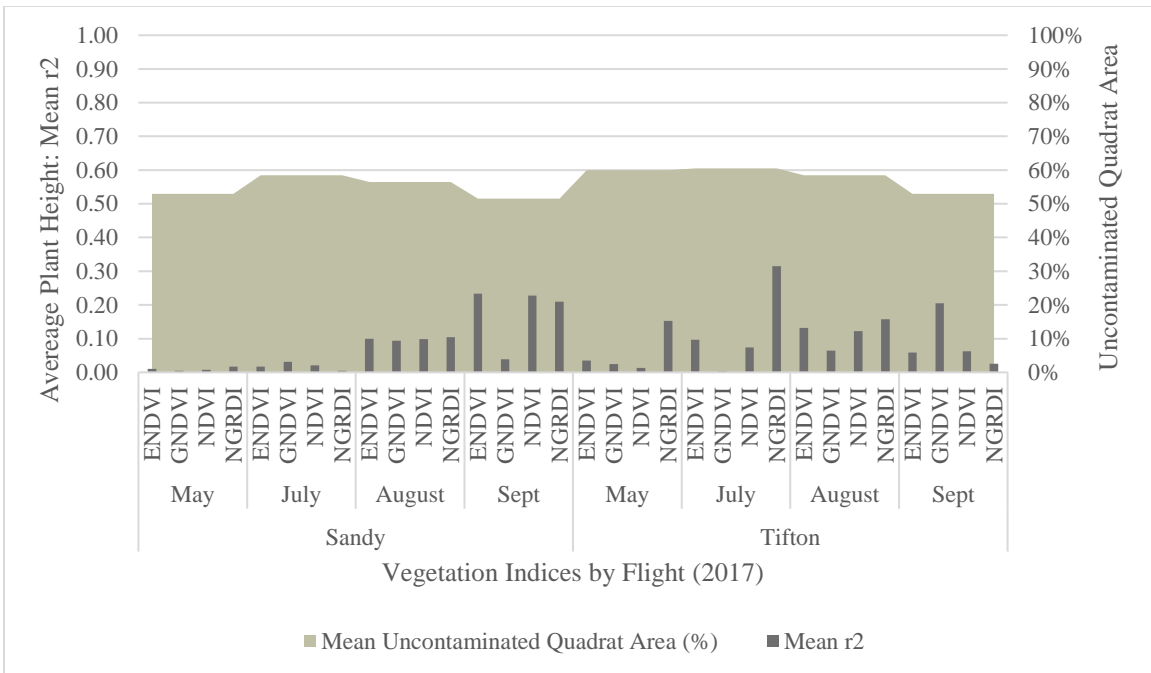


Figure 50.  $r^2$  values based on the regression analysis of each VI vs average plant height in centimeters for the 2017 flights. The mean uncontaminated quadrat area (%) is also shown as an area plot.



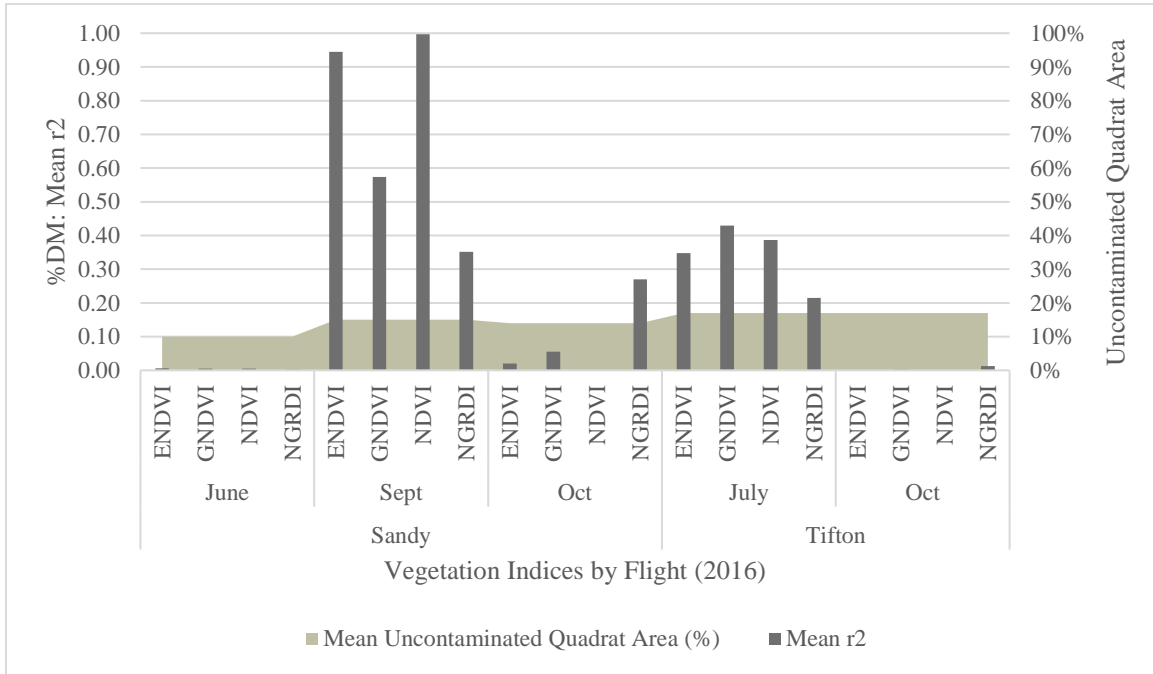


Figure 51.  $r^2$  values based on the regression analysis of each VI vs % DM for the 2016 flights. The mean uncontaminated quadrat area (%) is also shown as an area plot.

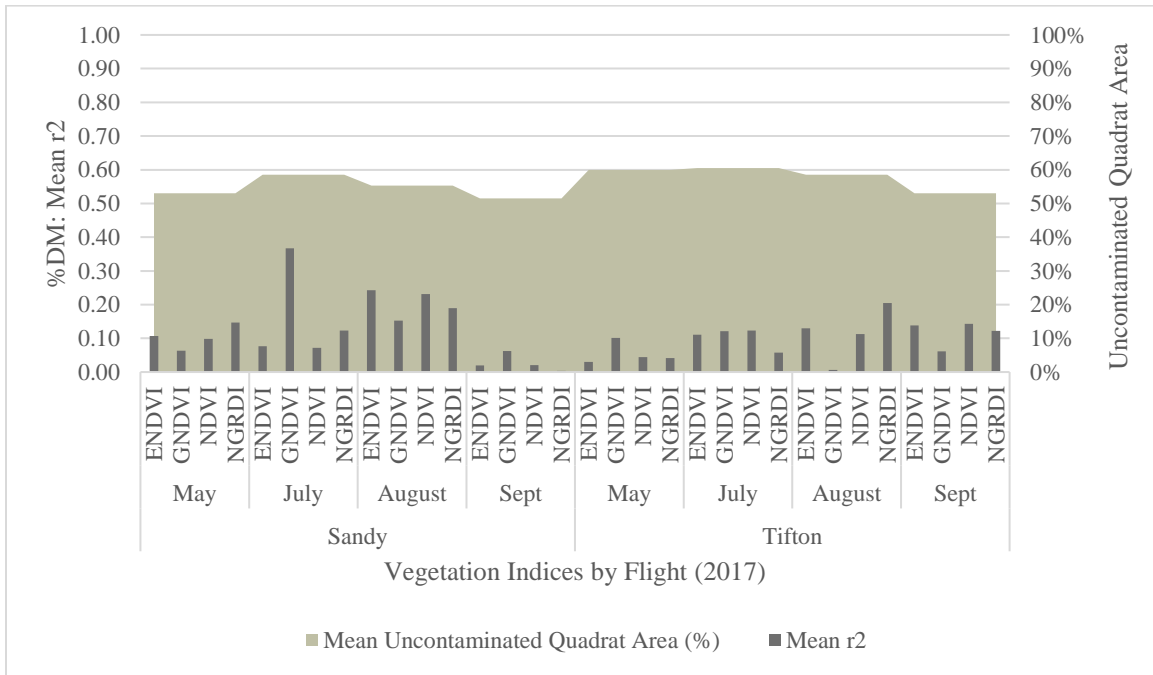


Figure 52.  $r^2$  values based on the regression analysis of each VI vs % DM for the 2017 flights. The mean uncontaminated quadrat area (%) is also shown as an area plot.

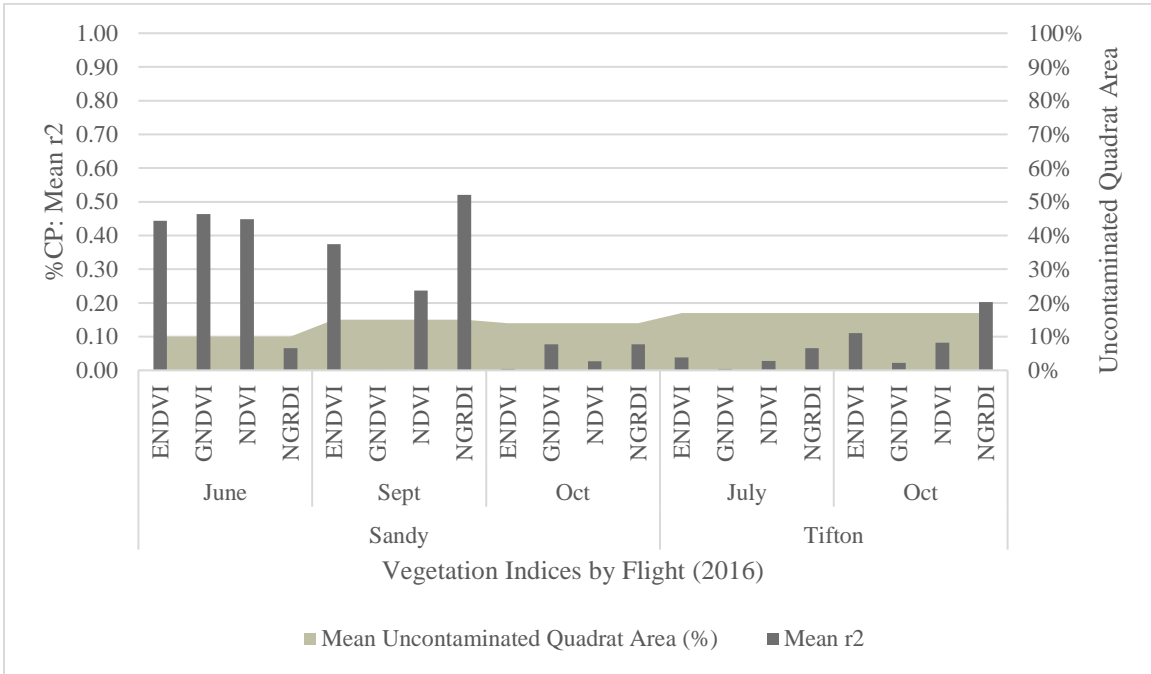


Figure 53.  $r^2$  values based on the regression analysis of each VI vs % Crude Protein (CP) for the 2016 flights . The mean uncontaminated quadrat area (%) is also shown as an area plot.

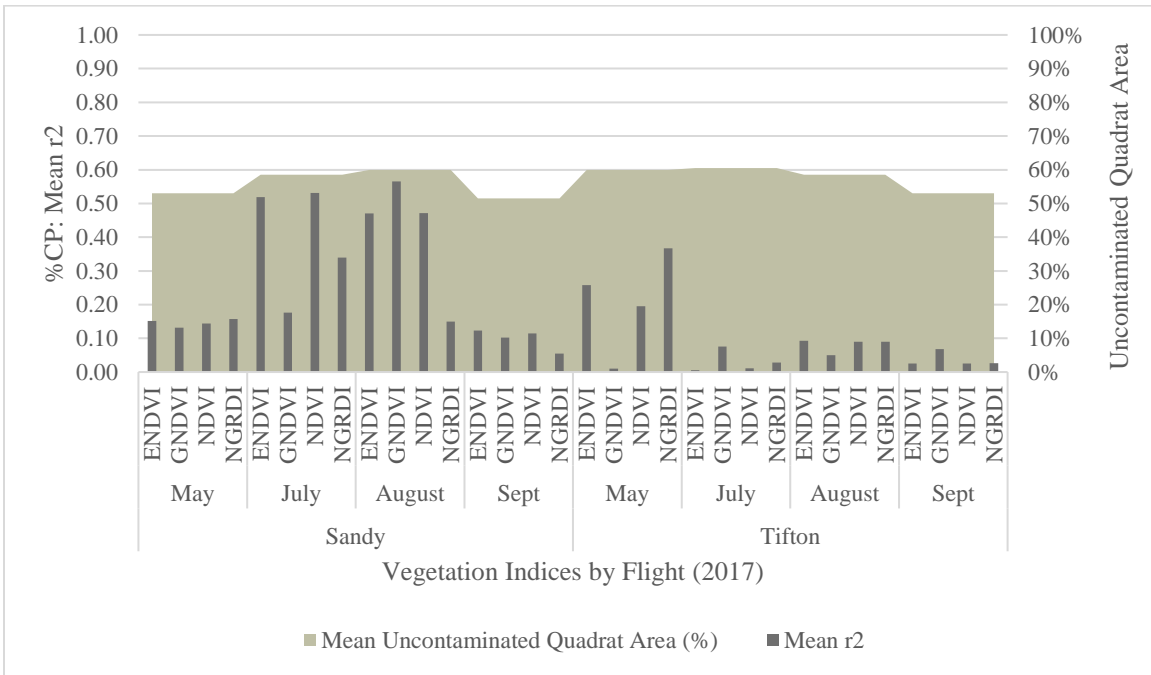
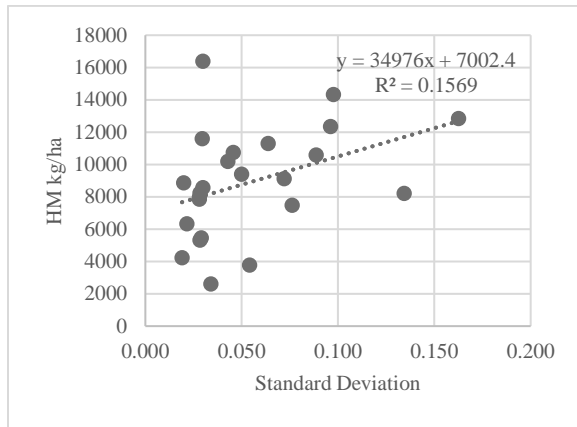


Figure 54.  $r^2$  values based on the regression analysis of each VI vs % CP for the 2017 flights . The mean uncontaminated quadrat area (%) is also shown as an area plot.

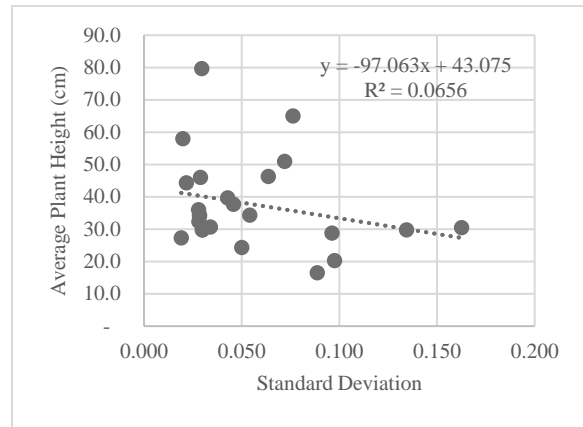
## APPENDIX 2: UAS-SfM POINT CLOUD METRICS VS FORAGE MEASURE

Statistical analysis of a point cloud provides an additional method for using UAS-SfM point clouds for estimating plant height, biomass, and other plant properties. The UAS-SfM point cloud statistics may be helpful for estimating plant height when a high-resolution DEM is not available for creating an accurate CHM [95]. To explore the relationship between the UAS-SfM point cloud properties and field measurements, statistics were calculated for the unclassified point cloud at each quadrat location for the 2016 flights. The unclassified point cloud was used as the vegetation canopy captured in the non-ground points were of principle interest for this portion of the analysis [95]. The minimum, maximum, and mean elevation for the unclassified UAS-SfM point cloud was calculated within each quadrat area, along with the point count and standard deviation of the point heights. The standard deviation of the point heights within the quadrat area was used to measure the point cloud structure and was compared to each of the laboratory measures for each field for all flights. The relationship between the height metrics and point density of the UAS-SfM point cloud have not yet been analyzed in relationship to the field measurements and represent an area for future work.

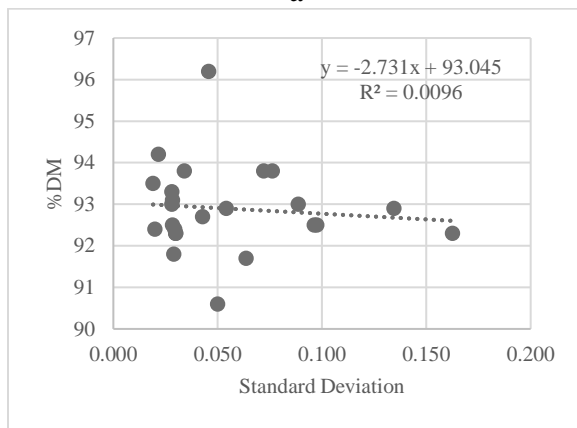
The regression analysis between the standard deviation of point heights within the quadrat area and the field measurements does not indicate a strong correlation with the field measurements. For the 2016 Sandy field data, the most significant result was with the HM measurement which yielded an  $r^2$  value of 0.16, indicating that only 16% of the variance is explained by the regression model. The rest of the regression models explain less than 10% of the variance with plant height, percent crude protein (%CP), and percent DM. These results are shown in Figure 55.



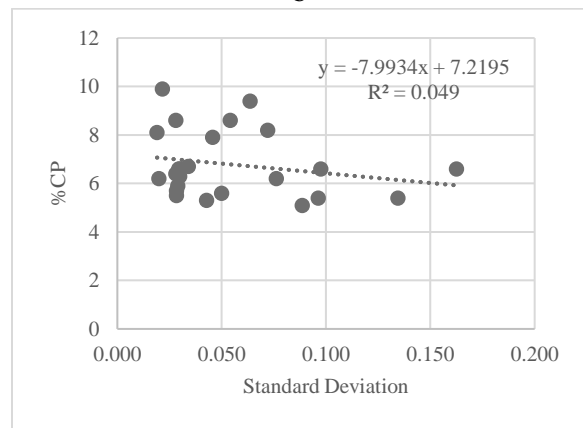
a



b



c



d

Figure 55. The results of the regression analysis between the standard deviation of point heights with (a) HM (kg/ha); (b) Average Plant Height (cm); (c) %DM; (d) %CP. Values are for the 2016 flights only.

## APPENDIX 3: POINT CLOUD CLASSIFICATION CODE

```

"""
Creates a folder directory to hold all the outputs.
Recursively tiles and segments point clouds.
"""

import os
import sys
import subprocess
import shlex
import shutil
import datetime
import time
from Tkinter import Tk
import tkinterFileDialog
import tkinterMessageBox

def point_cloud_processing(r, main_dir, raw_pt_cld, tile_size, spike, bulge, step):
    """Process for processing point clouds"""
    # Argument List for lastools
    args_list = [
        ("Tiling point cloud", raw_pt_cld, shlex.split(r"lastile -i *.las -odir '{0}' -tile_size {1} -buffer 5 -cores
8").format(os.path.join(main_dir, "Tiles"), tile_size)),
        ("Sorting tiles", os.path.join(main_dir, "Tiles"), shlex.split(r"lassort -i *.las -odir '{0}'").format(os.path.join(main_dir,
"SortedTiles"))),
        ("Classifying points", os.path.join(main_dir, "SortedTiles"), shlex.split(r"lasground -i *.las -odir '{0}' -spike {1} {2} -
step {3}").format(os.path.join(main_dir, "Ground"), spike, bulge, step)),
        ("Remove buffers", os.path.join(main_dir, "ClassReset"), shlex.split(r"lastile -i *.las -odir '{0}' -
remove_buffer").format(os.path.join(main_dir, "RemoveBuffers"))),
        ("Merge Tiles", os.path.join(main_dir, "RemoveBuffers"), shlex.split(r"lasmerge -i *.las -odir '{0}' -o
Pass{1}.las").format(os.path.join(main_dir, "NewCloud"), r))
    ]

    # Handle point reclassification
    if r < (len(passes)-1):
        args_list[3] = ("Keep ground points and reset class", os.path.join(main_dir, "Ground"), shlex.split(r"las2las -i *.las -
odir '{0}' -keep_class 2 -set_classification 0").format(os.path.join(main_dir, "ClassReset")))
    elif r == (len(passes)-1):
        args_list[3] = ("Keep ground points", os.path.join(main_dir, "Ground"), shlex.split(r"las2las -i *.las -odir '{0}' -
keep_class 2").format(os.path.join(main_dir, "ClassReset")))

    # Run passes
    for arg in args_list:
        print arg[0]
        os.chdir(arg[1])
        proc = subprocess.check_output(arg[2])
        if proc != "":
            # If the process fails, need to remove existing folder directory
            print "EXCEPTION", proc
            raise Exception(proc)

    # Lock should be gone on old folder, try to remove
    old_main_dir = "{0}\Pass{1}_{2}mTile".format(output_dir, r, (tile_size*2))
    if os.path.exists(old_main_dir):
        try:
            shutil.rmtree(old_main_dir)
            print "Successfully removed old processing folder {0}.".format(old_main_dir)

```

```

    except:
        print "Still can't removed old directory {0}.".format(old_main_dir)

def processing_tree(raw_pt_cld, passes, output_dir, overwrite_output, subfolders):
    # Index the raw point cloud
    os.chdir(raw_pt_cld)
    print "Indexing raw point cloud"
    args = r"lasindex -i *.las"
    results = subprocess.check_output(args)
    if results != "":
        raise Exception("Unable to index raw point cloud. Check file path.")
    # Work through passes after creating folder structure for each pass
    for r in range(0, 3, 1):
        print "Pass", r+1
        # Determine parameters from input Passes dictionary
        tile_size = passes[r][0]
        spike = passes[r][1]
        bulge = passes[r][2]
        step = passes[r][3]
        # Create raw point cloud directory
        if r > 0:
            raw_pt_cld = os.path.join(output_dir, "Pass{}".format(r + 1), "NewCloud")
            main_dir = "{0}\Pass{1}_{2}mTile".format(output_dir, r, tile_size)
            if os.path.exists(main_dir):
                if not overwrite_output:
                    raise Exception("Directory already exists: {}".format(main_dir))
                else:
                    shutil.rmtree(main_dir)
                    os.makedirs(main_dir)

            # Create folder structure
            for f in subfolders:
                new_folder = "{0}\{1}".format(main_dir, f)
                os.makedirs(new_folder)

            # Process point cloud
            point_cloud_processing(r, main_dir, raw_pt_cld, tile_size, spike, bulge, step)

def retry(passes, raw_pt_cld, output_dir, overwrite_output, subfolders):
    print "Reducing tile size to conserve memory"
    for place, p in enumerate(passes):
        tile_size = p[0]
        passes[place][0] = tile_size / 2
    for place, p in enumerate(passes):
        print "New tile size: {0}".format(passes[place][0])

    return passes

def confirm_choice():
    result = tkMessageBox.askyesno("Confirm Overwrite", "Overwrite existing data in this directory?", icon = "warning")
    print result
    return result

# Variables -----
# Get data from user
Tk().withdraw()
raw_pt_cld = tkFileDialog.askdirectory(title = "Raw Point Cloud Location")
output_dir = tkFileDialog.askdirectory(title = "Output Directory")

```

```

overwrite_output = confirm_choice()

# Pre-defined variables
subfolders = [
    "Tiles",
    "SortedTiles",
    "Ground",
    "ClassReset",
    "RemoveBuffers",
    "NewCloud"
]

timestamp = time.time()
datestamp = datetime.datetime.fromtimestamp(timestamp).strftime('%m-%d-%Y %H:%M:%S')
log_file = open(os.path.join(output_dir, "error_log.txt"), "w")
log_file.write("Error Log for Point Cloud Segmentation Script {0}\n".format(datestamp))

# Process -----

# Create folders for each pass over point cloud
pass_folders = [
    os.path.join(output_dir, "Pass1"),
    os.path.join(output_dir, "Pass2"),
    os.path.join(output_dir, "Pass3"),
]

# Pass variables
# Pass : [TileSize, Spike, Bulge, Step]
passes = [
    [250, 0.05, "-no_bulge", 1],
    [500, 0.1, "-no_bulge", 5],
    [1000, 0.2, "-bulge 1", 50]
]

# Process -----
result = None
while result is None:
    try:
        processing_tree(raw_pt_cld, passes, output_dir, overwrite_output, subfolders)
        result = 1
    except:
        passes = retry(passes, raw_pt_cld, output_dir, overwrite_output, subfolders)
        continue

# Delete intermediate data
print "Removing intermediate data from Pass"
# os.chdir(output_dir)
try:
    for p in pass_folders[:2]:
        if os.path.exists(p):
            shutil.rmtree(p)
    shutil.move(os.path.join(output_dir, "Pass3\\NewCloud"), output_dir)
    shutil.rmtree(pass_folders[2])
except:
    pass

log_file.close()

```